
Electronic Thesis and Dissertation Repository

4-21-2017 12:00 AM

Methods for Improved Estimation of Low Blood Velocities Using Vector Doppler Ultrasound

Bushra Hussain
The University of Western Ontario

Supervisor
Prof. Tamie L Poepping
The University of Western Ontario Joint Supervisor
Prof. James C Lacefield
The University of Western Ontario

Graduate Program in Physics
A thesis submitted in partial fulfillment of the requirements for the degree in Doctor of Philosophy
© Bushra Hussain 2017

Follow this and additional works at: <https://ir.lib.uwo.ca/etd>



Part of the [Other Physics Commons](#)

Recommended Citation

Hussain, Bushra, "Methods for Improved Estimation of Low Blood Velocities Using Vector Doppler Ultrasound" (2017). *Electronic Thesis and Dissertation Repository*. 4515.
<https://ir.lib.uwo.ca/etd/4515>

This Dissertation/Thesis is brought to you for free and open access by Scholarship@Western. It has been accepted for inclusion in Electronic Thesis and Dissertation Repository by an authorized administrator of Scholarship@Western. For more information, please contact wlsadmin@uwo.ca.

Abstract

Accurate estimation of low 3D blood velocities, such as near the wall in recirculation or disturbed flow regions, is important for accurate mapping of velocities to improve estimations of wall shear stress and turbulence, which are associated risk factors for vascular disease and stroke. Doppler ultrasound non-invasively measures blood-velocities but suffers from two major limitations addressed in this thesis. These are angle dependence of the measurements, which requires the knowledge of beam-to-flow angle, and the wall-filter. The high-pass wall filter that is applied to attenuate the high-intensity low-frequency signal from tissue and slowly moving vessel wall also attenuates any low velocity signals from blood thus causing inaccurate estimation of these velocities. This thesis presents two methods to alleviate the angle-dependence limitation and to minimize the effect of the wall filter on low blood-velocity estimates: a multi-receiver technique – vector Doppler ultrasound (VDUS), and a novel method called aperture-translation technique.

For the first method – VDUS, theoretical and experimental studies were performed to assess the comparative benefit of three to eight receivers (3R–8R) in Doppler ultrasound configurations in terms of the number of receiver beams, inter-beam angle, and beam-selection method (criterion for discriminating between tissue and blood Doppler signals) for a range of velocity orientations. Accuracy and precision for ≥ 5 receivers were consistently better over all flow velocity orientations and for all beam-selection methods. Asymmetry in the 5R configuration led to improved accuracy and precision compared to symmetrical 6R and 8R configurations.

Second, a novel 2D-VDUS aperture-translation technique using mechanical or electronic translation of the transmit-receive apertures was introduced and assessed experimentally. Both versions of the technique outperformed the conventional 2D-VDUS method for detection of low flow velocities in terms of accuracy and precision. The electronic version, which is more relevant and feasible clinically, showed comparable reliability and better accuracy compared with the idealized mechanical version, therefore suggesting its potential for future development. This work demonstrated that a minimum of five receivers, preferably with an inherent asymmetry with respect to the flow direction, should be considered when designing a 2D-array configuration for improved estimation of low velocities. For estimation of low velocities not measurable with conventional VDUS methods, the aperture-translation technique could be a potential candidate.

Keywords

Crossbeam, multi-receiver configuration, vector Doppler ultrasound, blood velocities, wall filter cut-off, aperture-translation.

Co-Authorship Statement

Chapter 2: Methods and Materials

This chapter describes the apparatus and experimental setups, as well as the methods for data acquisition and data processing for the studies presented in this thesis. Data acquisition and data processing for the first study is part of the published work “Investigation of Crossbeam Multi-Receiver Configurations for Accurate 3D Vector Velocity Estimation”, in *IEEE Transactions on Ultrasonics Ferroelectrics and Frequency Control*, vol. 63, pp. 1786-1798, Nov 2016. The article is co-authored by B. Hussain, B. Y. S. Yiu, A. C. H. Yu, J. C. Lacefield, and T. L. Poepping. I designed and fabricated the large straight-tube and the carotid flow phantoms; B. Dalrymple and F. Van Sas machined the containers. S. I. Hussain and I designed and built the gravity-flow setup.

Chapter 3: Crossbeam Multi-Receiver Configurations

The major portion of this chapter is part of an article entitled “Investigation of Crossbeam Multi-Receiver Configurations for Accurate 3D Vector Velocity Estimation”, which has been published in *IEEE Transactions on Ultrasonics Ferroelectrics and Frequency Control*, vol. 63, pp. 1786-1798, Nov 2016. The article is co-authored by B. Hussain, B. Y. S. Yiu, A. C. H. Yu, J. C. Lacefield, and T. L. Poepping. I wrote the velocity re-construction code for both the theoretical and experimental studies, designed and performed the experiments, analyzed the results and wrote the manuscript. B. Y. S. Yiu wrote the data acquisition and the signal-processing code. A. C. H. Yu, J. C. Lacefield, and T. L. Poepping reviewed the results and manuscript prior to submission.

Chapter 4: Vector Doppler Ultrasound Aperture-Translation

This chapter presents the results and discussion of a novel VDUS technique called ‘aperture translation’. The work will form the basis for submission to *IEEE Transactions on Ultrasonics Ferroelectrics and Frequency Control* with co-authors B. Hussain, B. Y. S. Yiu, A. C. H. Yu, J. C. Lacefield, and T. L. Poepping. I perceived the idea, modified the acquisition and signal processing code (initially written by B. Y. S. Yiu) for the new technique, wrote the velocity re-construction codes, designed and performed the experiments, analyzed and wrote the results (Chapter 4). J. C. Lacefield, and T. L. Poepping advised and reviewed the results.

Dedication

To my brother Syed Intesar Hussain

Acknowledgments

During the course of my PhD research I have come to know several wonderful people who have helped and supported me through this journey, to whom I am very thankful.

I am very grateful to my supervisors, Dr. Tamie Poepping and Dr. James Lacefield for providing this opportunity. Thank you Tamie for your endless support, encouragement, professional guidance, advice and believing in my abilities. Thank you Jim for your wisdom in many aspects of the research, provoking in me the deeper understanding of things, and for useful advice as I worked through various challenges of the research.

I thank my collaborators, Dr. Alfred Yu and Billy Yiu, for their generous help in programming and troubleshooting of the SonixRP scanner, and answering all my queries with patience. Thank you Alfred for your encouragement, useful advice and feedback in preparing the manuscript.

A big thank you to Dr. Will Handler, who coached and mentored me in the initial period of my PhD, showed me how to troubleshoot computer problems and taught me Matlab from scratch. My advisors Dr. Andrea Soddu and Dr. Silvia Mittler for the much appreciated ongoing advice and support. Thanks to the Physics and Astronomy administrative staff, Jodi Guthrie, Anne Brooks, Clara Buma, Jackie McLean, and Brian Davies, for helping in all matters, academic and financial.

I extend my thanks to all the department's technical staff for without their help I would not have been able to run the experiments presented in my thesis. Especially, Phin Perquin – for going above and beyond in providing technical support, assisting in writing, experimental runs, providing constant encouragement and beyond; thanks for being a great friend. Henry Leparskas – for helping me get beyond the blue-screen-of-death several times. Doug Hie – for sharing his insight in technical matters and meticulous troubleshooting of electronics. Machinists, Brian Darymple and Frank Van Sas – for their ability to understand and decipher my cryptic drawings, turning them into the much needed flow phantoms and related equipment for my experiments. Tim Goldhawk - for copious supply of distilled water for the

making of BMF. Dr. Gord Campbell, John Moore, and Hristo Nikolov, for their insight and technical help in the design and fabricating of flow phantoms.

Present and past lab group members for their support and help, especially Dr. Emily Wong, for her generosity and willingness to help in any way, and Dr. David Tessier, for his boundless help, both of whom I became great friends with.

I would like to thank my late parents, (Anwar and Zakia) for their love and instilling in me the derive to learn more. My family for all their love and moral support, especially my brother, Intesar, for inspired discussions on the research topics, his tremendous support at many levels, encouragement and understanding while walking through all the highs and the lows; thank you for being an awesome brother!

Financial support is gratefully acknowledged from the *Canada Foundation of Innovation* (CFI), *Canadian Institutes of Health Research* (CIHR), the *Heart and Stroke Foundation of Canada*, and the *University of Western Ontario*.

Finally, I thank the many other people who became my friends and were there for me.

Table of Contents

Abstract.....	ii
Co-Authorship Statement.....	iv
Chapter 2: Methods and Materials.....	iv
Chapter 3: Crossbeam Multi-Receiver Configurations.....	iv
Chapter 4: Vector Doppler Ultrasound Aperture-Translation	v
Dedication.....	vi
Acknowledgments.....	vii
Table of Contents.....	ix
List of Tables	xiv
List of Figures.....	xv
List of Appendices	xxi
List of Abbreviations and Symbols.....	xxii
Chapter 1.....	1
1 Introduction and Background.....	1
1.1 Overview.....	1
1.2 Clinical Motivation – Stroke.....	4
1.3 Significance of Hemodynamics for Vascular Disease Diagnosis.....	8
1.4 Modalities for <i>In-vivo</i> Blood Flow Characterization	11
1.5 Background of Ultrasound.....	12
1.5.1 Ultrasound.....	12
1.5.2 Doppler Ultrasound.....	13
1.5.2.1 Pulsed-Wave Doppler Ultrasound.....	14
1.5.2.2 Basic Signal Processing of Doppler Ultrasound.....	15
1.5.2.3 Mean Velocity Estimation Using Spectral Analysis	19

1.5.2.4	<i>Mean Velocity Estimation Using Autocorrelation</i>	20
1.5.3	Clutter Filter and its Effect on the Doppler Signal	23
1.6	Background and Overview of Vector Doppler Ultrasound Techniques	27
1.6.1	Key 2D/3D Vector Velocity Techniques.....	27
1.6.1.1	<i>Spectral Broadening and Dual-Beam Tracking</i>	27
1.6.1.2	<i>Speckle Tracking (Non-Doppler Technique)</i>	28
1.6.1.3	<i>Transverse Oscillation</i>	29
1.6.1.4	<i>Vector Velocity Techniques with PWI</i>	29
1.6.2	Crossbeam VDUS Technique	30
1.6.2.1	<i>3D-VDUS Crossbeam Systems</i>	34
1.7	Research Objectives and Thesis Outline.....	35
1.7.1	Chapter 2: Methods and Materials.....	37
1.7.2	Chapter 3: Crossbeam Multi-Receiver Configurations.....	37
1.7.3	Chapter 4: Vector Doppler Ultrasound Aperture-Translation	38
1.7.4	Chapter 5: Summary, Conclusion, and Future Directions	38
Chapter 2	39
2	Materials and Methods.....	39
2.1	Theory and Principles	39
2.1.1	Velocity Vector Reconstruction from Doppler Shifts	39
2.1.1.1	<i>Velocity Reconstruction Algorithm for Two Receivers</i>	41
2.1.2	Basic Equations.....	43
2.1.2.1	<i>Poiseuille's Law</i>	43
2.1.2.2	<i>Velocity Bias and Relative Error</i>	43
2.1.2.3	<i>Standard Deviation and Standard Error</i>	44
2.1.3	Vector Doppler Ultrasound Aperture-Translation Principle.....	44

2.2 Apparatus and Experimental Setup.....	47
2.2.1 SonixRP System	47
2.2.2 SonixDAQ	48
2.2.3 TEXO Software Development Kit.....	49
2.2.4 Linear Array Transducer.....	49
2.2.5 Translational Motion Control Stages	49
2.3 Flow Phantoms Fabrication	50
2.3.1 Wall-less Straight-tube Flow Phantom	51
2.3.2 Wall-less Carotid Flow Phantom	52
2.3.3 Gravity-Flow Setup.....	55
2.4 Data Acquisition and Processing	57
2.4.1 Crossbeam Multi-Receiver Configurations	57
<i>2.4.1.1 Beam-Selection Methods</i>	<i>60</i>
2.4.2 Vector Doppler Ultrasound Aperture-Translation	61
<i>2.4.2.1 Mechanical Sweep</i>	<i>61</i>
<i>2.4.2.2 Electronic Sweep</i>	<i>63</i>
Chapter 3.....	66
3 Crossbeam Multi-Receiver Configurations	66
3.1 Effective Wall Filter	66
3.2 Theoretical Geometric Analysis	69
3.3 Experimental Results	72
3.3.1 Doppler Power and Velocity Components	72
3.3.2 Relative Performance of Multi-Receiver Configurations for Velocity Estimations.....	76
<i>3.3.2.1 Velocity Estimations Improve with Increasing Inter-beam Angle....</i>	<i>78</i>

3.3.2.2	<i>Beam-Selection Methods Perform Equally Well for $\geq 5R$ at Low Velocities</i>	78
3.3.2.3	<i>Velocity Orientation Sensitivity Reduced for $\geq 5R$</i>	79
3.3.2.4	<i>Beam-Selection Methods Perform Equally Well for $\geq 4R$ at Higher Velocities</i>	81
3.4	Discussion	83
Chapter 4		91
4	Vector Doppler Ultrasound Aperture-Translation	91
4.1	Mechanical-Sweep Method	92
4.2	Electronic-Sweep Method	102
4.3	Electronic-Sweep Versus Mechanical-Sweep	105
4.4	Discussion	108
4.4.1	Practical Limitations of VDUS Aperture Translation	114
Chapter 5		116
5	Summary, Conclusion, and Future Directions	116
5.1	Summary and Conclusion	116
5.1.1	Crossbeam Multi-Receiver Configurations	116
5.1.2	Vector Doppler Ultrasound Aperture-Translation	117
5.2	Future Directions	118
5.2.1	2D Array Design of a 5R configuration	118
5.2.2	Optimized Beam-Selection Method	119
5.2.3	Implementation of Optimized 2D array for <i>In-vitro</i> and <i>In-vivo</i> Assessment	120
5.2.4	Optimization of VDUS Aperture-Translation Technique	122
5.2.5	Reducing Effect of Wall Motion on VDUS Aperture-Translation	123
Bibliography		125
Appendices		139

Appendix A-1	Justification of Effective Wall Filter Value.....	139
Appendix A-2	Resultant Velocity Magnitude and Direction	140
Appendix A-3	Geometric Analysis at WF_{eff} of 50 Hz for 10 cm/s	142
Appendix A-4	Performance of 5R Configuration at $\beta = 15^\circ$	143
Curriculum Vitae	145

List of Tables

Table 2.1: Ultrasound Imaging Parameters	59
--	----

List of Figures

Figure 1.1: Carotid artery bifurcation showing the common, internal, and external carotid artery. The internal carotid is shown with plaque built-up and an embolus blocking the blood flow. Source: National Heart Lung and Blood Institute (NIH) (National Heart Lung and Blood Institute (NIH)) [Public domain], via Wikimedia Commons..... 6

Figure 1.2: Example of a velocity map in an asymmetric 50% stenosed carotid bifurcation model generated using computational fluid dynamics. Black arrows represent velocity vectors overlaid on color-encoded map showing a range of velocities in forward and reverse direction. The presence of high-velocity jet, large recirculation regions, and downstream turbulent flow, such as vortices are shown (as labeled). (Courtesy of E. Y. Wong, Western University). 9

Figure 1.3: Schematic showing the basic working principle of Doppler ultrasound. Velocity component V_c along the beam direction is estimated from blood scatterer velocity, V , at a Doppler angle, θ_d 14

Figure 1.4: Block diagram of basic signal processing used in pulsed wave Doppler ultrasound for velocity estimations..... 16

Figure 1.5: Schematic showing the sample-and-hold operation using (a) ‘n’ number of backscattered RF signal from a scatterer moving away from the transducer. First signal received when the scatterer enters the sample volume and moves away for each transmission. (b) Doppler signal (slow time signal) constructed from sampling ‘n’ RF pulses at a specified time indicated by the vertical dashed line in (a). 17

Figure 1.6: Duplex ultrasound display of a carotid bifurcation flow phantom showing a B-mode image (upper half) and Doppler spectrogram (lower half). The direction of the flow is from right to left..... 19

Figure 1.7: Triplex ultrasound display of a carotid bifurcation flow phantom including B-mode, Doppler-mode, and color Doppler-mode combined. The direction of the flow is from right to left..... 22

Figure 1.8: Illustration of hypothetical Doppler spectra from the high-intensity, low-frequency signal from the stationary and slowly moving walls (red) with the very low-intensity blood signal (blue). A hypothetical frequency response of a wall filter is shown in black to demonstrate its effect on the low frequency blood signal when the two signals overlap in frequency. 24

Figure 1.9: Schematic of a general crossbeam vector Doppler ultrasound system for estimation of 2D velocities with two transceivers separated by an angle δ 31

Figure 2.1: (a) Schematic of a linear array showing the central-transmit aperture and two sliding receiver apertures (labeled R_c) to maintain constant inter-beam angle (β) with changing depth. The 3D velocity vector with magnitude V and direction specified by θ

(elevation angle) and $\Delta\phi$ (azimuthal rotation angle) is shown. (b) Top view of the linear array showing azimuthal rotations of $\phi_n = 60^\circ$ and 120° (in gray) to simulate a 3R and 6R, (c) 4R and 8R, and (d) 5R configurations. The dotted and dashed lines in (b, c, & d) show geometric shapes and receiver orientations used for each configuration. 40

Figure 2.2: Schematic showing a transmit-aperture with left and right receive-apertures swept along the length of the linear array, i.e. $-y$ direction. The transmit-sweep velocity, V_s , is opposite to the flow velocity vector, V . V_s is the velocity of the transmit-receive apertures for E-sweep or the velocity of the transducer for the M-sweep method. The step size of the motion is equal to the element-pitch of the transducer, Δy in the E-sweep, whereas for M-sweep it is the distance travelled by the transducer during one pulse repetition period. 45

Figure 2.3: Schematic for working principle for both the M-sweep and E-sweep methods. (a) An exaggerated step Δy is shown for two consecutive transmit pulses from depth, d , received with an interbeam angle, β . (b) Schematic showing signal received from the same sample volume but received at a distance Δy away from the first receiver location. The path difference due to the receiver displacement is Δd 46

Figure 2.4: Transducer holder attached to the vertical translational stage of the three-axis system. The linear motion along x , y , and z axes (dashed yellow arrows) and rotational motion about the z and x axis of the holder are shown (yellow circled arrows). The yellow arrows represent the direction of motion of the linear stages. 50

Figure 2.5: Agar-based wall-less straight-vessel phantom with 2.46 cm internal diameter. ... 51

Figure 2.6: Key fabrication steps (a-c) of a CCA flow phantom (d). 54

Figure 2.7: Duplex display of the B-mode image and the Doppler spectral mode showing the CCA vessel and the velocity spectrogram from a sample volume placed at the center of the vessel, as indicated by the cursor in the B-mode image. 55

Figure 2.8: Schematic (top) and photo (bottom) of the gravity-fed flow setup. Blood-mimicking fluid in a raised reservoir (1) flows through the phantom (2) at a gravity-driven rate determined by the height of the reservoir and then into the collector tank (3). Fluid is returned to the reservoir via the intermediate feedback tank (4). 56

Figure 2.9: Schematic representing the principle of the E-sweep method. One scan-line is obtained from an ensemble of N taken along the transmit sweep direction with a sliding step of two elements. The red dots represent one subset of data chosen for velocity estimations. The slow time ($1/PRF_{flow}$) sampling is equal to the maximum PRF (PRF_{max}) divided by the total number of pulses (n) sent from one transmit center. The purple line shows the number of pulses skipped (slow time period) to process only the pulses shown in red. 65

Figure 3.1: Frequency response of the equiripple minimum-phase FIR filter of order 21 and 60-dB suppression. The effective wall filter cut-off is indicated by the vertical dashed line corresponding to a normalized frequency of 0.05. 67

Figure 3.2: Experimental mean Doppler shifts (solid) averaged over 160 independent measurements of a velocity of 2 cm/s with a 3R configuration with an inter-beam angle of 20° . The corresponding theoretical Doppler shifts are shown with gray markers. The gray band represents the effective wall-filter cut-off range ($\pm WF_{\text{eff}}$). Error bars represent standard deviations over 160 independent measurements..... 68

Figure 3.3: Color-encoded plots demonstrating theoretical determination of the number of receivers with Doppler shifts exceeding a WF_{eff} of 10 Hz for each of the 3R to 8R configurations (as labeled) for inter-beam angles varying from $\beta = 5^\circ$ to 30° . Each is shown for a 2 cm/s velocity vector rotated through elevation angles $\Delta\theta$ between 75° to 105° relative to the x axis and for the worst-case of azimuthal angles, $\Delta\phi$. The data points labeled with an asterisk correspond to parameters applied in the experiments and the worst-case $\Delta\phi$ (one column per configuration) included in Fig. 3.4. The black dashed-line represents the minimum inter-beam angle for which ≥ 3 receivers' Doppler shifts are above the WF_{eff} for all velocity orientations..... 69

Figure 3.4: Color-encoded plots demonstrating theoretical determination of the number of receivers with Doppler shifts exceeding the effective wall filter cutoff of 10 Hz for 3R - 8R configurations (as labeled) each shown for $\beta = 10^\circ, 15^\circ, 20^\circ,$ and 25° for a 2 cm/s velocity vector rotated through azimuthal angles of $\Delta\phi = 0^\circ, 15^\circ, 30^\circ, 45^\circ,$ and 60° relative to y axis with an elevation angle $\theta = 90^\circ$ 71

Figure 3.5: Mean Doppler power from each receiver beam oriented at various azimuthal rotation angles (legend labels), averaged over 160 independent measurements, to achieve 3R to 8R configurations, with $\beta = 20^\circ$, for velocity vectors oriented at an azimuthal angle of 90° (i.e. azimuthal rotation, $\Delta\phi = 0^\circ$ relative to y axis) and elevation angle $\theta = 90^\circ$, for a parabolic flow data. The beam-selection method used is the PT method, indicating the Doppler power chosen as shown by the black dashed lines in each sub-plot. The legend labels represent the azimuthal rotations of the receiver beams with respect to the velocity vector. The error bars represent SDs. Vertical dashed-lines separate the lumen and TMM regions.. 73

Figure 3.6: Mean Doppler velocities from each receiver beam oriented at various azimuthal rotation angles each with an elevation angle of 20° , averaged over 160 independent measurements, to achieve 3R to 8R configurations, with $\beta = 20^\circ$, for velocity vectors oriented at an azimuthal angle of 90° (i.e. azimuthal rotation, $\Delta\phi = 0^\circ$ relative to y axis) and elevation angle $\theta = 90^\circ$, for parabolic flow. The legend labels represent the azimuthal rotations of the receiver beams relative to the velocity vector (i.e. vessel axis). For example, a 3R configuration would be reconstructed from beams at $0^\circ, 120^\circ,$ and 240° ; this could be extended to 6R by including beams at $60^\circ, 180^\circ,$ and 300° . The error bars represent SD. Vertical dashed lines separate the lumen and TMM regions..... 74

Figure 3.7: Sample parabolic flow data representing mean Doppler velocity vector estimations for (a) magnitude, (b) azimuthal direction, and (c) elevation direction, averaged over 160 independent measurements for each of 3R to 8R configurations, with $\beta = 20^\circ$, for velocity vectors oriented at an azimuthal angle of 90° (i.e. azimuthal rotation, $\Delta\phi = 0^\circ$ relative to y axis) and elevation angle $\theta = 90^\circ$, after applying the PT method. Theoretical

velocity magnitude profile and direction are shown in solid black line. Note that velocity estimations from only the upper half of the profile were used for the analysis. 75

Figure 3.8: Bias in velocity magnitude (a – c) and direction bias (d – f) averaged over all orientations comparing beam-selection methods for 3R - 8R configurations and $\beta = 15^\circ$ (a, d), 20° (b, e) and 25° (c, f) when measured a theoretical velocity vector of 2 cm/s. Biases represent the averaged differences between the experimental and theoretical values over all five azimuthal orientations ($\Delta\phi = 0^\circ, 15^\circ, 30^\circ, 45^\circ, 60^\circ$ relative to y axis). Error bars represent SDs over 800 measurements. 77

Figure 3.9: Velocity magnitude bias (a – c) and direction bias (d – f) comparing beam-selection methods for 4R to 6R configurations (as labeled) versus azimuthal rotation for $\beta = 20^\circ$ when measured a theoretical velocity of 2 cm/s. Biases are averaged differences with respect to the theoretical value over 160 independent measurements for each orientation. Error bars represent the standard deviations (SD) over 160 measurements. Note the error bars in (d) extend beyond the plotted region ($40^\circ \leq SD \leq 51^\circ$). 80

Figure 3.10: Relative error of the means in velocity magnitude (a-c) and direction bias (d-f) comparing beam-selection methods for a theoretical velocity range of 1 to 5 cm/s for 4R to 6R configurations (as labeled) at $\beta = 20^\circ$. Biases are averaged differences over all velocity vector orientations ($\Delta\phi = 0^\circ, 15^\circ, 30^\circ, 45^\circ, 60^\circ$ relative to y axis). Error bars represent the standard deviations over 800 measurements. 82

Figure 3.11: Color-encoded plots demonstrating theoretical determination of the number of receivers with Doppler shifts exceeding an WF_{eff} of 50 Hz for 3R to 8R configurations (as labeled) with varying inter-beam angle from $\beta = 5^\circ$ to 65° . Each is shown for a 5 cm/s velocity vector rotated through elevation angles $\Delta\theta$ from 65° to 115° relative to the x-axis and for the worst-case of azimuthal angles, $\Delta\phi$. The data points labeled with an asterisk (i.e. one column per configuration) correspond to parameters applied in the experiments and the worst-case $\Delta\phi$. The black dashed-line represents the minimum inter-beam angle for which Doppler shifts from ≥ 3 receivers exceed the WF_{eff} for all velocity orientations. 87

Figure 3.12: An example of possible 2D probe design for a 5R configuration using a 64×64 element grid with each element pitch of 0.3 mm along both directions. Note that the outline of these circular apertures will be pixelated either including or excluding the elements that lie on the aperture boundary. 90

Figure 4.1: Mean Doppler frequency profile for varying mechanical-sweep speeds (0 – 50 mm/s) for ensemble sizes (as labeled) (a – d), in the stationary TMM and for parabolic flow in the CCA-vessel of the carotid flow phantom with a peak velocity of 3.4 cm/s. The positive and negative Doppler shifts are from the left and right receiver beams, respectively, at an inter-beam angle of 20° and a PRF of 223 Hz. Doppler shifted frequencies are averaged over 70 independent measurements. The vertical dashed-lines separate the lumen and the TMM regions. 93

Figure 4.2: Mean resultant velocity magnitude profiles reconstructed from the left and right receivers' Doppler shifts for varying sweep speeds (0 – 50 mm/s) for four ensembles (a – d), in the TMM and in the CCA of the carotid flow phantom with a peak velocity of 3.4 cm/s at

$\beta = 20^\circ$ and a PRF of 223 Hz. The velocities are averaged over 70 independent measurements..... 94

Figure 4.3: (a) Example of resultant mean velocity magnitude profiles reconstructed from the left and right receivers' Doppler shifts with no power threshold applied to the data (b) resultant mean velocity profiles after applying power threshold, and (c) mean Doppler powers showing constant power threshold applied (gray horizontal line) to all data, for varying sweep velocities (0 – 50 mm/s) for an ensemble size of 12 at $\beta = 20^\circ$ and a PRF of 223 Hz, in the TMM and in the CCA of the carotid flow phantom with a peak velocity of 3.4 cm/s. Resultant velocity magnitude and Doppler powers are averaged over 70 independent measurements. The vertical dashed-lines separate the lumen and the TMM regions. 95

Figure 4.4: Velocity magnitude bias (a-d) and standard deviations (e-h) for four specified flow velocities (as labeled) measured at $\beta = 20^\circ$, comparing five sweep speeds for ensemble sizes ranging from 4 to 16. Biases are differences averaged over 70 independent measurements..... 97

Figure 4.5: Relative error in velocity magnitude comparing varying sweep speeds for a theoretical velocity range of 0.5 to 3 cm/s for ensembles of 4 to 16 (as labeled) at $\beta = 20^\circ$. Relative errors are calculated from the estimated velocities averaged over 70 measurements. Error bars represent relative standard deviations..... 100

Figure 4.6: Relative error (a,b) and SD (c,d) in velocity magnitude comparing inter-beam angles of 15° and 20° at various sweep speeds for flow velocities ranging from 0.5 to 3 cm/s for an ensemble size of 12. Relative errors are calculated from the estimated velocities averaged over 70 measurements. Error bars (in a, b) represent the relative standard deviations over 70 measurements..... 101

Figure 4.7: Mean resultant velocity magnitude profiles reconstructed from the left and right receivers' Doppler shifts for varying electronic-sweep speeds for an ensemble of 12, in the TMM and in the straight-vessel flow phantom with a peak velocity of 3.4 cm/s at a β of 15° . The flow velocities are averaged over 60 independent measurements..... 102

Figure 4.8: Left and right single-line Doppler frequencies for conventional (a-c), M-sweep (d-f), and E-sweep (g-i) methods using varying PRFs (112, 134, and 168 Hz), which correspond to sweep speeds of 3.5, 4, and 5 cm/s, respectively..... 104

Figure 4.9: Mean resultant velocity magnitude profiles reconstructed from the left and right receivers' Doppler frequencies comparing M-sweep and E-sweep methods with case-0 and theoretical velocity profiles for three matching sweep speeds (3.5, 4, and 5 cm/s) with corresponding PRFs (as labeled) for an ensemble of 12 at $\beta = 15^\circ$. The velocities are averaged over 60 independent measurements..... 106

Figure 4.10: Velocity magnitude (a-c) comparing mechanical and electronic-sweep methods with conventional method for theoretical velocities ranging from 0.5 to 3 cm/s (in gray) for three matching sweep speeds (3.5, 4, and 5 cm/s) with corresponding PRFs (as labeled) for an ensemble of 12 at $\beta = 15^\circ$. Error bars represent the standard error over 60 measurements.

Standard deviations (d-e) for the three methods are compared for the same flow velocities.107

Figure 4.11: Theoretical Doppler frequencies, seen by two symmetrically oriented receiver beams at an interbeam angle of 20° for various sweep velocities (a – f), due to axial wall of 0.8 cm/s with no sweep velocity, wall velocity (perpendicular to the flow velocity) with sweep speed, and lateral flow velocity of 1 cm/s..... 111

Figure A-1.1: Experimental mean Doppler shifts (solid) averaged over 160 independent measurements of a velocity of 2 cm/s with a 3R configuration with inter-beam angles of (a) 15° and (b) 25° . The corresponding theoretical Doppler shifts are shown with gray markers. The gray band represents the effective wall-filter cut-off range ($\pm WF_{\text{eff}}$). Error bars represent standard deviations over 160 independent measurements. 139

Figure A-2.1: Sample parabolic flow data representing mean Doppler velocity vector estimations for (a) magnitude, (b) azimuthal direction, and (c) elevation direction, averaged over 160 independent measurements for each of 3R - 8R configurations, with $\beta = 20^\circ$, for velocity vectors oriented at an azimuthal angles of 105° , 120° , 135° , and 150° (i.e., azimuthal rotations of $\Delta\phi = 15^\circ$, 30° , 45° , and 60° , respectively, relative to y axis) and elevation angle $\theta = 90^\circ$, after applying the PT method. Theoretical velocity magnitude profile and direction are shown in solid black line..... 141

Figure A-3.1: Color-encoded plots similar to Fig. 3.3 shown here for a WF_{eff} of 50 Hz and for a 10 cm/s velocity vector rotated through $\Delta\theta$ from 75° to 105° relative to the x-axis and for the worst-case of, $\Delta\phi$. The black dashed-line represents the minimum inter-beam angle for which ≥ 3 receivers' Doppler shifts are above the WF_{eff} for all velocity orientations.... 142

Figure A-4.1: Relative error of the mean velocity magnitude (a-c) and direction bias (d-f) comparing beam-selection methods for a theoretical velocity range of 1 to 5 cm/s for 4R - 6R configurations (as labeled) at $\beta = 15^\circ$. Biases are averaged differences over all velocity vector orientations ($\Delta\phi = 0^\circ$, 15° , 30° , 45° , 60° relative to y axis). Error bars represent the standard deviations over 800 measurements..... 144

List of Appendices

Appendix A-1 Justification of Effective Wall Filter Value	139
Appendix A-2 Resultant Velocity Magnitude and Direction	140
Appendix A-3 Geometric Analysis at WF_{eff} of 50 Hz for 10 cm/s.....	142
Appendix A-4 Performance of 5R Configuration at $\beta = 15^\circ$	143

List of Abbreviations and Symbols

Alphanumeric

\vec{B}_j	three-dimensional vector along the j^{th} beam direction
c	speed of sound
Δd	path difference
$D_{\text{ICA,min}}$	minimum luminal diameter in the internal carotid artery
$D_{\text{ICA,distal}}$	distal luminal diameter in the internal carotid artery
f_d	Doppler frequency
f_n	Doppler frequency of n^{th} beam
f_r, f_t	receive and transmit frequency
\hat{i}_n, \hat{i}_o	unit vectors along n and transmit direction
n	number of receivers
N	receiver number
\hat{u}_1, \hat{u}_2	orthogonal unit velocity vectors in a plane of vectors \vec{B}_1 and \vec{B}_2
\vec{V}	flow velocity vector
\vec{V}_R	resultant flow velocity vector
\vec{V}_S	aperture sweep velocity vector
V_x, V_y, V_z	flow velocity magnitude along x, y, and z axis respectively
V_{yz}	flow velocity magnitude in the yz plane
x_i	i^{th} experimental measured value
x	theoretical value
Δy	aperture displacement

Greek

β	inter-beam angle
δ	inter-transceiver angle
λ	wavelength
$\Delta\varphi$	phase-difference
$\Delta\phi$	velocity vector angle relative to y-axis in xy-plane
ϕ'_n	azimuthal angle for the n^{th} receive beam
θ	elevation angle
θ_d	Doppler angle

Abbreviations

1D, 2D, 3D, 4D	one-, two-, three-, and four-dimensional, respectively
A-line	amplitude mode scanline
A-mode	amplitude mode
AVF	arteriovenous fistula
BMF	blood-mimicking fluid
B-mode	brightness mode
Case-0	case with stationary aperture
CCA	common carotid artery
CFD	computational fluid dynamics

CFI	color flow imaging
CWD	continuous-wave Doppler
DUS	Doppler ultrasound
E3.5, E4, E5	electronic aperture translation at sweep speed 3.5, 4, 5 cm/s, respectively
ECA	external carotid artery
E-sweep	electronic-sweep
FIR	frequency impulse response
ICA	internal carotid artery
ID	internal diameter
M1, ..., M5	mechanical aperture motion, sweep speeds 1 to 5 cm/s
MDSD	maximum Doppler standard deviation
M-mode	motion mode
MRI	magnetic resonance imaging
M-sweep	mechanical sweep
NR	N-receiver configuration
NT	no threshold
PC-MRI	phase-contrast magnetic resonance imaging
PIV	particle imaging velocimetry
PRF	pulse repetition frequency
PT	power threshold
PVA	polyvinyl alcohol
PWD	pulse-wave Doppler
PWI	plane wave imaging
Rc	receiver
ROI	region of interest
SD	standard deviation
SNR	signal-to-noise ratio
TMM	tissue-mimicking material
T_x	transmit
US	ultrasound
VDUS	vector Doppler ultrasound
WF_{eff}	effective wall filter cut-off
WLS	weighted least squares

Chapter 1

1 Introduction and Background

1.1 Overview

The overall focus of this work is towards improved diagnosis and management of vascular disease in large arteries, such as in the aorta, femoral, renal, and carotid arteries. Vascular disease such as atherosclerosis (thickening or hardening of an arterial wall), plaque ulceration (irregular plaque surface), and aneurysm (localized enlargement of an artery) in these arteries, if left untreated, can form emboli and can eventually lead to heart attack or stroke. It is understood that initiation and progression of the disease can manifest into changes in the blood flow. Therefore, better understanding and accurate measurement of blood flow and related parameters may be useful in early diagnosis and management of the disease and prevention of cerebrovascular events.

Accuracy in blood velocity estimation in the carotid arteries is important for improved diagnostic assessment of stroke risk, both in terms of accurately determining the jet velocity and estimating the related shear stress and turbulence. The jet velocity is a surrogate measure of stenosis severity (narrowing) and a known correlate of stroke risk (ECST 1991; NASCET 1991). The shear stress and turbulence have been known to play an important role in plaque development, plaque rupture, and thrombus formation (Stein and Sabbah 1974; Reininger et al. 1995; Holme et al. 1997; Tambasco and Steinman 2003; Nesbitt et al. 2009). Flow in arteries is not always laminar (moving in constant-velocity layers) especially after passing through bifurcations, curvatures, or bends, which introduce disturbances and out-of-plane flow, especially if the artery is diseased.

Doppler ultrasound (DUS) is commonly used as a diagnostic tool for non-invasive blood flow imaging and velocity estimations. However, the DUS technique has inherent limitations, such as aliasing, frequency-dependent attenuation, angle-dependent velocity estimations, and the effect on these estimates from a high-pass filter, where the last two are major limitations addressed in this thesis. Aliasing limits the maximum measurable velocity, which is affected by how fast the data is sampled. The frequency dependent attenuation can distort the transmitted/received pulse because higher frequencies attenuate more than the lower frequencies. Due to the angle dependence of DUS, i.e. measuring only a component of the velocity vector along the beam direction, the standard clinical implementation requires *a priori* knowledge of the Doppler angle and generally assumes flow is parallel to the vessel wall. Vessel tortuosity, as well as flow complexity exacerbated by the diseased arterial flow, introduces large variances in the velocity magnitude and direction estimation, both due to incorrect flow assumptions and operator variability in terms of sample-volume placement (Lui et al. 2005; Mynard and Steinman 2013). Vector Doppler ultrasound (VDUS), a multi-receiver technique, obtains Doppler shifted signal from multiple directions from moving scatterers (i.e. blood cells). These signals are then added using vector addition to estimate the resultant velocity of these scatterers. VDUS alleviates the angle dependence of the blood-velocity estimations and therefore can improve the accuracy in estimation of velocities in 2D and 3D, as introduced by Fahrbach (1973) and Fox (1978), respectively.

The other well-known limitation, common to both conventional DUS and VDUS, relates to the effect of the high-pass filter on the low velocity estimates. The filter is applied to the received signal in order to attenuate the high-intensity, low-frequency

signal of stationary or slowly moving tissue. The filter is applied to the received signal in order to attenuate the high-intensity, low-frequency signal of the stationary or slowly moving tissue. Any low or near-transverse blood-velocity signal, if present, is also attenuated, thus leading to incorrect velocities. This high-pass filter is commonly called ‘wall’ or ‘clutter’ filter; the term may be used interchangeably throughout the thesis. Recent work to overcome this limitation has been done using 2D speckle tracking with plane-wave imaging (Fadnes et al. 2015); the technique is only good for 2D vector velocities, and the 3D speckle tracking is computationally demanding. Another approach presented in a recent work (Karabiyik et al. 2016), investigated the effect of adaptive power spectral estimators to determine the accuracy of low blood velocity estimations in color flow imaging without using clutter filtering. Given the assumption required to define an adaptive algorithm, it is unclear that this technique would be effective in applications with disturbed flow. Also, the technique is computationally very demanding compared to the autocorrelation algorithm, which requires only a few computational steps. The focus of this thesis is on improving the effect of the more commonly used filtering method, which uses a fixed value finite impulse response (FIR) filter.

The two studies presented in this thesis attempt to overcome or minimize the effect of the wall-filter to improve the estimation of 3D blood velocities that lie near or within the effective wall filter cut-off (WF_{eff}). The WF_{eff} , which is determined from the data and the parameters of the wall filter, is defined as the frequency at which the Doppler signal attenuation is high enough to cause highly inaccurate and unreliable velocity estimations. The first study is an investigation of the benefit of increasing the number of receivers above three, for improved low 3D velocity estimations, with a

suitable beam-selection criterion. The second study introduces a novel method for improving the signal-to-noise-ratio (SNR) of low SNR Doppler signals. It uses two receivers for proof of concept, but the technique could be extended to 3D velocity vector estimations, as discussed in Chapter 4. Both studies use a crossbeam VDUS technique in which multiple receive-beams cross at the region of interest (ROI) to obtain information from the same ROI. The technique is discussed later in this chapter (section 1.4.2).

Accurate estimation of these low blood velocities would improve wall shear stress estimations and provide accurate mapping and visualization of abnormal hemodynamics. Wall shear stress is measured from the spatial gradient of velocities near the wall, and velocities near the wall are expected to be low. The overall improved quantification of hemodynamics and understanding of how it might affect the initiation and progression of the vascular disease may therefore help in better assessment and diagnosis of the disease. A primary example of this is the carotid artery bifurcation, which is a common site for atherosclerosis causing potential risk of stroke.

1.2 Clinical Motivation – Stroke

Globally, stroke is the second leading cause of death and the third leading cause of lifetime disability (Feigin et al. 2014). In the USA each year, approximately 0.8 million people experience a new or recurrent stroke, out of which 0.6 million are first attacks (Mozaffarian et al. 2015). According to the Canadian Heart and Stroke Association statistics (2012), 6% of all deaths are due to stroke, out of which approximately 80% are ischemic. The major cause of ischemic stroke is the blockage of arteries in the brain by thrombo- or athero-emboli (blood clots or bits of plaque), stopping the blood supply to that part of the brain (Fig. 1.1). These are often formed due to atherosclerosis – a disease

causing narrowing of the vessel due to plaque build-up. Although, most of the strokes can be prevented by lifestyle changes (Warlow et al. 2003), and surgical or drug therapy (Gorelick 1994), early diagnosis and monitoring of the carotid disease can greatly reduce the onset of a new or recurring stroke (Chen et al. 2000; Warlow et al. 2003; Mendis et al. 2005; Strong et al. 2007; Swanepoel and Pretorius 2015).

The initiation (atherogenesis), development, and progression of atherosclerosis are highly focal, occurring in regions of arterial curvatures (aortic arch), branching (femoral, renal artery), and bifurcations (carotid artery). These geometric features have been known to cause hemodynamic changes, such as flow separation (regions where the fluid separates from the surface of a body), generation of vortices and recirculation regions, which induce localized wall shear and tensile stresses, and therefore are linked to atherogenesis (Glagov et al. 1988). One of the most common sites for such disease progression is the carotid artery bifurcation, which is particularly important, as it is one of the major arteries supplying blood to the head (Fig. 1.1). The common carotid artery (CCA) originates in the aortic arch and bifurcates into the external and the internal artery at the neck level. The external carotid artery (ECA) supplies blood to the face, whereas the internal carotid artery (ICA) supplies blood to the brain. A unique feature of the internal carotid artery is its bulb at the bifurcation, referred to as the sinus. The presence of the sinus, which is a pressure regulator, increases the curvature at the bifurcation, therefore further enhances flow separation and hemodynamic stresses that make the carotid artery most vulnerable to atherosclerotic disease (Ku et al. 1985).

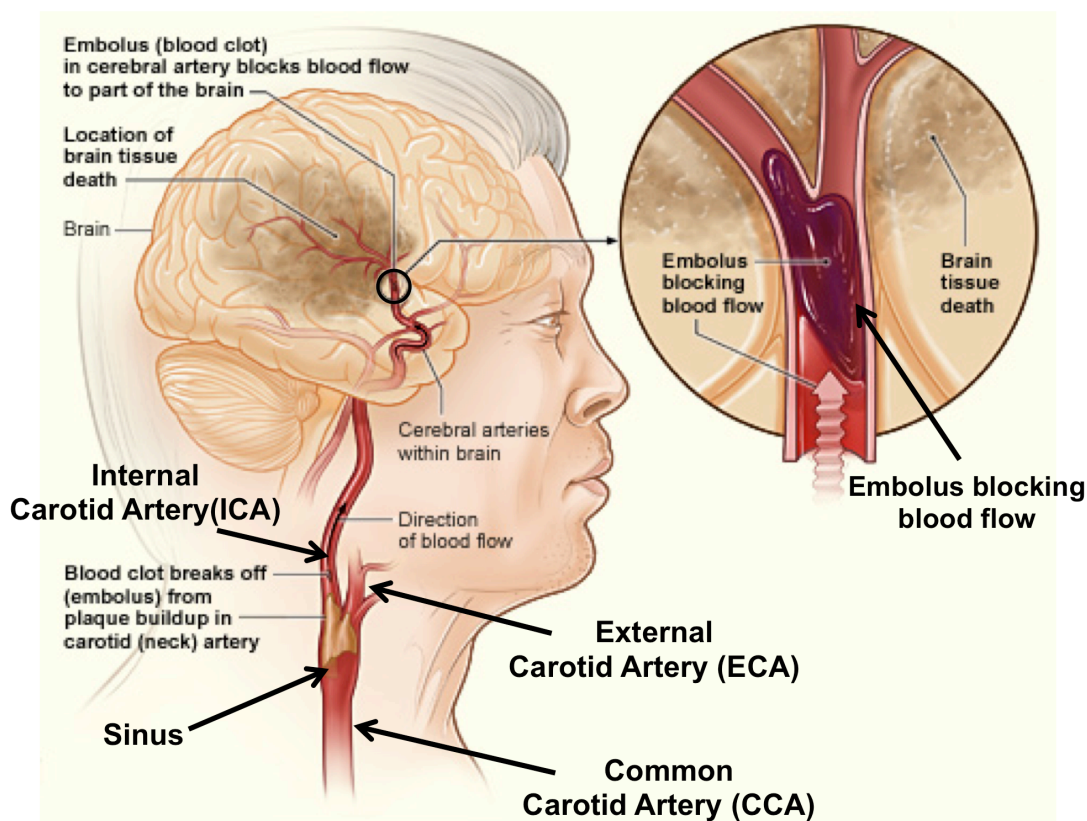


Figure 1.1: Carotid artery bifurcation showing the common, internal, and external carotid artery. The internal carotid is shown with plaque built-up and an embolus blocking the blood flow. Source: National Heart Lung and Blood Institute (NIH) (National Heart Lung and Blood Institute (NIH)) [Public domain], via Wikimedia Commons.

Large multi-center randomized clinical trials, such as the North American Symptomatic Carotid Endarterectomy Trial (NASCET) (NASCET 1991) and the European Carotid Surgery Trial (ECST) (ECST 1991), had emphasized the importance of stenosis severity as a primary risk factor of stroke. The criterion used in the NASCET clinical trial has widely been adopted as the standard definition [Eq. (1.1)] to measure stenosis severity for categorization of carotid artery disease severity, defined as the following:

$$\% \text{ Stenosis} = 100 * (1 - D_{\text{ICA,min}} / D_{\text{ICA,distal}}), \quad (1.1)$$

where $D_{\text{ICA,min}}$ is the minimum luminal diameter (in the stenosis), and $D_{\text{ICA,distal}}$ is the diameter distal (downstream) to the bulb in the ICA provided the walls are parallel and disease free (Fox 1993).

The imaging modality used in the NASCET trial was x-ray digital subtraction angiography, which is considered the gold standard for defining stenosis severity. However, the procedure is highly invasive and has been observed to cause neurological complications, negative contrast reactions and renal dysfunctions due to the iodinated contrast agent (Fayed et al. 2002). Non-invasive imaging techniques have been introduced to replace digital subtraction angiography. Currently, duplex ultrasound (Doppler and B-mode displayed simultaneously) has widely been adopted as the first-line diagnostic tool to evaluate carotid artery disease and assess the associated stroke risk (Brott et al. 2013; Gokaldas et al. 2015), and has the advantage of low cost, accessibility, portability, and non-invasive nature in comparison to its counterparts magnetic resonance imaging (MRI) and computed tomography. However, the latter techniques are used when the results from duplex ultrasound are inconclusive (Dawson et al. 1997; Back et al. 2000). The current standard strategy for stroke risk assessment for both asymptomatic and symptomatic patients has been outlined in (Brott et al. 2013), which still suggests DUS as the initial diagnostic tool.

Although stenosis severity has been considered a primary factor in assessing cardiovascular disease, studies have shown that stenosis severity is not the sole risk factor for stroke, especially in asymptomatic patients (Gupta and Marshall 2015). The plaque

vulnerability (Chalela 2009; U-King-Im et al. 2009; Huibers et al. 2015; Brinjikji et al. 2016) and abnormalities in the hemodynamics (Gupta and Marshall 2015) are two major factors, in addition to stenosis severity, that play an important role in assessing the risk of stroke. Plaque vulnerability is currently assessed primarily based on the plaque composition using MRI or ultrasound (US), and hemodynamics generally are assessed using DUS or phase-contrast MRI (PC-MRI). Vector Doppler ultrasound and ultrasound velocimetry have potential impact on improved assessment of the hemodynamics. The relevance of hemodynamics in vascular disease is described further in the next section.

1.3 Significance of Hemodynamics for Vascular Disease Diagnosis

Hemodynamic effects are associated with athero-prone bifurcations and curvatures, as well as subsequent diseased atherosclerotic stenosis (Bakker 1991; Ganger 1995; Fung 1997). Studies have shown that other vessel features, such as vessel tortuosity, surface irregularities, plaque geometries (e.g. eccentricity), as well as flow pulsatility, introduce increased abnormalities in the blood flow (Lesniak et al. 2002a; Lesniak et al. 2002b; Tang et al. 2003; Poepping et al. 2010; Wong et al. 2013; Kefayati et al. 2014). Plaque surface irregularities have been shown to change the size and/or the shape of regions with reversed or reduced flow, the behaviour of the jet (Lesniak et al. 2002a; Lesniak et al. 2002b), and significantly elevate levels of flow disturbances (Wong et al. 2013) distal to the stenosis in the carotid bifurcation. Stenosis asymmetry in arteries has shown larger flow separation regions (Tang et al. 2003) and change in size and location of the recirculation zones and path of the velocity jet (Poepping et al. 2010) compared to that of symmetric stenosis. Some of the main flow features linked with these vessel features are

the high-velocity jet, flow separation and reattachment (fluid layer separates and then reattaches with the surface of a body), vortex and eddy formation, and disturbed or turbulent flow. An example of these flow features is demonstrated in Fig. 1.2 below. High-velocity jet with a larger recirculation region is seen, which occurs due to asymmetric stenosis. The low velocity regions (in green) with varying flow directions, such as in the recirculation zones, downstream of the stenosis and near wall, are difficult to map accurately using DUS due to its angle-dependence and wall filter effect.

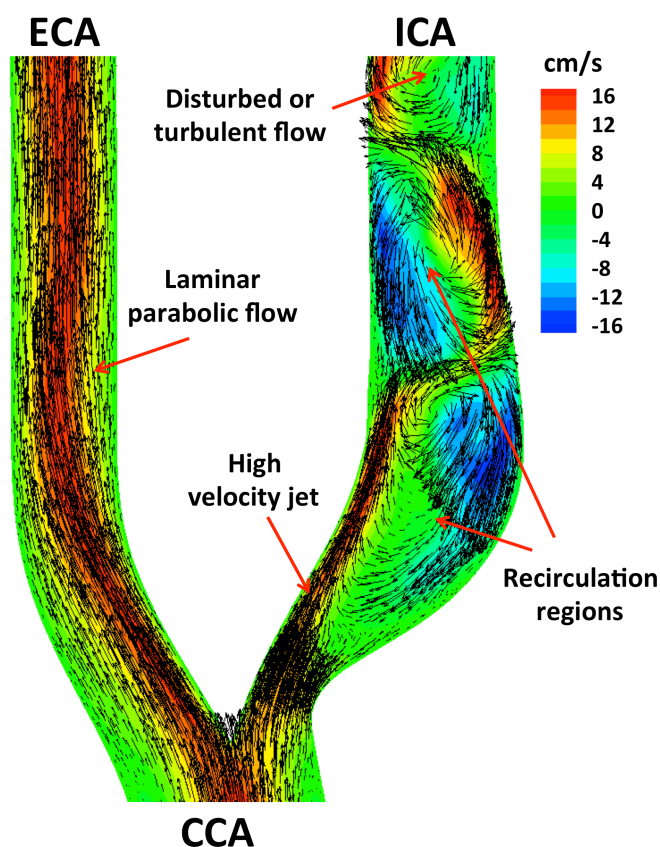


Figure 1.2: Example of a velocity map in an asymmetric 50% stenosed carotid bifurcation model generated using computational fluid dynamics. Black arrows represent velocity vectors overlaid on color-encoded map showing a range of velocities in forward and reverse direction. The presence of high-velocity jet, large recirculation regions, and downstream turbulent flow, such as vortices are shown (as labeled). (Courtesy of E. Y. Wong, Western University).

These flow features, shown in Fig. 1.2, can lead to complex patterns of low and high shear stress at the vessel wall (Zarins et al. 1983; Ku et al. 1985; Asakura and Karino 1990). Both shear stress and turbulence are known to play an important role in the initiation and progression of atherosclerotic disease such as plaque development, plaque rupture, and thrombus formation (Stein and Sabbah 1974; Reininger et al. 1995; Holme et al. 1997; Tambasco and Steinman 2003; Nesbitt et al. 2009). Studies have shown that low and oscillatory shear stress (due to pulsatile flow) is atherogenic (initiates plaque build-up), whereas high shear stress protects from plaque build-up (Malek et al. 1999). However, high shear stress regions, such as upstream of a plaque segment can cause intra-plaque hemorrhage, thinner fibrous cap and greater incidence of plaque rupture (Dirksen et al. 1998; Slager et al. 2005; Cicha et al. 2011). Once plaque is initiated, shear stress further progresses the disease causing vessel stenosis and plaque surface irregularities. These features in turn can cause further changes in the level of shear stress and turbulence. A recent review on the role of disturbed hemodynamics related to geometric features in the carotid and the coronary arteries (the two most studied arteries) on vascular disease initiation and progression has been given in Morbiducci *et al* (Morbiducci et al. 2016).

Overall, the effect of all the vessel features is encompassed in the changes in the above mentioned flow parameters. Hence, quantification and characterization of these flow parameters, such as shear stress and turbulence intensity, are important for vascular disease diagnoses, which require accurate 3D velocity vector estimations as the initial step. The work presented in this thesis focuses on accurate estimation of low blood

velocities, such as would be present in regions of recirculation and near the wall, for improved estimation of shear stress.

1.4 Modalities for *In-vivo* Blood Flow Characterization

Magnetic resonance imaging and ultrasound are the two main modalities used for non-invasive blood flow characterization *in vivo*.

For MRI, the technique for blood flow characterization is PC-MRI. It is based on the observation that changes in the MR signal phase along a magnetic field gradient are directly related to the blood flow velocity. The first *in-vivo* velocity maps using PC-MRI were presented in the early 80's (Moran 1982; Bryant et al. 1984). Recently, time-resolved ("CINE") 3D PC-MRI with velocity encoding in all three dimensions has been introduced and is increasingly used to quantify and visualize 3D hemodynamics in the human vasculature (Wigstrom et al. 1999; Frydrychowicz et al. 2007); this technique is called 4D flow. In addition to cardiovascular 3D flow mapping, 4D flow data have been used to estimate flow parameters such as turbulence intensity (Dyverfeldt et al. 2007), turbulence kinetic energy (Dyverfeldt et al. 2008), and wall shear stress (Sotelo et al. 2016). Further details and applications are discussed in recent review article (Markl et al. 2012; Ha et al. 2016).

Although MRI offers advantages in anatomic regions where acoustic windows are limited, it is time consuming, expensive, and can be invasive for patients with pacemakers and metallic implants due to its strong magnetic field. Ultrasound, on the other hand, measures blood velocities using a DUS technique. It is usually considered the first-line diagnostic tool for blood-velocity measurements due to its low cost,

accessibility, portability and non-invasive nature. A more detailed description on DUS and its background is presented in the next section.

1.5 Background of Ultrasound

This section provides a brief introduction to ultrasonography and modes used in ultrasound imaging systems. DUS for estimation of blood velocities is presented in more detail along with the basics of signal processing and the two most common velocity estimation approaches used in pulsed-wave Doppler (PWD) ultrasound. The last subsection discusses the clutter-filter limitation of the DUS systems addressed in this thesis.

1.5.1 Ultrasound

Ultrasonography was invented for underwater sonar imaging by Paul Langevin in 1923 (Chilowski and Langevin 1923). It emerged into the medical field in the late 1950's and since then has seen great advances both in the field of anatomical as well blood-flow imaging.

Diagnostic ultrasound uses frequencies ranging from 2 to 15 MHz, the choice of which provides a trade-off between imaging parameters, such as spatial resolution, depth penetration and bio-effects. Ultrasound imaging is based on the principle of transmission and reception of pulsed waves in which pulses of ultrasound frequency are transmitted from an acoustic transducer and the echoes are returned from the tissue or blood. The intensity of the returned signal depends mainly on the differences in acoustic impedance in the tissue structure and the size of the scatterers relative to the wavelength. Anatomical structure viewing takes advantage of this property by forming intensity-based images commonly known as the brightness mode (B-mode) images. The depth information from

the echoes is determined from the time of flight and the speed of sound ($\sim 1540 \text{ ms}^{-1}$ in soft tissue) to obtain a 2D structural image of the insonified region.

Other useful modes for ultrasound imaging are the amplitude mode (A-mode), motion mode (M-mode), spectral Doppler, and color Doppler (color-encoded velocity maps), where color Doppler is of primary relevance to this thesis. Currently, all clinical ultrasound systems have the capability for duplex and triplex imaging. Duplex imaging combines 2D B-mode imaging with Doppler-mode in the same system. B-mode imaging provides visual guidance, which helps in volume placement and beam-to-vessel angle determination for Doppler velocity measurements. An overlay of color flow imaging is also available on the duplex mode to obtain a triplex mode (i.e. B-mode, Doppler-mode, and color-mode ultrasound combined).

1.5.2 Doppler Ultrasound

For blood flow or tissue motion estimations, the methodology used is DUS, which uses the principle of Doppler effect – introduced by Christian Doppler in 1843 where one hears a shift in the transmitted frequency due to the relative motion of the source and the listener. The shift in the frequency is referred to as the Doppler shift, which is proportional to the relative velocity between the source and the listener. The Doppler equation for the shift in the ultrasound frequency f_d is then given by:

$$f_d = f_r - f_t = 2f_t V \cos \theta_d / c \quad (1.2)$$

where f_r is the received frequency, f_t is the transmitted frequency, V is the velocity of the reflecting target, c is the speed of sound, and θ_d is the Doppler angle, which is the angle between the ultrasound beam and the direction of motion of the target (e.g. red blood

cells). Note, since $V \cos \theta_d$ gives the magnitude of the velocity component along the received beam, the angle θ_d must be known accurately in order to obtain the correct velocity. The schematic in Fig. 1.3 shows the basic principle of DUS and the component of the scatterer velocity along the transmit and receiver beam axis.

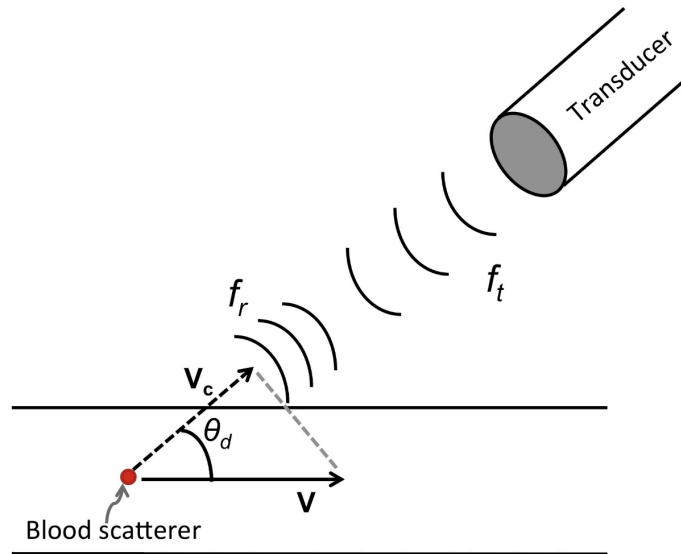


Figure 1.3: Schematic showing the basic working principle of Doppler ultrasound. Velocity component V_c along the beam direction is estimated from blood scatterer velocity, V , at a Doppler angle, θ_d .

1.5.2.1 Pulsed-Wave Doppler Ultrasound

The direct method for estimating the Doppler shift in frequency is applicable for continuous wave Doppler (CWD) method, which transmits and receives continuously. Due to continuous transmission and reception, it becomes difficult to have good depth resolution, except having a sense of the sound to be coming from a shallower or deeper region assessed from its strength (i.e. loudness) because signal from shallower regions is attenuated less. Also, the knowledge of the distance and the angle between the transmitting and receiving crystals can provide information on the depth to where the

transmitting and receiving beams might overlap. CWD is usually used in hand-held and pocket-Doppler devices for auscultation (listening to internal sounds of the body organs) of valvular movements and blood flow sounds, which may be undetected with a stethoscope. The other commonly used transmission method is pulsed-wave Doppler (PWD), introduced by Peronneau (Peronneau et al. 1976), which sends a burst of short pulses at a regular time interval (pulse repetition interval) and with a specific central frequency. The authors used a single transducer to transmit and receive alternatively from a given depth by a time-gated window. Multiple gates could also be used, which would provide a profile of velocity values across a vessel (Plett et al. 2001).

It has been shown [(Jensen 1996(a), Chp.4)] that the method for directly measuring the frequency shift as has been suggested for the classical Doppler effect could not be applied to the PWD method. As short duration pulses used in PWD correspond to broad bandwidth pulses with a particular central frequency. The frequency-dependent attenuation with depth, observed for ultrasound waves, would downshift the central frequency of the pulses. This effect makes it difficult to assess the frequency shift in the received signal specifically due to relative motion of the scatterers. Therefore, in PWD, a shift in time or phase between at least two consecutively received signals is relatable to the shift in the frequency, f_d , leading to the estimation of velocity of the scatterers using Eq. (1.2).

1.5.2.2 Basic Signal Processing of Doppler Ultrasound

A block diagram of the basic signal processing used in PWD method is shown in Fig. 1.4. In this method, bursts of short pulses of some specific central frequency are transmitted at a specified rate (the pulse repetition frequency, PRF). These pulses are generated from

the master oscillator, which controls the central frequency of the transmitted pulses and provides a reference signal for the demodulation stage. The interval between these pulses is controlled by the time-gated transmitter amplifier. The reflected received signal is amplified and low-pass filtered to improve its SNR. The signal then passes through a demodulator to remove the carrier frequency. Various demodulation techniques can be used, such as Hilbert transform, in-phase/quadrature (IQ) demodulation, or quadrature heterodyning [(Evans 2000), Chp. 6]. The aim is to obtain a complex signal with the in-phase, usually the original signal, and the quadrature signal (the signal shifted in phase by 90°).

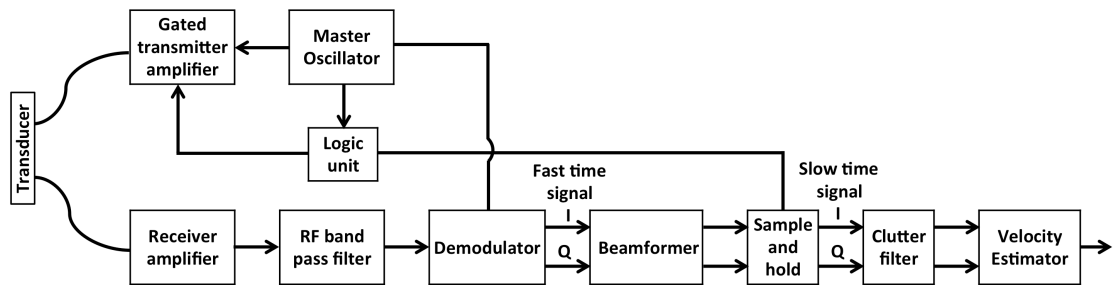


Figure 1.4: Block diagram of basic signal processing used in pulsed wave Doppler ultrasound for velocity estimations.

A low-pass filter is applied to remove the high frequency signal, which removes the sum of the frequency signal in the case of IQ-demodulation and quadrature heterodyning or removes high-frequency noise from the signal when using the Hilbert transform (method used in this thesis). The demodulated signal is then passed through a beamformer, where it is focused at various depths, and then a sample-and-hold circuit. The sample-and-hold circuit opens the receive-gate after the signal is transmitted. The time difference between the transmission of the signal and opening of the receive-gate determines the depth from

which the signal is received. The length of the pulse determines the length of the sample volume.

An example of a sampled signal at one depth is shown in Fig. 1.5. Due to the motion of the scatterers, each received signal is slightly shifted in phase relative to the previous one.

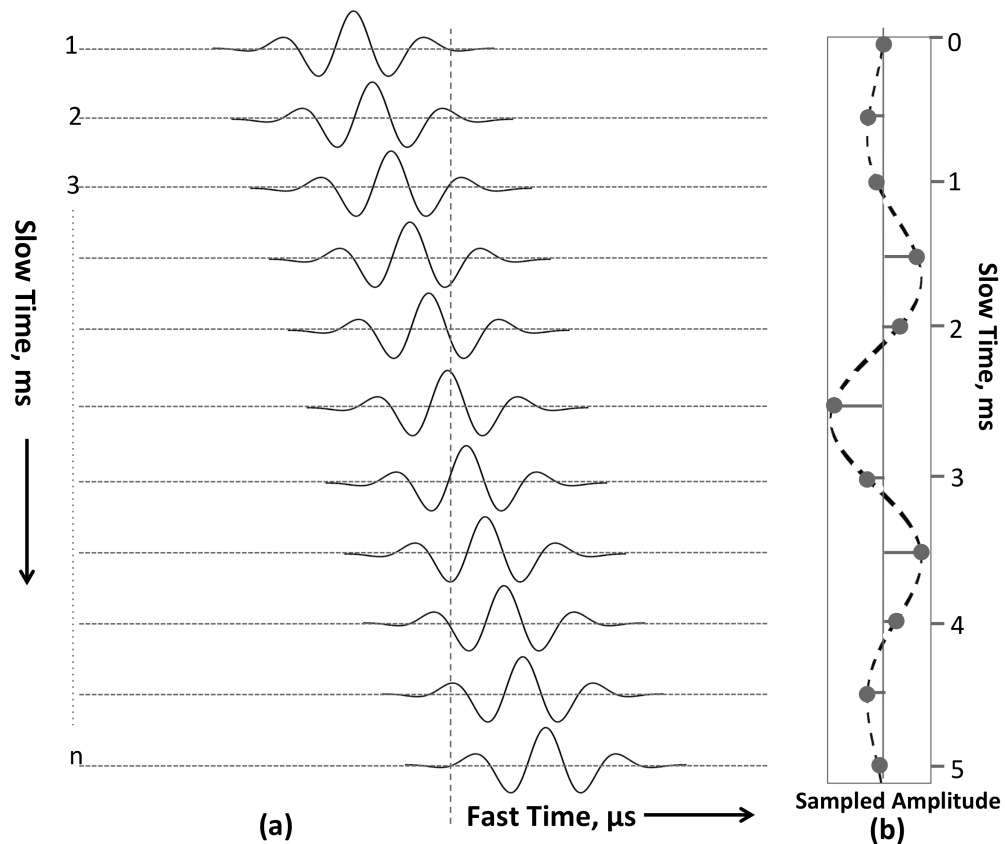


Figure 1.5: Schematic showing the sample-and-hold operation using (a) ‘n’ number of backscattered RF signal from a scatterer moving away from the transducer. First signal received when the scatterer enters the sample volume and moves away for each transmission. (b) Doppler signal (slow time signal) constructed from sampling ‘n’ RF pulses at a specified time indicated by the vertical dashed line in (a).

The signal generated from typically 8 to 20 samples is called the slow-time signal, which is then passed through a high-pass filter to attenuate the high- amplitude, low-frequency

echo signals from the stationary or nearly stationary targets, such as slowly moving vessel walls. Finally, the velocity estimator outputs the Doppler shift or the velocity magnitude and directional information (forward or reverse). The two commonly used methods implemented on clinical machines for the estimation of mean blood velocities are spectral analysis and 1D lag-one autocorrelation, which are presented in the next two subsections.

The PWD system is limited in its ability to detect velocities beyond a finite maximum dependent on PRF. To prevent interference between echoes coming from different depths, the PRF has to be low enough such that the echo received from the first pulse is received before the second pulse is transmitted. Therefore, the deeper the sample volume position, the longer the interval between the pulses needs to be. The resulting reduced PRF reduces the maximum measurable velocity that would lie within the Nyquist limit. According to the Nyquist theorem, the PRF of the transmitted pulses should at least be equal to or greater than twice the maximum Doppler frequency, which is needed to measure the velocities without being aliased. PRF needs to be reduced (increased pulse repetition interval) to measure velocities in a deeper vessel, which could become a problem when high-velocity jets need to be measured in deeper vessels or locations, e.g. in the heart. As mentioned earlier, the other two major limitations of the system are the angle dependence of the measurements, requiring *a priori* knowledge of the flow direction, and the application of the wall filter, which limits the minimum velocity that can be measured.

1.5.2.3 Mean Velocity Estimation Using Spectral Analysis

The spectral analysis method of estimating Doppler frequencies is used virtually in all clinical systems for the PWD mode. In this method, which commonly applies fast Fourier transform on the demodulated signal, a spectrum of frequencies is obtained corresponding to the range of blood velocities and to the finite beam dimensions (typically 0.5 mm for clinical scanners). A spectrogram from the sample volume of interest is displayed along with the B-mode of the vessel, together commonly referred to as the duplex mode. This capability is available on all clinical scanners. Fig. 1.6 shows a B-mode image and the velocity spectrum of the velocities within the sample volume placed in the lumen of a carotid artery flow phantom, which was used in this thesis.

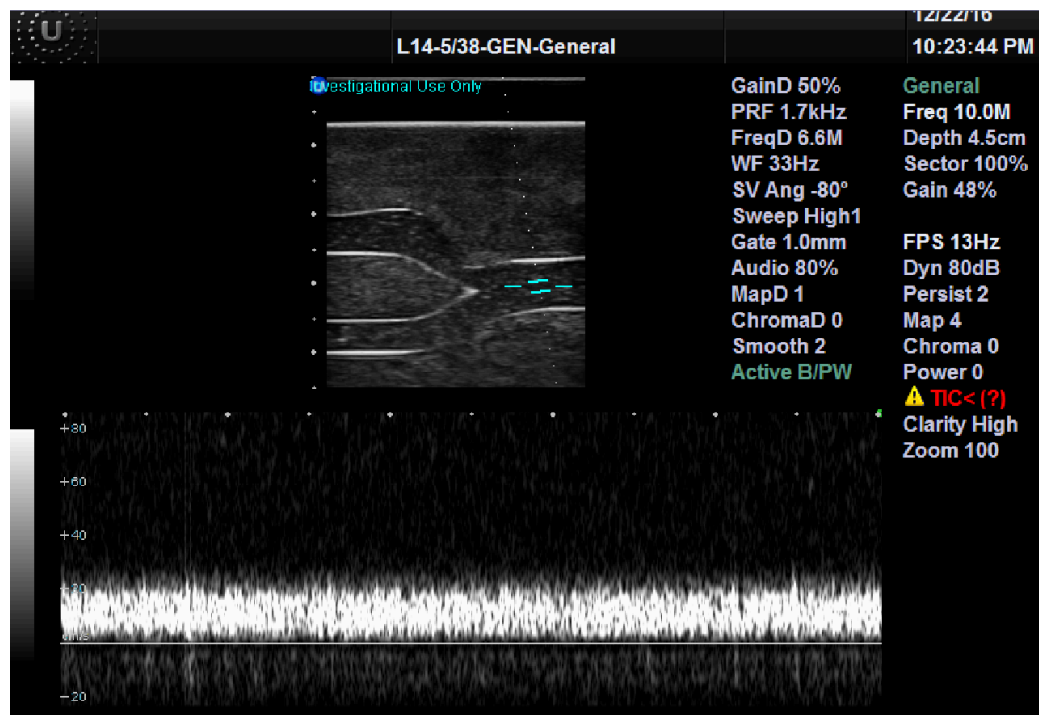


Figure 1.6: Duplex ultrasound display of a carotid bifurcation flow phantom showing a B-mode image (upper half) and Doppler spectrogram (lower half). The direction of the flow is from right to left.

Quantitative flow information, such as peak, mean, and minimum velocity, in the volume of interest can be obtained from the spectrogram.

The two most significant causes of broadening in the spectrum are the range of velocities within the sample volume and the beam width. The range of velocities within a sample volume can occur both due to intrinsic and extrinsic factors. The intrinsic factors – inherent to the measurements and to the system – are beam width and beam geometry (Newhouse et al. 1976; Newhouse et al. 1977; Guidi et al. 2000). The beam width causes transit-time broadening due to the time spent crossing the beam whereas beam geometry creates a range of insonation angles thus causing a range of frequencies received by the receiver. The extrinsic factors – associated with the nature of the velocity field – are the velocity gradient and/or varying directions in the sample volume, which can occur due to spatially or temporally varying velocity fields, e.g. due to turbulence and acceleration. (Fish 1991; Cardoso et al. 1996; Bastos et al. 1999).

Broadening of the frequency spectrum has been used in several studies to provide insight into the dynamics of flow, such as in regions of turbulence downstream of stenosis, vortices, and recirculation (Shung et al. 1984; Zuech et al. 1984; Hutchison and Karpinski 1985; Shung et al. 1992; Hutchison 1995; Cloutier et al. 1996). Since several factors mentioned above cause broadening of the Doppler spectrum, it becomes difficult to assess the exact contribution from each in practice (Hoeks et al. 1991).

1.5.2.4 Mean Velocity Estimation Using Autocorrelation

The second method for mean velocity estimation is the autocorrelation method, which estimates only the mean Doppler shift and was first introduced in 1972 (Miller and

Rochwarg 1972; Kasai et al. 1985)). In autocorrelation method, one scanline measurement is compared with another one so that it gives maximum value when correlated. The autocorrelation processor compares the echoes from two A-lines (amplitude-based signal) separated by a pulse repetition interval ($t_{PRI} = 1/PRF$). The phase difference, $\Delta\varphi$, which is related to the mean Doppler shift, \bar{f}_d , is calculated when the two A-lines correlate, as follows:

$$2\pi\bar{f}_d = (1/t_{PRI}) \Delta\varphi \quad (1.3)$$

The mean Doppler shift in terms of lag-one autocorrelation is:

$$2\pi\bar{f}_d = 1/t_{PRI} \arg(R(t_{PRI})) \quad (1.4)$$

where $R(t_{PRI})$ is the autocorrelation coefficient with a lag of one time period.

The advantage of using Eq. (1.4) is that it requires a very small number of operations, making it useful for real-time imaging. This is often used in color DUS (color-mode), which provides a 2D visual display of moving blood in the vasculature superimposed on the conventional gray-scale B-mode image. In the color-mode, only the mean velocities and the directions (forward and reverse) within a sub-area of the B-mode image are determined and then color-encoded – usually with hot shades of red to yellow for blood moving towards the transducer and cold shades of blue to cyan for blood moving away from it. An example of a triplex mode (B-mode, spectral, and color Doppler modes displayed simultaneously) is shown in Fig. 1.7, which is taken on the same carotid flow phantom shown previously (Fig. 1.6).

updating of the changes in the flow. Plane wave imaging, discussed in a later section, has improved on this limitation, increasing the frame-rate by at least 16 times than that of a standard 2D CFI system (Bercoff et al. 2011).

A good review on the development of CFI has been presented in (Evans et al. 2011; Hoskins and Kenwright 2015), with some introduction to the principles behind CFI, clinical applications, description of methods used to obtain velocity information, and some new techniques to overcome the angle dependence of CFI. Other current work on visualization includes combining plane wave imaging (PWI) with transverse oscillation technique (Lenge et al. 2015) or with some optimization algorithms (Yiu et al. 2014). In contrast, the work presented in this thesis is not aimed towards qualitative flow visualization but towards more accurate estimation of low velocities, which can be incorporated with flow visualization at a later stage.

1.5.3 Clutter Filter and its Effect on the Doppler Signal

The phase-shifted Doppler signal obtained (after demodulating the beamformed signal) has very high intensity contribution from the walls of the vessel and surrounding tissue compared to the low-intensity signal coming from the flowing blood. This signal is usually 20 to 60 dB higher than that of the blood signal. As mentioned earlier (section 1.3.2.2), a high-pass filter is applied to attenuate the high-intensity low-frequency signal of stationary or slowly moving tissue due to pulsatile motion of the walls of the arteries. Any blood signal with velocity components lying close to the wall velocities will fall within the wall filter's transition region, thus partly attenuating the blood signal and therefore reducing its SNR. This is demonstrated in Fig. 1.8, where a hypothetical frequency response of a filter is shown to attenuate the wall signal also attenuates the

blood signal that lies in the range of the wall signal. The low SNR signal leads to highly unreliable estimations of the Doppler signal for the low velocity components.

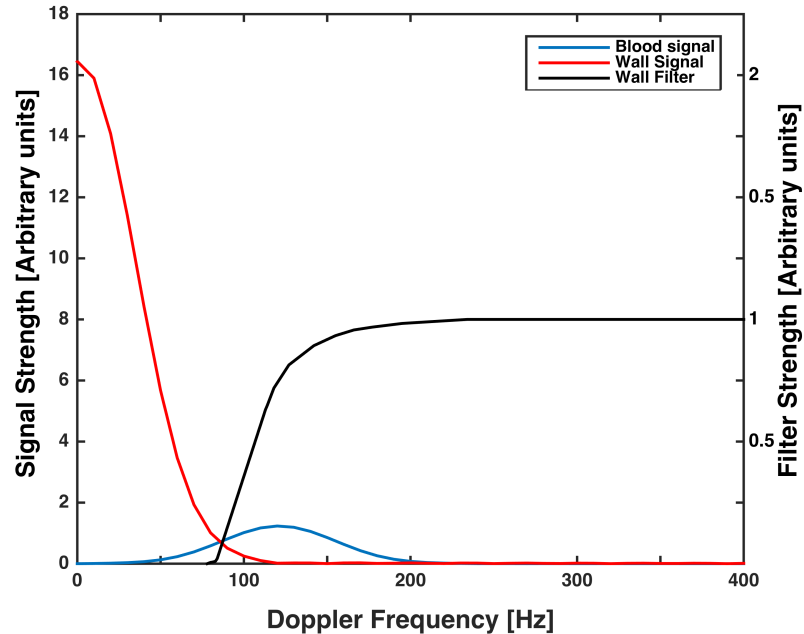


Figure 1.8: Illustration of hypothetical Doppler spectra from the high-intensity, low-frequency signal from the stationary and slowly moving walls (red) with the very low-intensity blood signal (blue). A hypothetical frequency response of a wall filter is shown in black to demonstrate its effect on the low frequency blood signal when the two signals overlap in frequency.

This limitation, common to both conventional DUS and VDUS, is especially of concern for wall shear stress measurements as the blood velocities close to the vessel wall usually lie in the lower range, thus causing difficulty in the estimation of these velocities. Without near-wall velocity estimates, various models to estimate the wall shear stress have been implemented, which make assumptions regarding the velocity profile, for example, using maximum Doppler velocity as the centerline velocity and assuming fully developed flow (Mitchell et al. 2004; Davies et al. 2006). The velocity profile is then used to extrapolate for the velocities near the vessel wall. Unfortunately, these

assumptions fail where the flow is not well behaved, such as recirculating flow in the ICA bulb and disturbed flow distal to the stenosis or where the arteries are curved (Ford et al. 2008; Manbachi et al. 2011). Several studies have demonstrated that these assumptions cause error in the wall shear estimations such as due to over-simplified model of Poiseuille flow (Leguy et al. 2009; Mynard and Steinman 2013; Mynard et al. 2013). However, the closer and more accurate velocity measurements can be made to the vessel wall, the more accurate the wall shear stress estimations will be, which can lead to improved understanding and diagnosis of arterial disease.

Recent work (Fadnes et al. 2015) made 2D vector estimations of low velocities bypassing the wall filter issue by using speckle tracking combined with PWI. However, accurate wall shear stress estimation requires 3D velocity vector estimation, especially for the low velocities spanning the wall-filter cut-off, such as in regions near the wall that include vortices, recirculation zones, or regions downstream of a destabilizing jet in a diseased artery. 3D speckle tracking with compounding could improve the accuracy of these velocities, but the method is computationally very demanding.

The work in this thesis used a crossbeam multi-receiver technique, the most commonly used VDUS technique. The crossbeam VDUS technique is discussed in more detail later in this chapter. The focus on overcoming the wall-filter limitation and reducing its impact on the accuracy of low blood velocity estimations that lie close to the wall filter cut-off is addressed in two ways.

The first study focused on investigating the potential of VDUS technique in terms of number of receivers with a suitable beam-selection method to obtain low 3D blood

velocities as close to the wall filter cut-off as possible. It is based on the argument that the estimation of a 3D velocity vector requires at least three ‘good’ (high SNR Doppler signal) estimates, but the wall filter can reduce the number of available estimates to less than three for velocities near the wall-filter cut-off thus reducing the accuracy in both the velocity magnitude and the direction. Increasing the number of receivers, when also combined with a suitable selection method, may reduce the impact of the wall filter for low blood velocities. An increase in the number of receivers will therefore increase the probability of having at least three receiver beams with a Doppler signal that exceeds the wall-filter cut-off.

In the second study, a novel technique is introduced, referred to as the ‘VDUS Aperture-Translation’ technique. In this technique, an increased phase shift is introduced in the blood velocities via aperture translation by increasing the relative velocity of the moving scatterer. This improves the SNR of the received signal as the Doppler frequencies are shifted to the passband of the filter thus improving the velocity estimates. Therefore, lower velocities even within the WF_{eff} region could be measured with better accuracy and precision. The technique is initially performed for 2D vector velocities as proof of concept.

The next section presents a background and literature review of various techniques developed for 2D and 3D blood velocity estimations with an emphasis on the crossbeam VDUS technique.

1.6 Background and Overview of Vector Doppler Ultrasound Techniques

Vector Doppler ultrasound was introduced in the early 70's to resolve the ambiguity in the velocity estimations due to the angle dependence of DUS. Several techniques have been introduced since then. The work in this thesis uses a crossbeam VDUS technique. The term crossbeam is used when one transmit beam and at least one separate receiver beam cross at an ROI with some known angle between them. Note that there are other techniques that use a crossed-beam method, but these add modifications, such as modulating the beams in different directions, as in the transverse oscillation technique (Jensen and Munk 1998; Jensen 2001), to extract the velocity information or using a signal from one beam to estimate the direction of the flow and a second one to estimate the velocity as is done in a dual-beam tracking method (Tortoli et al. 2006). In this thesis, 'crossbeam' terminology is used in its original form without any modifications. A detailed review of VDUS crossbeam technique is given in sub-section 1.6.2. However, a brief overview of other key VDUS and non-Doppler techniques using ultrasound for 2D/3D vector velocity estimation is presented here for completeness.

1.6.1 Key 2D/3D Vector Velocity Techniques

1.6.1.1 Spectral Broadening and Dual-Beam Tracking

The idea of using spectral broadening as a measure of blood velocities was introduced by Newhouse et al (Newhouse et al. 1987). A 3D vector velocity estimation method was introduced (Newhouse et al. 1994) that replaced one of the three transducers by exploiting the fact that the bandwidth of the Doppler spectrum is proportional to the velocity component perpendicular (transverse) to the beam direction (Censor et al. 1988;

Newhouse et al. 1994; McArdle et al. 1995). It reduces the number of receivers and allows blood velocity estimations in regions where flow is perpendicular to the beam axis. However, inaccuracies arise due to confounding sources of spectral broadening, such as the velocity gradient across the finite sample volume size and shape (McArdle and Newhouse 1996; Tortoli et al. 2001), noise in the signal, and geometric broadening (Bastos et al. 1999). In contrast, Tortoli et al (Tortoli et al. 2006) in their dual-beam tracking method used the transverse Doppler relation to align the beam perpendicular to the flow to determine the velocity direction. The second beam is then set at a known angle relative to the first one for Doppler measurements. It is a 2D-vector technique that assumes flow in the plane in which the two beams lie, therefore requiring another beam to remove this assumption.

1.6.1.2 Speckle Tracking (Non-Doppler Technique)

Speckle tracking was introduced in ultrasound (Trahey et al. 1987) to measure 2D blood velocities. The method is a non-Doppler technique, which tracks the speckle pattern to estimate the local particle velocities. The velocity of the particle is estimated in a kernel region from the first B-mode image and one of the surrounding same-sized regions with the best match from the next image taken after some time. It can measure velocities as low as a few mm/s, which is a challenge for other techniques due to the wall-filter cut-off, but requires high temporal resolution and extensive computing. Several methods were introduced to improve the temporal resolution and reduce the computing power of the 2D speckle tracking technique (Bohs and Trahey 1991; Bohs et al. 1998; Bohs et al. 2001; Lovstakken et al. 2006; Liu et al. 2009). A 3D speckle tracking method has been

introduced but tested only for tissue motion (Morsy and von Ramm 1998), strain imaging (Malik et al. 2016), and echocardiography (Seo et al. 2014).

1.6.1.3 Transverse Oscillation

The transverse oscillation (TO) technique was introduced by Jensen and Munk (Jensen and Munk 1998) for 2D blood flow imaging. It is based on the principle that transverse motion influences the received signal through transverse spatial modulation. It uses spatially oscillating fields in the axial direction and one or two transverse directions, for velocity estimations in 2D or 3D respectively, relative to the transducer. The velocity components along these directions are estimated from the measurements of their in-phase and quadrature signals. The method employs the currently used conventional phase-shift estimation processing and therefore has similar limitations as that of a crossbeam technique. The TO technique has been tested through simulations (Udesen and Jensen 2006), validated in vivo (Hansen et al. 2009a; Hansen et al. 2009b; Hansen et al. 2011), and tested for real-time 2D velocity vector estimations (Hansen et al. 2014b; Pedersen et al. 2014). The 3D TO system has been tested and evaluated (Pihl et al. 2012; Pihl and Jensen 2014; Pihl et al. 2014) in Poiseuille flow to obtain the 3D velocity vector estimation with good accuracy for higher velocities (≥ 50 cm/s). Review on the development of this technique can be found here (Jensen et al. 2012; Jensen et al. 2013).

1.6.1.4 Vector Velocity Techniques with PWI

Recently, several new 2D vector methods have emerged that use PWI, where the entire width of the region of interest is insonified simultaneously using a plane wave. The main aim of PWI is to improve the temporal resolution for real-time visualization. PWI for medical applications was introduced in 2002 (Tanter et al. 2002). Bercoff *et al.* (Bercoff

et al. 2011) introduced an ultrafast compound Doppler imaging technique in which backscattered signals from several tilted planes were coherently summed to produce high-resolution images. These new 2D vector methods coupled with PWI for ultrafast vector Doppler imaging include speckle tracking (Fadnes et al. 2015), transverse oscillation (Jensen and Munk 1998), multi-gated Doppler (Ricci et al. 2014), vector projectile imaging (Yiu et al. 2014), frequency-domain imaging (Lenge et al. 2014) plane-wave excitation (Hansen et al. 2008; Flynn et al. 2012; Ekroll et al. 2013; Hansen et al. 2014a), and 2D cross-correlation (Udesen et al. 2008). These techniques demonstrate the capability of producing ultrafast high quality images in a 2D plane and thus providing only 2D velocity estimations. For these 2D velocity vector techniques, an underestimation of velocities occurs when the flow is out of the imaging plane. To obtain an estimate of the out-of-plane velocity magnitude component, Osmanski (Osmanski et al. 2015) used a spectral-bandwidth technique in conjunction with PWI for simple Poiseuille flow. A review article (Tanter and Fink 2014) on PWI is available for the interested reader. A comprehensive review on the state-of-the-art vector-flow imaging techniques, both Doppler and non-Doppler, is given in recent review articles (Jensen et al. 2016a; Jensen et al. 2016b).

1.6.2 Crossbeam VDUS Technique

The crossbeam technique is the most fundamental technique used in VDUS. The first VDUS system was implemented as a 2D crossbeam technique (Fahrbach 1970; Fahrbach 1973). It used two single-element transducers transmitting and receiving from both, referred to as transceivers. The beams crossed perpendicular to each other at a region of interest. The resultant velocity was estimated using simple trigonometry. A more

generalized form of Fahrbach's system was later developed (Peronneau 1974), which would work for any angle between the two transceiver beams (Fig. 1.9). The 2D VDUS systems successfully estimated the resultant 2D-vector velocity in the plane formed by the two receiver beams using PWD triangulation (Umetsu 1981) to quantify blood flow measurements in superficial arteries. The estimated velocity magnitude, $|\vec{V}|$, and its direction, θ_1 , relative to transceiver 1 were given as follows:

$$|\vec{V}| = c/(2f_t \sin\delta) \sqrt{f_1 + f_2 - 2f_1 f_2 \cos\delta} \quad (1.5)$$

$$\theta_1 = \tan^{-1}(\cos\delta - f_2/f_1)/\sin\delta \quad (1.6)$$

where f_t is the central transmit frequency, f_1 and f_2 are the Doppler frequencies measured from transceivers 1 and 2 respectively, and δ is the angle between them.

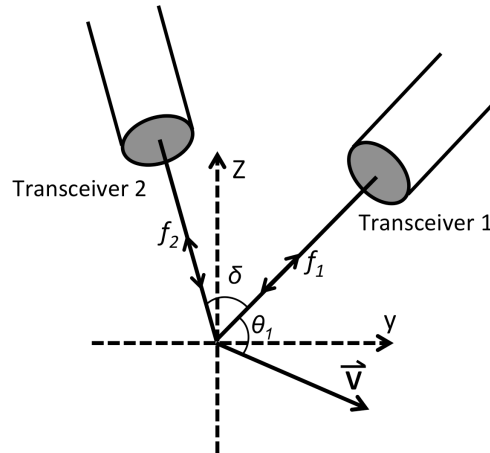


Figure 1.9: Schematic of a general crossbeam vector Doppler ultrasound system for estimation of 2D velocities with two transceivers separated by an angle δ .

The first 3D-vector crossbeam system was introduced by Daigle *et al.* (Daigle 1974) which consisted of three transceivers for independent (non-simultaneous) flow measurements and a fourth central transceiver for wall motion. Later, Fox and Gardiner

(Fox and Gardiner 1988) used only three transceivers to measure the higher jet velocities. A detailed summary on the development and the design of 2D and 3D-vector crossbeam techniques has been presented in a review article (Dunmire et al. 2000).

The initial VDUS systems were a single-element design, which were later implemented on a linear or a 2D array by grouping elements into sub-apertures (Papadofrangakis et al. 1981) acting as dedicated transmitter and receivers or all transceivers. The single-element design gave flexibility in the range of inter-beam angles and the acquisition depth but required mechanical adjustment to change the angle and the imaging depth. The mechanical adjustment could cause sample volume misregistration due to possible misalignment of multiple beam crossings. Also, larger angles and greater acquisition depth would increase the overall size of the probe. On the other hand, the sub-aperture design electronically steered the beams to change the inter-beam angle and the acquisition depth. This sub-aperture design reduced the sample volume misregistration errors and allowed multi-gating (acquisition from multiple depths by electronically sliding the aperture) and dynamic focusing (re-adjustment of focusing when changing the ROI), both of which are necessary for real-time 2D acquisitions. Although arrays could be smaller in size, this tends to limit the range of inter-beam angles and the acquisition depth. Currently, several research systems are available (e.g. Ultrasonix, Verasonics, and Visualsonics), which have the capability of acquiring simultaneously from all channels and allow separate transmit and multi-receiver sub-apertures.

To obtain 3D velocity estimations, a 2D-array could be used. A simulated version of a 2D-array, such as used in this work, can be achieved by using a linear array rotated about a central transmit-beam axis to mimic the out-of-plane receiver beams as in a 2D

array. The data acquisition in this case would not be simultaneous and error in velocity estimations may occur for time-varying flow (e.g. pulsatile flow, vortex shedding), as each receiver beam potentially would obtain a signal from an uncorrelated set of scatterers at a later time. However the method suffices for steady flow velocity estimations as was used in this work.

The crossbeam technique suffers from the same limitations as other VDUS techniques, such as aliasing, frequency-dependent attenuation, and intrinsic spectral broadening. However, limitations specific to the crossed beam method due to multiple beam crossing have been identified as sample volume translation and angle misregistration, which cause bias in the velocity vector estimation of multi-receiver crossbeam systems (Ashrafzadeh 1988; Steel and Fish 2003; Steel et al. 2004). Although, as mentioned above, linear and 2D arrays minimize the volume misregistration errors inherent in the single-element systems, the refraction errors are still present which are due to tissue inhomogeneity causing sample volume translation.

Crossbeam VDUS systems have successfully been used in a wide range of applications. Some examples are velocity mapping of spiral flow in prosthetic grafts for peripheral arterial disease (Kokkalis et al. 2013) and for arteriovenous fistula (Kokkalis et al. 2015), estimation of post-stenotic flow disturbances (Dunmire et al. 2001), mapping of blood hemodynamics in a diseased carotid artery (Forsberg et al. 2008; Tortoli et al. 2015), and wall shear stress measurements in the carotid artery (Akagawa 2016). Recent work by Tortoli *et al.* (Tortoli et al. 2015) has demonstrated an overestimation in the peak systolic jet velocity when using spectral Doppler. The accuracy in the velocity estimation

improved when 2D VDUS system was used, justifying the need for implementing VDUS as a clinical diagnostic tool.

1.6.2.1 3D-VDUS Crossbeam Systems

To date, 3D crossbeam-VDUS systems, which used separate central transmit (Tx) surrounded by multiple receiver (Rc) probes, consisted of three, four, and six receivers (3R, 4R, and 6R) symmetrically surrounding the central transmit (Fox and Gardiner 1988; Dunmire 1998; Calzolari et al. 1999; Vilkomerson et al. 2005). Fox and Gardiner (Fox and Gardiner 1988) introduced a 3R VDUS system and tested velocities of 10 cm/s and higher. Calzolari *et al.* (Calzolari et al. 1999) assessed a 3R system with a thread phantom for velocities ranging from 33 to 133 cm/s for varied angles with an inter-beam angle of 15.5°. Dunmire *et al.* (Dunmire 1998) designed a 4R configuration probe and qualitatively showed its potential to measure post-stenotic disturbances (Dunmire et al. 2001). Vilkomerson *et al.* (Vilkomerson et al. 2005) fabricated a 6R prototype to measure high jet velocities *in vivo*. Three receiver beams oriented in 3D space may likely be sufficient for such velocity ranges, but it becomes challenging to accurately measure low 3D vector velocities (≤ 2 cm/s) that lie close to the wall and are greatly attenuated by the wall filter, for reasons previously explained in section 1.3.3. Such a range of velocities may require a greater number of receivers oriented in 3D space with an optimal inter-beam angle, the choice of which may be affected by factors such as the magnitude and orientation of the velocity vector, beam-selection criterion, and/or the choice of wall filter parameters. The choice of filter parameters is usually limited by the frequencies of the clutter signal present, thus affecting the velocity signal preserved in that range. The impact of this limitation can be lowered either by increasing the number of receiver

beams (>3) and carefully eliminating the ‘noisy’ beams, by applying a suitable beam-selection criterion, with an optimal inter-beam angle or by improving the SNR of these velocity components. In this thesis, the results in Chapter 3 address the wall-filter limitation by investigating the benefit of increasing the number of receivers and applying a suitable beam-selection criterion, whereas Chapter 4 tackles this limitation by demonstrating a method of increasing the Doppler shift and thus improving the SNR of the retained signals from low velocity components.

1.7 Research Objectives and Thesis Outline

Accurate and early diagnosis of vascular disease in large arteries is important in management of the disease and possible prevention of fatal incidences such as stroke and heart attack. As discussed in Section 1.1.2, hemodynamic factors play a key role in vascular hemostasis and vascular disease progression (Kwak et al. 2014). The effects of these factors are encompassed in the changes in the level of shear stress and turbulence, which are known risk factors for initiation and progression of vascular disease (Stein and Sabbah 1974; Reininger et al. 1995; Holme et al. 1997; Tambasco and Steinman 2003; Nesbitt et al. 2009). Accurate measurement and mapping of 3D blood velocities is essential for improved estimation of shear stress and turbulence, especially low blood velocities that are near the vessel wall, in recirculation regions, and dissipative flow distal to the stenosis.

Currently, DUS is the first line diagnostic tool for noninvasive blood flow imaging, but suffers from angle dependence and wall-filter limitations for 3D and low blood velocities, as explained earlier. Vector Doppler ultrasound implementing at least three beams oriented in 3D-space can overcome the angle-dependence limitation if the

velocity components along each beam exceed the wall-filter cut-off. However, for low velocities, initially applying more than three possible receiver beams may be helpful, along with an appropriate beam-selection criterion or a method for improved SNR of the low velocity signals along each component.

The overall goal of the work in this thesis is to improve the estimation of low blood velocities using two Doppler methods – multi-receiver and aperture-translation methods – which target the improvement of the estimations of individual velocity projections by optimizing the number of receivers and their orientations with a suitable beam-selection criterion or by reducing the variability of these velocity projections to improve the estimation of low 3D-vector velocities.

The primary objectives are as follows:

- I. Theoretically determine the performance of various multi-receiver configurations in terms of minimum inter-beam angle for which ≥ 3 receiver beams exceed the wall-filter cut-off for all velocity orientations in 3D-space.
- II. Experimentally assess the benefit of increasing the number of beams while using a reasonable inter-beam angle and choice of beam-selection criteria to achieve accurate and reliable estimation of 3D velocities whose Doppler shifts lie near the wall-filter cut-off.
- III. Investigate the potential of a novel technique that uses translating apertures for accurate and reliable estimations of low velocities that lie within the wall-filter cut-off.

The following sections outline the content of each chapter, where the contributions of co-authors for each work were previously given in the ‘Co-Authorship Statement’, p. (iii).

1.7.1 Chapter 2: Methods and Materials

This chapter describes the apparatus and experimental setups used in this thesis, methods for data acquisition and data processing for the studies presented in this thesis, and the algorithm used for velocity reconstruction from multiple velocity components. The theoretical analysis was performed using a single 3D velocity vector, and experimental data were acquired in simple Poiseuille flow using a gravity-flow setup. For the initial development of these methods, it was necessary to use simple Poiseuille flow instead of complex flow (such as relevant in the ICA of a carotid). Therefore, preliminary experiments were completed in a straight vessel with the idea that the developments could be applied in the future to more complex geometries (e.g. stenosed carotid bifurcation) as suggested in the future work in Chapter 5. Data acquisition and data processing for the first study was part of the published work “Investigation of Crossbeam Multi-Receiver Configurations for Accurate 3D Vector Velocity Estimation”, in *IEEE Transactions on Ultrasonics Ferroelectrics and Frequency Control*, vol. 63, pp. 1786-1798, Nov 2016.

1.7.2 Chapter 3: Crossbeam Multi-Receiver Configurations

This chapter addresses the first two objectives stated above. It presents the results and discussion for work aimed at accurate and reliable estimation of low 3D blood velocities. In this work the potential benefit of various multi-receiver configurations, oriented at various inter-beam angles, is assessed and the effect of different beam-selection criteria is

studied. A major portion of the work is part of an article entitled “Investigation of Crossbeam Multi-Receiver Configurations for Accurate 3D Vector Velocity Estimation”, which has been published in *IEEE Transactions on Ultrasonics Ferroelectrics and Frequency Control*, vol. 63, pp. 1786-1798, Nov 2016.

1.7.3 Chapter 4: Vector Doppler Ultrasound Aperture-Translation

The work in this chapter presents the results and discussion of a novel technique ‘VDUS aperture translation’ to improve the estimation of low blood velocities that lie close to and within the WF_{eff} . The results of the two versions of the technique – mechanical and electronic translation of the aperture – are presented and compared with the conventional 2D VDUS technique. The work will form the basis for a manuscript to be submitted to *IEEE Transactions on Ultrasonics Ferroelectrics and Frequency Control*.

1.7.4 Chapter 5: Summary, Conclusion, and Future Directions

This chapter closes the thesis with the summary and conclusion of the presented work and suggests future studies to extend this work.

Chapter 2

2 Materials and Methods

This chapter describes the apparatus and the methodology used, as well as the related theory and principles for the work presented in this thesis. The velocity reconstruction theory for the crossbeam multi-receiver study and the working principle for the aperture-translation study are explained in section 2.1. Section 2.2 describes the apparatus; section 2.3 describes phantom fabrications and flow setup. Data acquisition and processing is described in section 2.4.

2.1 Theory and Principles

2.1.1 Velocity Vector Reconstruction from Doppler Shifts

The equations presented here are used in this thesis for pulsed-wave vector Doppler velocity reconstruction for N receivers arranged symmetrically around a central transmit beam axis. The mean Doppler frequency (f_n) of an n^{th} receiver, where the mean is defined based on the ensemble, is given by [Eq. (2.1)] (Calzolari et al. 1999):

$$f_n = -\frac{f_t}{c}(\vec{V} \cdot \hat{i}_o + \vec{V} \cdot \hat{i}_n) \quad (2.1)$$

The index n takes values from 1 to N , f_t is the transmitted signal frequency, c is the speed of sound in tissue, \vec{V} is the 3D velocity vector, and \hat{i}_o and \hat{i}_n are the unit vectors along the transmit beam and n^{th} receiver beam directions, respectively, as illustrated in Fig. 2.1(a). The velocity component $\vec{V} \cdot \hat{i}_o$ along the transmit axis and $\vec{V} \cdot \hat{i}_n$ along the n^{th} receiver are:

$$\vec{V} \cdot \hat{i}_o = -V_z \quad (2.2)$$

$$\vec{V} \cdot \hat{i}_n = -(V_x \sin \beta \cos \phi'_n + V_y \sin \beta \sin \phi'_n + V_z \cos \beta) \quad (2.3)$$

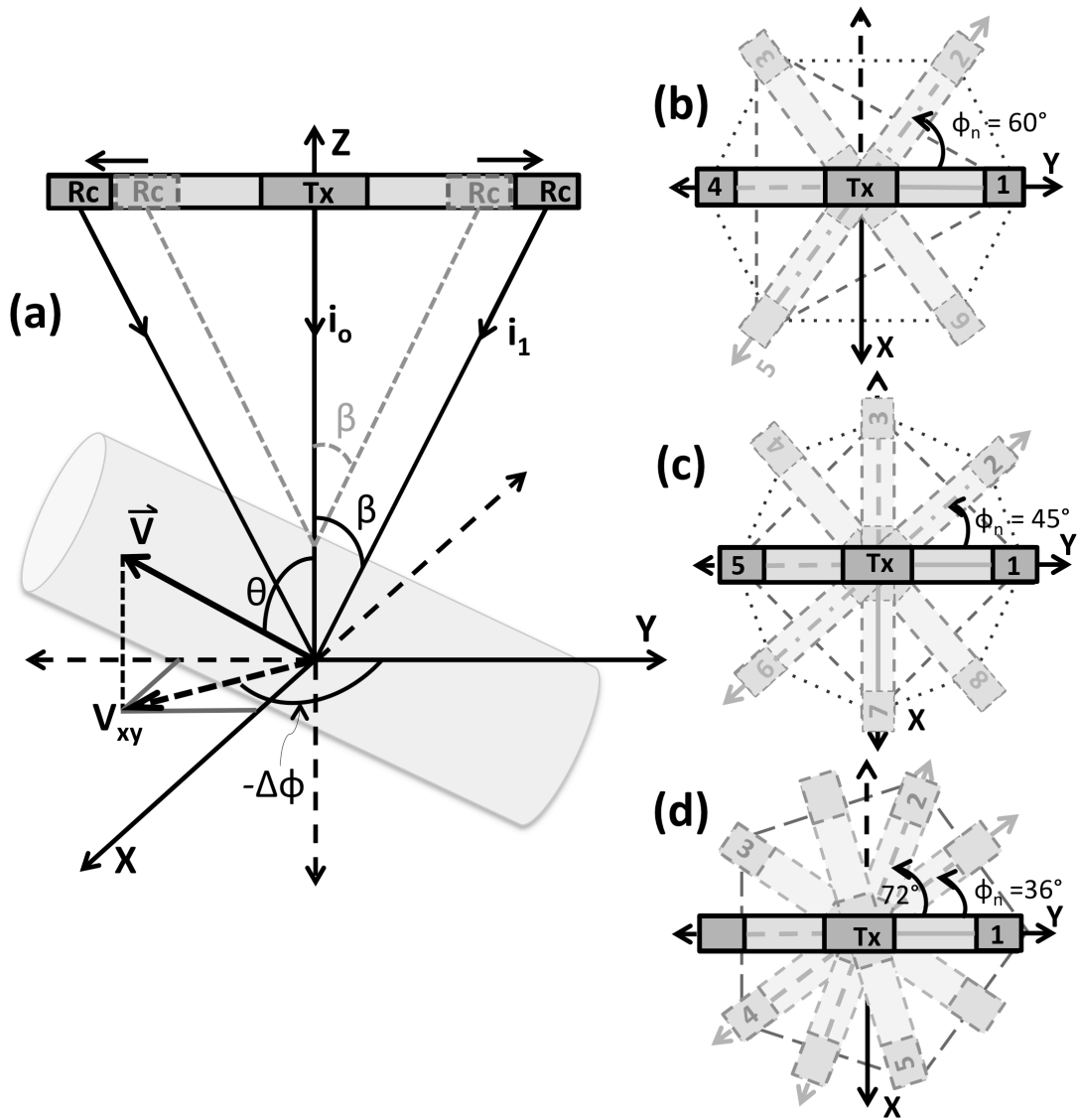


Figure 2.1: (a) Schematic of a linear array showing the central-transmit aperture and two sliding receiver apertures (labeled Rc) to maintain constant inter-beam angle (β) with changing depth. The 3D velocity vector with magnitude V and direction specified by θ (elevation angle) and $\Delta\phi$ (azimuthal rotation angle) is shown. (b) Top view of the linear array showing azimuthal rotations of $\phi_n = 60^\circ$ and 120° (in gray) to simulate a 3R and 6R, (c) 4R and 8R, and (d) 5R configurations. The dotted and dashed lines in (b, c, & d) show geometric shapes and receiver orientations used for each configuration.

The parameter β is the inter-beam angle, and ϕ'_n is the azimuthal angle that the n^{th} receiver makes relative to the x axis. The general relation to calculate ϕ_n for an NR configuration with N receivers uniformly spaced around the transmit axis (z axis) is given as follows:

$$\phi_n = 2\pi(n-1)/N \quad (2.4)$$

$$\phi'_n = \phi_n + \pi/2 \quad (2.5)$$

For an NR configuration, using [Eq. (2.2)] and [Eq. (2.3)] in [Eq. (1)], N simultaneous equations are generated and can be solved for V_x , V_y , and V_z velocity components from the known Doppler shifts, f_n , inter-beam angle, β , and azimuthal angle, ϕ'_n . Note that when the number of simultaneous equations exceeds three ($n > 3$), a linear least-squares method was used to solve for the three velocity components.

2.1.1.1 Velocity Reconstruction Algorithm for Two Receivers

A velocity reconstruction algorithm was developed to obtain the resultant velocity when Doppler shifts from only two receivers were available for NR configurations with $N \geq 3$. The algorithm determines the in-plane velocity vector from the Doppler shifts that contribute to the estimation of the resultant velocity. The 3D orientations of vectors (\vec{B}_1 and \vec{B}_2) of the two receiver beams with respect to the 3D global reference system defined in Fig. 2.1 are given as:

$$\vec{B}_1 = a_1\hat{i} + b_1\hat{j} + c_1\hat{k} \quad (2.6)$$

$$\vec{B}_2 = a_2\hat{i} + b_2\hat{j} + c_2\hat{k} \quad (2.7)$$

The coefficients $a_1, a_2, b_1, b_2, c_1,$ and c_2 are determined from each beam's orientation relative to the global reference system.

A local 2D orthogonal reference axis was set up with one axis \hat{u}_1 taken along vector \vec{B}_1 such that:

$$\hat{u}_1 = \vec{B}_1 / |\vec{B}_1| \quad (2.8)$$

The unit vector normal to the plane of the two receiver vectors is then:

$$\hat{n} = \vec{B}_1 \times \vec{B}_2 / |\vec{B}_1 \times \vec{B}_2| \quad (2.9)$$

The second axis orthogonal to \hat{u}_1 is:

$$\hat{u}_2 = \hat{n} \times \hat{u}_1 \quad (2.10)$$

The coefficients of \vec{B}_1 and \vec{B}_2 in the new reference axis are given by:

$$C_{ij} = \vec{B}_j \cdot \hat{u}_i \quad (2.11)$$

For $i = 1, 2$ and $j = 1, 2$, the resultant velocity components c_1 and c_2 along \hat{u}_1 and \hat{u}_2 , respectively, were calculated using simultaneous equations:

$$c_i = C_{ij}^{-1} v_j \quad (2.12)$$

where v_i is the velocity magnitude corresponding to receiver vector \vec{B}_i . The resultant velocity vector can now be written in the 3D global reference system as:

$$\vec{V} = \sum_{i=1}^2 (u_{ix} c_i \hat{i} + u_{iy} c_i \hat{j} + u_{iz} c_i \hat{k}) \quad (2.13)$$

The magnitude and direction are:

$$|\vec{V}| = \sqrt{V_x^2 + V_y^2 + V_z^2} \quad (2.14)$$

$$\Delta \phi = \tan^{-1}(V_y/V_x) \quad (2.15)$$

$$\theta = \cos^{-1}(V_{yz}/|\vec{V}|) \quad (2.16)$$

where $\Delta \phi$ is the azimuthal angle and θ is the elevation angle of the velocity vector. The algorithm provides the 3D directional information of the resultant velocity vector but in the plane of the two receivers. The velocity magnitude agrees well with the relation derived by Steel and Fish (Steel and Fish) but provides the directional information in terms of the global rectangular coordinate system.

2.1.2 Basic Equations

2.1.2.1 Poiseuille's Law

Steady-state parabolic flow in straight vessels was used for testing, where the theoretical parabolic velocities were calculated using Poiseuille flow conditions as follows:

$$V = V_{max} (1 - r^2/R^2) \quad (2.17)$$

for which V is the velocity magnitude at a distance r from the central axis of the tube, and $V_{max} = 2(Q/\pi R^2)$ is the peak velocity at the center of the tube of radius R with flow rate Q .

2.1.2.2 Velocity Bias and Relative Error

The mean bias, $\bar{\epsilon}_x$, and mean relative error, $\bar{\epsilon}_r$, are calculated as below:

$$\bar{\epsilon}_x = 1/m \sum_{i=1}^m |x_i - X_t| \quad (2.18)$$

$$\overline{\epsilon}_x = 1/m \sum_{i=1}^m (|x_i - X_t|/X_t) \quad (2.19)$$

where x_i is the i th experimental value and X_t is the theoretical value. The index i runs from 1 to m measurements.

2.1.2.3 Standard Deviation and Standard Error

The standard deviation, σ_x , and standard error, $SE_{\bar{x}}$, formulae are given below:

$$\sigma_x = \sqrt{\sum_{i=1}^m (x_i - \bar{x})^2 / m - 1} \quad (2.20)$$

$$SE_{\bar{x}} = \sigma_x / \sqrt{m} \quad (2.21)$$

2.1.3 Vector Doppler Ultrasound Aperture-Translation Principle

The aperture-translation method relies on a simple concept of relative motion. It adds a velocity to the moving or stationary scatterers either by mechanically translating the transducer (M-sweep) or simulating this motion electronically, i.e. sweeping the transmit-beam electronically along the linear array (E-sweep). Motion in both cases is established opposite to the velocity of the scatterers to increase their relative velocity with respect to the DUS pulse. A schematic is shown in Fig. 2.2 representing the transmit-sweep motion with a sweep velocity vector, \vec{V}_s , opposite to the flow velocity vector, \vec{V} , which is along the +y-direction. Note that for the M-sweep method, the physical translation of the linear array causes changes in the location of the transmit-receive apertures relative to the scatterers. For the E-sweep method the transmit-aperture (Tx_1) with receiver apertures (Rc_{L1} and Rc_{R2}) on each side are electronically stepped along the linear array with a

minimum step-size of one element-pitch. The estimated resultant relative velocity, \vec{V}_R , is the vector sum of flow and the sweep velocity vector:

$$\vec{V}_R = \vec{V} + \vec{V}_S \quad (2.12)$$

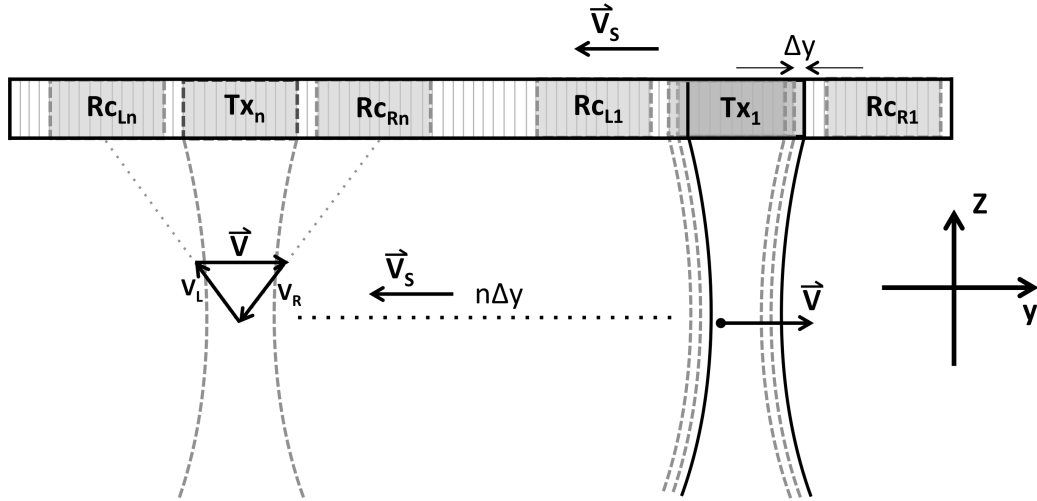


Figure 2.2: Schematic showing a transmit-aperture with left and right receive-apertures swept along the length of the linear array, i.e. $-y$ direction. The transmit-sweep velocity, V_S , is opposite to the flow velocity vector, V . V_S is the velocity of the transmit-receive apertures for E-sweep or the velocity of the transducer for the M-sweep method. The step size of the motion is equal to the element-pitch of the transducer, Δy in the E-sweep, whereas for M-sweep it is the distance travelled by the transducer during one pulse repetition period.

Fig. 2.3 demonstrates the working principle for the two methods. Only one of two receive-beams (left) is shown in the schematic for clarity. The displacement, Δy , of the transmit aperture from Tx_1 to Tx_2 between two consecutive pulses is the element-pitch of the transducer for the E-sweep method or the distance travelled by the transducer for the M-sweep method. Fig. 2.3(a) shows the echoes coming from two different locations but from the same moving sample volume [Fig. 2.3(b)] if Δy were smaller than the lateral size of the sample volume. These echoes are received at different locations along the array as the receiver aperture also moves with the transmit aperture, keeping a constant

inter-beam angle. Therefore, the distance travelled by each echo is different, introducing a path difference, Δd , related to the phase difference, $\Delta\phi$, by the relation below:

$$\Delta\phi = (2\pi/\lambda) \Delta d \quad (2.13)$$

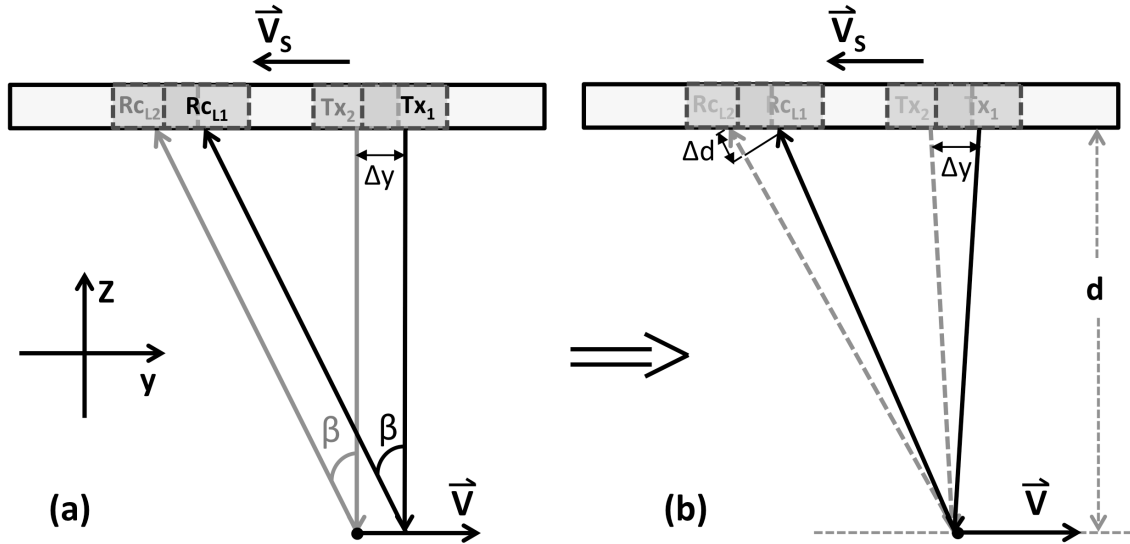


Figure 2.3: Schematic for working principle for both the M-sweep and E-sweep methods. (a) An exaggerated step Δy is shown for two consecutive transmit pulses from depth, d , received with an interbeam angle, β . (b) Schematic showing signal received from the same sample volume but received at a distance Δy away from the first receiver location. The path difference due to the receiver displacement is Δd .

This additional phase difference accounts for the increase in the Doppler frequency, hence the resultant flow velocity along the sweep direction.

There can be different ways to introduce this phase difference. One way would be to electronically move the receive-aperture while keeping the transmit-aperture at a fixed location. Another would be to move only the transmit-aperture keeping the receive-aperture fixed. Theoretically, both methods work but would require un-equal and

fractional steps to maintain a constant path-difference as the aperture (receive/transmit) moves away from the fixed aperture. In practice, the minimum step-size possible on a linear array is its element-pitch (0.3 mm for the array used in this study). A step-size of a fraction of the element-pitch is not possible. Alternatively, making the element-pitch extremely small, i.e. 0.01 mm, which is impractical, could allow more flexibility in choosing a step-size equal to multiples of the element-pitch. A different approach demonstrated in Fig. 2.3, in which both transmit and receive apertures are translated to maintain a fixed step-size and a constant inter-beam angle, is presented in this thesis.

2.2 Apparatus and Experimental Setup

The experimental setup and apparatus used for data acquisition, along with their key specifications, are described in this section.

2.2.1 SonixRP System

The SonixRP (Ultrasonix Corporation) scanner is a diagnostic ultrasound system with a programmable research interface, which allows control over transmit and receive parameters. The transmit beam can be programmed to introduce delays and steering, while the receive beam can be programmed to apply delays, focusing, steering, and apodization (reduce the affect of side-lobes). The scanner provides 128 channels where a maximum of 64 elements can be active for a single transmit at any given time. The transmit pulse can be a maximum of 96 samples at sampling rates of 40 MHz or 80 MHz. The receive-beam, with a maximum aperture of 32 elements, is digitized at a 10-bit resolution with 20 MHz RF sampling. Besides other common imaging modes available in all ultrasound scanners, the SonixRP includes an RF-imaging mode to allow

acquisition of raw RF-data (i.e. modulated pre-filtered data). It uses the Microsoft Windows XP Professional operating system. Work in this thesis uses the scanner with SonixDAQ component (explained below); specifications for the received data match that of the SonixDAQ.

2.2.2 SonixDAQ

The SonixDAQ (Ultrasonix Corporation) is a data acquisition plug-in module, which allows simultaneous acquisitions from multiple channels, for collecting raw (RF data) ultrasound data. Its relevant capabilities for the study in this thesis are discussed here briefly, whereas a detailed description of the design and its functionality is found in (Cheung et al. 2012). The receive end of the module is connected to a SonixRP scanner via one of the probe-connector ports to capture raw pre-beamformed received-data from all 128 channels simultaneously with no control over transmits. The data are digitized, after amplification and filtering, with a 12-bit resolution at a sampling rate of 40-MHz. Internal and external triggering and clocking is available at 40 MHz and 80 MHz; the work in this thesis uses an external trigger with a clocking rate of 40 MHz. The module uses field-programmable gate arrays, which allow programming of functions such as, controlling of the transmit/receive switches, defining time-gain compensation curves, and coordinating data retrieval. The maximum data buffer size is a 16 GB RAM, which can capture received data from about 8,000 to 25,000 transmit firings, depending on the acquisition depth. This captured data is then transferred to a Windows based computer through a USB port.

2.2.3 TEXO Software Development Kit

Several software development kits (SDK) are provided with the SonixRP, which can be used to control and perform various functionalities. The SDK used in this thesis is the TEXO SDK (version 5.7.4, Ultrasonix Corp.), which allows low-level beamforming both in transmit and receive. Another SDK used in this work is the 'TexoDAQ', which combines the Exam software (i.e. clinical-mode software) and SonixDAQ controller software to provide full control over both the receive- and transmit-sequencing.

2.2.4 Linear Array Transducer

A 128-element linear array transducer (L14-5/38, Ultrasonix Corporation) was used in this research. According to the manufacturer's specifications, the physical footprint of the transducer is 4 mm x 39 mm with an element-pitch and kerf of 0.304 mm and 0.025 mm, respectively. Its operating central frequency is 7.2 MHz with a fractional bandwidth of 70% at -6 dB level. The elevation aperture is 4 mm wide with a fixed focus at 16 mm.

2.2.5 Translational Motion Control Stages

Three high performance linear translational stages (ILS50PP, ILS100PP, and ILS20PP; Newport Corporation) (Fig. 2.4) are assembled to enable accurate and precise linear motion along all three dimensions (x, y, and z direction). A motion controller device (XPS Controller, Newport Corp.) is electronically connected to the stages and was used to control their motion via a remote control (XPS-RC, Newport Corp.) device. The maximum translational speed along each direction is 5 cm/s with a maximum acceleration/deceleration of 20 cm/s² and a displacement resolution of 0.5 μ m detected by an encoder (4000 counts/rev). It is capable of moving a maximum load of 40 N without any changes in its performance. The transducer holder, which is designed to allow

rotations about the vertical axis (z-axis) and one horizontal axis (x-axis) with a resolution of 1° , is attached to the stage and weighs less than the specified maximum limit allowed.

2.3 Flow Phantoms Fabrication

Two different phantoms were used in this study, a straight-tube flow phantom with large internal diameter (ID) and a carotid flow phantom. Fabrication and dimensions of each are described in the following sub-sections. The large ID phantom was used in the ‘multi-receiver study’ and the carotid-flow phantom was used in the ‘aperture-translation study’.

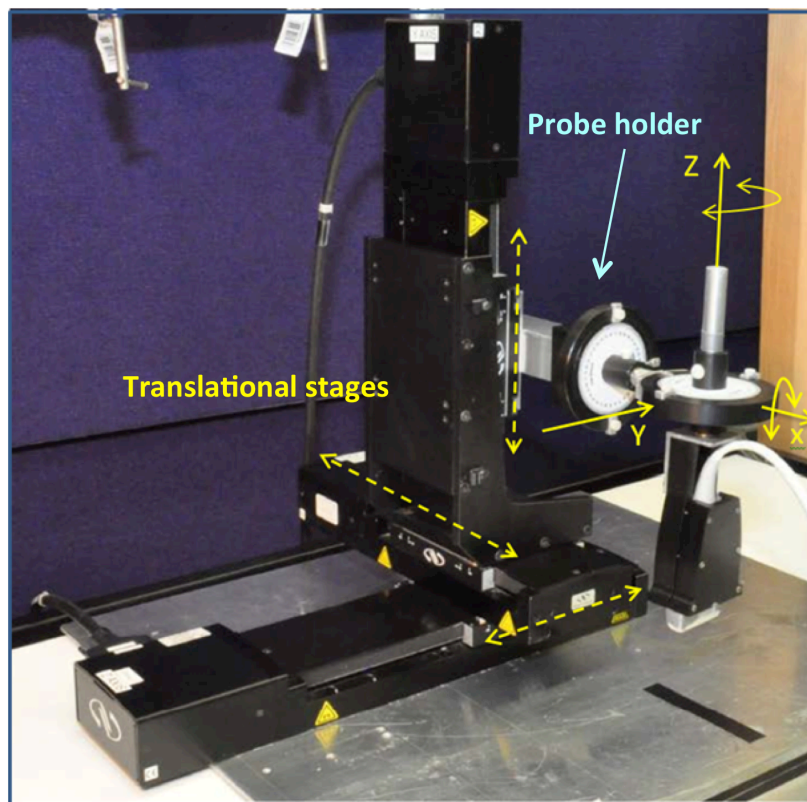


Figure 2.4: Transducer holder attached to the vertical translational stage of the three-axis system. The linear motion along x, y, and z axes (dashed yellow arrows) and rotational motion about the z and x axis of the holder are shown (yellow circled arrows). The yellow arrows represent the direction of motion of the linear stages.

2.3.1 Wall-less Straight-tube Flow Phantom

For the multi-receiver study (presented in Chapter 3), a straight-tube flow phantom (Fig. 2.5) with 2.46-cm ID was fabricated in-house to generate parabolic flow.

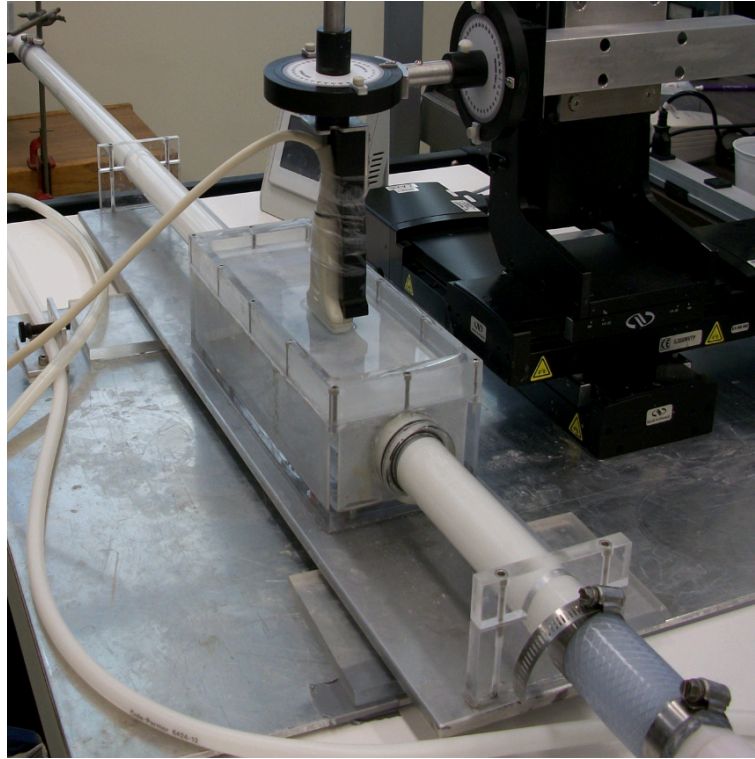


Figure 2.5: Agar-based wall-less straight-vessel phantom with 2.46 cm internal diameter.

The phantom is referred to as a ‘straight large-ID flow phantom’. The acrylic tube, with an inlet length of 1.1 m adjoined to a wall-less flow channel for scanning purposes, was fabricated using an agar-based tissue-mimicking material (TMM) (Ramnarine et al. 2001). The TMM matches the acoustic properties of soft tissue (speed of sound of $1540 \text{ cm}\cdot\text{s}^{-1}$ and attenuation of $0.3 \text{ dB}\cdot\text{cm}^{-1}\cdot\text{MHz}^{-1}$). A coarse-meshed foam collar was wrapped around the inlet and the outlet tubes to reinforce the acrylic-TMM interface and prevent fluid leakage. A thin sheet of the coarse-meshed foam was also attached to the bottom

surface of the phantom to diffuse strong reflections from the base. To protect the TMM from drying, a thin Lexan™ sheet was placed at the top of the phantom.

The flow channel was perfused with a blood-mimicking fluid (BMF) (Ramnarine et al. 1999), modified according to Thorne *et al.* (Thorne et al. 2008), with measured viscosity of 4.10 ± 0.05 cP and a flow rate of 13.3 ± 0.7 mL/s. A centerline velocity of 5.4 ± 0.3 cm/s [Eq. (2.17)] was generated which resulted in ~ 344 Reynolds number. The volumetric flow rate was calculated by measuring the time taken for a fixed volume (275 ml) of the fluid to flow through the outlet and averaged over six measurements. Note that a large diameter vessel was used to generate a range of low velocities (~ 5 cm/s) such as would lie within 2 mm of the walls of a carotid artery during the diastolic phase (Holdsworth et al. 1999) and to specifically obtain a shallow velocity gradient (i.e. narrow velocity range) within any given sample volume. The velocity range obtained was ≤ 0.09 cm/s within each sample volume.

2.3.2 Wall-less Carotid Flow Phantom

A carotid flow phantom (Fig.2.6) with 50% stenosis at the bifurcation (Smith et al. 1996) was also fabricated in-house. While the flow in the bifurcation was used for a study not presented here, only the flow in the common carotid artery (CCA) of this phantom was used as a straight vessel for the aperture-translation study (presented in Chapter 4). The phantom is therefore, referred to as the ‘straight small-ID flow phantom’ in the rest of the thesis. The diameter of the CCA was 8 mm.

The phantom was fabricated using polyvinyl alcohol (PVA) cryogel as a tissue mimicking material (TMM) (Surry et al. 2004). The gel contained 10% PVA solution

with 1% of silicon oxide and 0.3% of potassium sorbate added as a preservative. Silicon oxide was used to introduce speckle and to match the attenuation to that of tissue. The phantom was contained in an acrylic box with dimensions 24 cm x 10 cm x 7.6 cm. Each side was attached using screws and springs [Fig. 2.6(a)–(b)]. This combination was used to allow for PVA expansion during the freeze-thaw-cycle (FTC). In addition, thick sheets of Styrofoam were placed at either end to allow expansion along the length of the phantom. The PVA is usually expected to expand by $\sim 10\%$ in length. As was done for the large-ID vessel a thin sheet of a coarse-meshed foam was attached to the inside of the bottom face of the box [Fig. 2.6(a)–(b)] to diffuse specular reflections that may introduce artifacts and noise to the received signal. To create the wall-less flow channel, a lost-material casting technique (Smith et al. 1999) was used. The technique used a low melting point alloy (cerro-low) to create the metal core, and the PVA solution was poured around it. The heated PVA solution was poured into the assembled phantom box [Fig. 2.6(c)]. The assembly went through three FTCs, where each cycle was a 24-hr freeze at -31°C and a 24-hr thaw at room temperature, to attain an approximately tissue-matching speed of sound of ~ 1540 m/s and attenuation of ~ 0.3 dB/cm/MHz (Zell et al. 2007). The core was then melted out by heating the phantom in a water-bath at a constant temperature of 50°C (King et al. 2011), leaving a hollow channel.

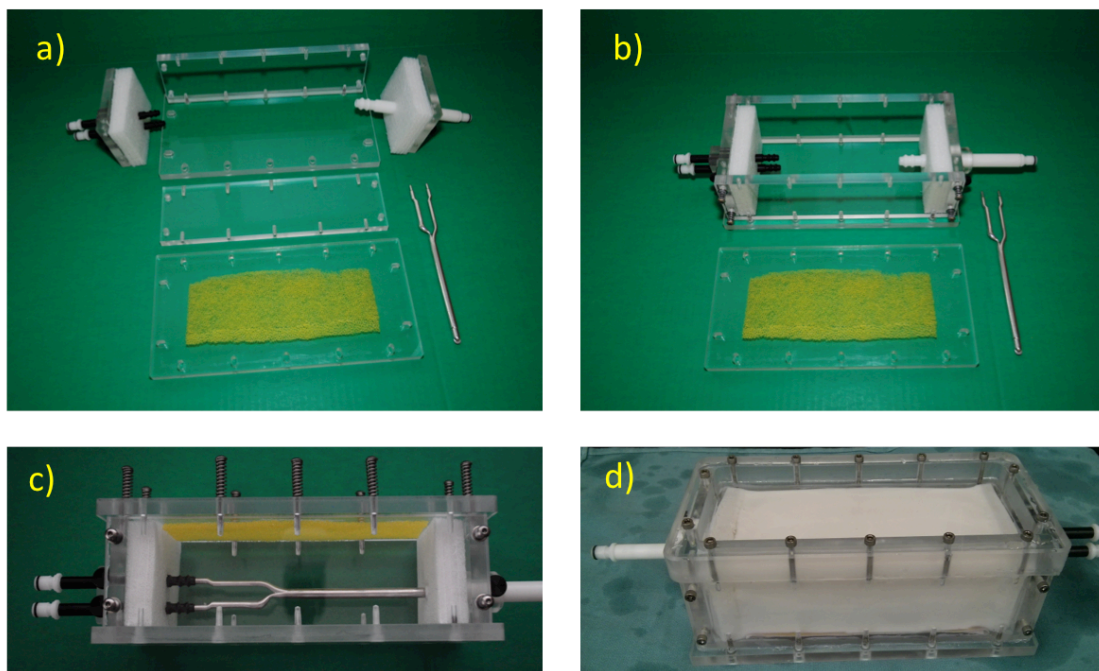


Figure 2.6: Key fabrication steps (a-c) of a CCA flow phantom (d).

The same modified BMF was used to perfuse the CCA vessel channel with a low constant flow rate of ~ 1 ml/s using gravity-fed flow, generating a parabolic centerline velocity of 3.4 ± 0.5 cm/s with Reynolds number of ~ 68 . The B-mode image with its velocity spectrogram is shown in Fig. 2.7.

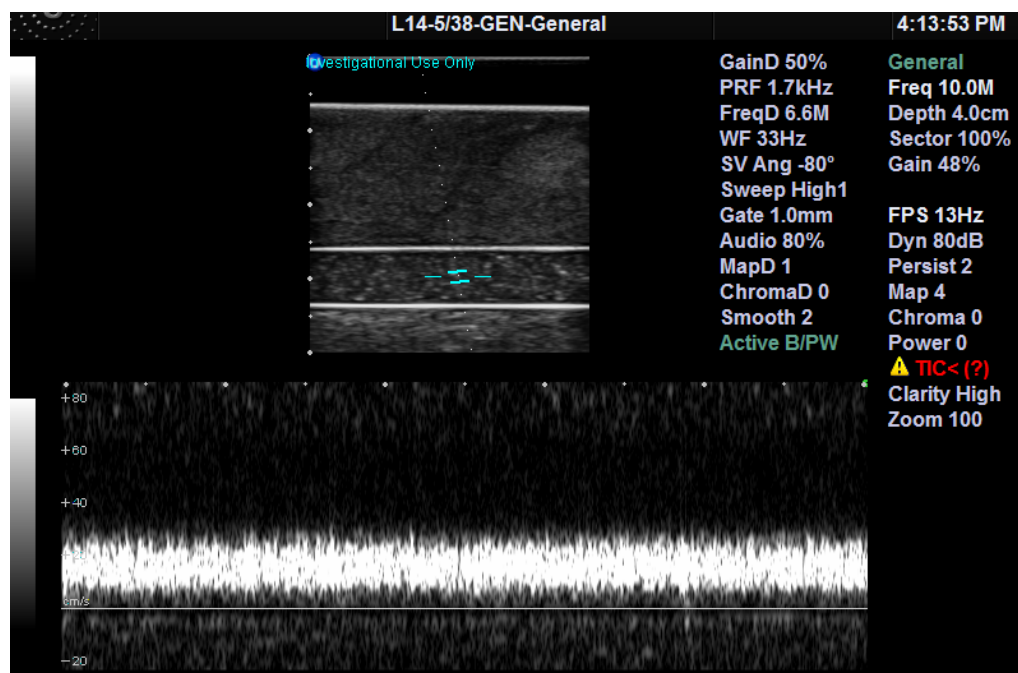


Figure 2.7: Duplex display of the B-mode image and the Doppler spectral mode showing the CCA vessel and the velocity spectrogram from a sample volume placed at the center of the vessel, as indicated by the cursor in the B-mode image.

2.3.3 Gravity-Flow Setup

Fig. 2.8. shows the gravity-fed flow setup, which was used to generate parabolic flow in the straight large-ID and the small-ID vessel. The reservoir system consisted of two reservoirs (Fig. 2.8, bottom). The lower reservoir is used as a pressure head and the top reservoir, used to minimize the amount of air bubbles entering the pressure-head reservoir, collects the fluid from the feedback tank. Air bubbles are highly attenuating and therefore undesired for ultrasound imaging. These last longer than normal in the BMF due to presence of surfactant (Jet-Dry), which is used as a wetting agent for dispersing the ultrasound-scattering (nylon) particles in the fluid.

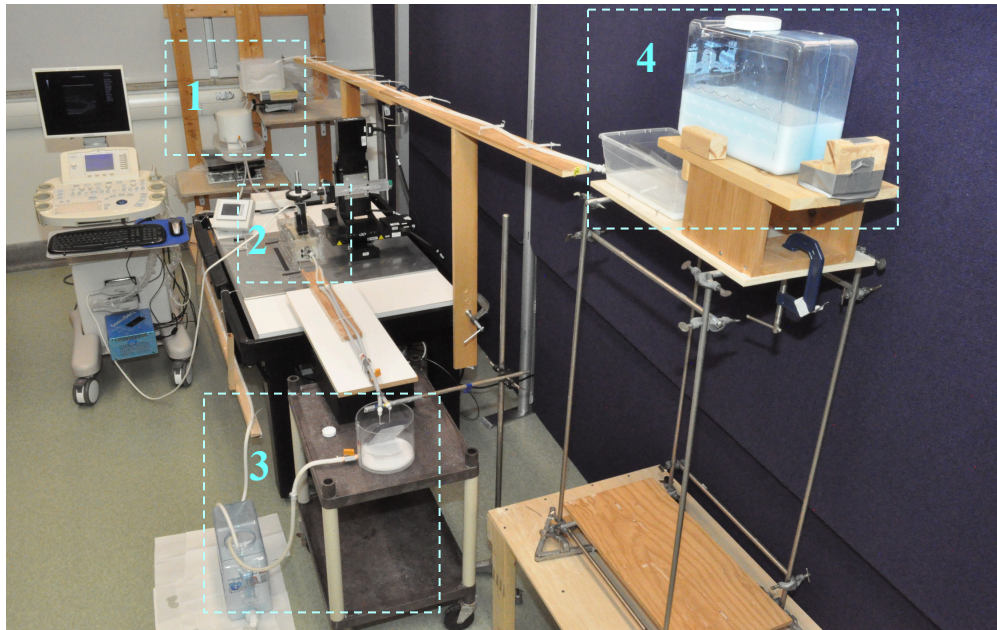
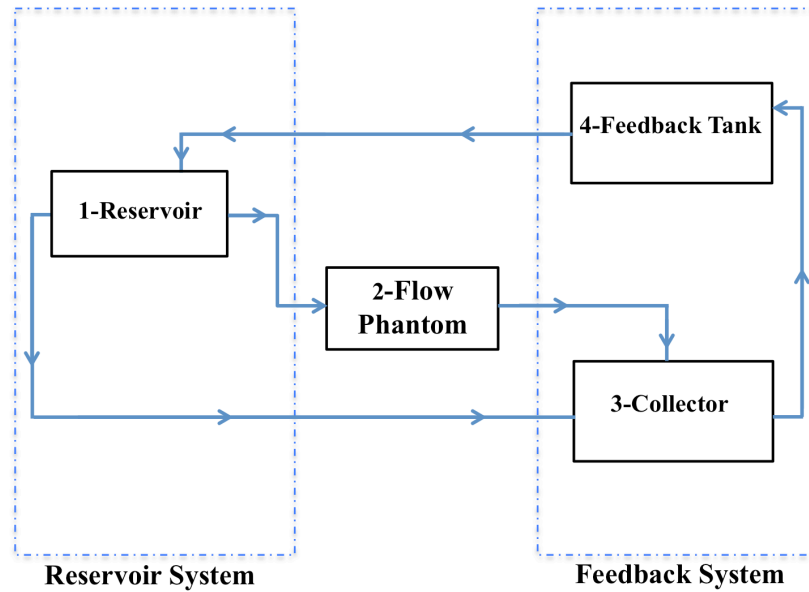


Figure 2.8: Schematic (top) and photo (bottom) of the gravity-fed flow setup. Blood-mimicking fluid in a raised reservoir (1) flows through the phantom (2) at a gravity-driven rate determined by the height of the reservoir and then into the collector tank (3). Fluid is returned to the reservoir via the intermediate feedback tank (4).

The feedback system consists of a collector and a feedback tank (box 3 and 4, respectively). To minimize fluid agitation (causing air bubbles) when fluid flows into a container (e.g. pressure head reservoir or the collector), it first flows onto a flat smooth-surfaced acrylic sheet placed at an angle inside the container. To maintain a constant pressure head, the fluid in the pressure head reservoir is allowed to overflow, which is then collected by the collector (box 3). The height of the pressure head reservoir and the valve at the outlet are adjusted to set the desired constant flow rate through the vessel phantom.

2.4 Data Acquisition and Processing

2.4.1 Crossbeam Multi-Receiver Configurations

The raw data were acquired using the programmable ultrasound system (Sonix RP and SonixDAQ, Ultrasonix Medical Corp., Richmond, B.C. Canada) with the linear array transducer (L14-5/38, Ultrasonix Medical Corp.). Custom data-acquisition code was used to generate a central 32-channel transmit beam focused at the center of the wall-less flow channel (30-mm focal length) using a central transmit frequency of 5 MHz, a pulse length of 5 cycles, and a PRF of 223 Hz. The 12-bit RF signal, with a sampling rate of 40 MHz, was recorded from all 128 channels for offline processing. The imaging parameters are summarized in Table 1. These parameters were based on the capabilities of the sonixDAQ except for the pulse-length and the PRF. The pulse-length of 5 cycles was chosen to strike a balance between the high frequency resolution due to a narrow bandwidth versus high spatial resolution from a broadband pulse. A low PRF of 223 Hz was chosen, as the focus is on estimation of low blood velocities. The sonixRP limited the PRF to 670 Hz, which was then lowered in post-processing to 223 Hz by picking the

data from every third beam. For each acquisition, >1300 pulses of received data were recorded, and the data acquisition was repeated 10 times. A single acquisition from the linear array provided only two receiver beams, i.e. a 2R configuration [Fig. 2.1(a)]. To achieve configurations with 3R and higher, data acquisition was repeated after rotating the linear array around the vertical transmit (z) axis through a suitable azimuthal angle [Fig. 2.1(b)–(d)]. To obtain the 3R and 6R configuration, the transducer was oriented at azimuthal rotations of 0° , 60° and 120° relative to the vessel axis (y-axis), as illustrated in Fig. 2.1(b), to acquire the 0° - and 180° -, 60° - and 240° -, and 120° - and 300° -beams, respectively. Note that ϕ_n in [Eq. (4)] is the azimuthal rotation angle of the n^{th} receiver beam for an NR configuration. For a 3R configuration, only the 0° , 120° , and 240° beams were selected from the three transducer azimuthal rotations mentioned above, whereas all six beams were used to construct the 6R configuration. A similar scenario is shown in Fig. 2.1(c) for 4R and 8R. To achieve the 5R configuration, the transducer was positioned at five unique azimuthal rotation angles of 0° , 72° , 144° , 216° , and 288° relative to the y-axis in the xy-plane [Fig. 2.1(d)]. Additionally, to simulate a range of 3D velocity vectors, the data acquisition was repeated at intermediate azimuthal rotation angles ($\Delta\phi = 0^\circ, 15^\circ, 30^\circ, 45^\circ, \text{ and } 60^\circ$) such that each NR configuration was effectively rotated as a whole assembly.

Table 2.1: Ultrasound Imaging Parameters

Parameters	Transmit (Tx)	Receiver (Rc)
Transmit Frequency (f_0)	5 MHz	---
Pulse length	$5\lambda = 0.15$ cm	---
Number of elements	32	32
Focal length	3 cm	Multi-gated
PRF	223 Hz	---
PRF (E-sweep)	335, 223, 168, 134, 112 Hz	---
Steer angle	0°	$10^\circ, 15^\circ, 20^\circ, 25^\circ$
Steer Angle (E-sweep)	0°	15°
Frame rate	14 fps	14 fps
Sampling rate	40 MHz	40 MHz
Quantization	Bipolar pulse	12-bit

The received raw pre-beamformed data were processed offline (MATLAB) to achieve two 32-channel receiver beams on either side of the central transmit beam. A Hanning-windowed apodization was applied to each receive-aperture. The two beams were focused at a given depth with a specified inter-beam angle relative to the vertical transmit beam. The inter-beam angles were kept constant with increasing depths by sliding the 32-element receiver apertures away from the center in lateral steps to achieve a vertical gate length of 0.1 mm along the depth and a lateral resolution of ~ 1 mm at the focus (-6 dB attenuation) for a focal length of 30 mm, close to the center of the lumen (~ 28.5 mm depth). The constant inter-beam angle was used to allow for a fair comparison of the performance of each configuration as a function of velocity, which varies with depth. Due to the limited size of the array, depths greater than 31 mm were not achievable without reducing the inter-beam angle below 25° . The decrease from 25° to $\sim 19^\circ$ in the inter-beam angle was taken into account when calculating the resultant

velocities for depths greater than 31 mm, which extended to the bottom vessel wall at ~41 mm (i.e. lower-half of the parabolic flow profile). These data were processed to show the complete parabolic profile. Note that unless specified otherwise, all results presented here were from the shallow half of the parabolic flow profile for which the inter-beam angle was kept constant. This was also done to separate the effect of attenuation on the performance of our results, as each beam effectively extends through the same thickness of TMM. Estimations from the deeper half of parabola would have lower SNR due to greater difference in the depths, which would not justify combining the results from the upper and lower halves of the parabola.

2.4.1.1 Beam-Selection Methods

Three examples of beam-selection methods – power threshold (PT), minimum Doppler standard deviation (MDSD), and weighted least squares (WLS) – were compared to assess their ability to selectively eliminate or minimize the influence of beams with noisy or low-power Doppler signal. Remaining or appropriately weighted velocity estimates from individual receivers were combined to obtain the resultant velocity estimation from an NR configuration. To assess the validity of the signal from each beam the PT method applied a user-defined minimum power threshold of 40% above the average tissue-signal power for the data set. This user-defined percentage was chosen by plotting velocity residuals (i.e. difference between theory and experiment) for the entire velocity profile over a range of power thresholds for each configuration. A value close to the common minima was chosen. Any beam whose signal power was below this threshold was ignored, and the remaining Doppler shifts (if any) were used to calculate the resultant velocity vector estimate. The MDSD method selected the three beams with signals

showing the lowest standard deviation calculated from 10 independent Doppler shift measurements in order to calculate the resultant 3D velocity vector, whereas the WLS method used information from all N beams but weighted them according to their variance. No arbitrary user-defined criterion was needed for these latter two methods. Also, for comparison, a no-threshold (NT) method used Doppler shifts from all N beams in each configuration to obtain the resultant velocity vector estimate without any selection criterion and was used as a reference method.

2.4.2 Vector Doppler Ultrasound Aperture-Translation

To demonstrate the proof of concept of a new method – aperture translation – to improve the accuracy of low 2D velocities that lie close and within the effective wall-filter cutoff, simple Poiseuille flow was established in the straight small-ID flow phantom. Two versions consisting of a mechanical and an electronic version were tested and compared.

2.4.2.1 Mechanical Sweep

The raw data for the M-sweep method were acquired using the same gravity-flow setup as was used in the multi-receiver-experiment, described in section 2.3.1, but in the straight small-ID flow phantom, with the same acquisition code and the imaging parameters summarized in Table 2.1. The pre-beamformed data were also received simultaneously from all 128 channels using the SonixDAQ, which were beamformed to obtain signals from two 32-element receivers on either side of the transmit-beam. To increase the phase-shift for the blood mimicking scatterers the transducer was translated opposite to their velocities (Fig. 2.2) acquiring data while the transducer was moving. This caused the data from each pulse to be obtained from a slightly different location laterally, i.e. along the direction of the transducer motion. The amount of this lateral

displacement would depend on the PRF, the sweep speed of the aperture (V_s), and the ensemble size used to obtain the mean Doppler shift. Data for a range of sweep speeds from 0 to 5 cm/s were acquired where 0 cm/s is the conventional method. The data were processed at different ensemble sizes (4 – 16) at a PRF of 223 Hz. Ten independent measurements were made at each sweep speed and for each acquisition, >800 pulses of the received-data were recorded. The start of data acquisition and the start of the transducer motion were done at approximately the same time by simultaneously hitting the start keys on both the SonixRP and the XPS-RC. This helped in estimating an approximate number of pulses to be discarded, which would potentially be affected by the acceleration/deceleration of the translational stage. A maximum allowed acceleration of 20 cm/s^2 was chosen for each sweep speed of the translational stage to attain the desired constant speed with the least possible displacement. The total distance spanned by the transducer was adjusted to collect at least one second of data. The acceleration time for the stage to reach a constant maximum speed of 5 cm/s is 250 ms (specification given by Newport Corp.). The maximum number of frames acquired during these times at a PRF of 670 Hz (minimum PRF allowed by the scanner) were ~ 168 , which were not included in the analysis.

The 2D-velocity reconstruction from the Doppler signal was performed in the same manner as was done for the multi-receiver experiment for the 2R configuration [Eq. (2.13)]. A constant power threshold of $\sim 8.4 \text{ dB}$ was applied to all the data irrespective of the sweep speed before re-constructing the resultant 2D velocity. This constant user-defined value was set at 40% above the average tissue Doppler power ($\sim 6 \text{ dB}$), which was chosen by comparing the Doppler signal power from within the lumen and the tissue

background of the phantom. This was applied to remove the low SNR Doppler signal from the stationary tissue. The average velocity and the standard deviation were calculated from the 10 independent velocity estimations and at seven different locations in the vessel. To obtain the true estimated velocity of the moving scatterers the sweep speed was subtracted from the measured estimated velocity of the scatterers. Relative error and SD in the velocity estimations were calculated using Eq. (2.19) and Eq. (2.20).

2.4.2.2 Electronic Sweep

The E-sweep method simulates the effect of the M-sweep method. In this electronic version of the method, a phase difference was introduced between pulses sent from two adjacent transmit-center locations, as shown in Fig. 2.2(b) and described in section 1.1.4.

The acquisition code was modified to electronically sweep the transmit-beam center along the length of the linear array transducer, commonly done for a B-mode swept-scan. The transmit sequences were set to send a fixed number of pulses (2 – 6) before the aperture moved to the next element, with each element corresponding to a vertical line of dots in Fig. 2.9. This was done to achieve different sweep speeds. For example, when the number of pulses from a given transmit-center was set to two at a maximum PRF_{max} of 670 Hz, the sweep speed attained was ~ 10 cm/s for a displacement of 0.3 mm (element-pitch of the transducer). Therefore, the range of sweep velocities achieved, for 2 to 6 pulses sent from each transmit-center, ranged from 10 cm/s to 3.4 cm/s, respectively. To achieve the desired sweep speed, before signal processing, the data were downsampled as shown in Fig. 2.9 (picking the red dots) so that the correct number of pulses are skipped each time. The acquisition was repeated 10 times for each number

of pulses per transmit-center. The ultrasound imaging parameters used are shown in Table.2.1 with changed parameters for the method labeled as ‘E-sweep’.

The data were signal processed in a similar manner as was done in the multi-receiver experiment except the Doppler shift was calculated taking the ensemble size along the lateral direction, shown in Fig. 2.4, instead of in the axial direction (conventional). The velocity reconstruction was done in a similar manner as was done for the M-sweep to estimate the 2D velocity using the signal from the two receive-beams on either side of the transmit-aperture. The average velocities were calculated from the 10 independent measures at five different locations. A comparison was made with the velocities estimated from the M-sweep method and the conventional method. The bias and relative error were calculated using Eq. (2.18) and Eq. (2.19) from the theoretical flow velocities to assess the accuracy of the method. For reliability and precision of the estimates the standard deviation and standard error were calculated using Eq. (2.20) and Eq. (2.21).

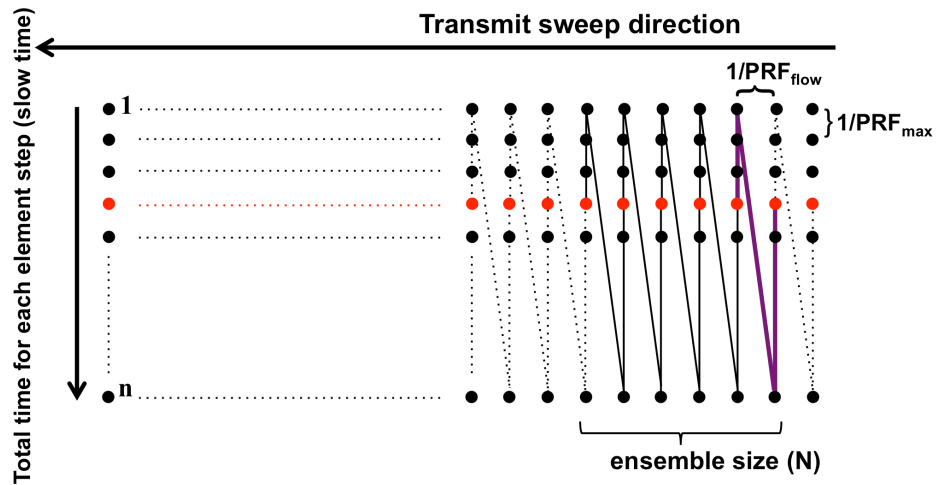


Figure 2.9: Schematic representing the principle of the E-sweep method. One scan-line is obtained from an ensemble of N taken along the transmit sweep direction with a sliding step of two elements. The red dots represent one subset of data chosen for velocity estimations. The slow time ($1/PRF_{flow}$) sampling is equal to the maximum PRF (PRF_{max}) divided by the total number of pulses (n) sent from one transmit center. The purple line shows the number of pulses skipped (slow time period) to process only the pulses shown in red.

Chapter 3

3 Crossbeam Multi-Receiver Configurations

This chapter presents the results and discussion of investigating the potential of various multi-receiver configurations for improved low 3D velocity estimations that lie close to and below the WF_{eff} , defined in Chapter 1, including testing of a suitable beam-selection criterion. Section 3.1 discusses the wall filter used in this study and justification of choosing the WF_{eff} cut-off. Section 3.2 presents the theoretical analysis of various multi-receiver configurations in terms of minimum inter-beam angle and exceeding the wall-filter cut-off for all velocity orientations in 3D-space. Section 3.3 presents the experimental results and section 3.4 discusses the results.

3.1 Effective Wall Filter

Fig. 3.1 shows the frequency response of the equiripple (equal ripples in stopband and passband) minimum phase FIR wall filter, which was used to remove any clutter signal (e.g. sidelobe reverberations) originating from the tissue. Fig. 3.1(a) shows the frequency magnitude response curve of the filter, where the vertical dashed-line indicates the effective wall-filter (WF_{eff}) cut-off of 10 Hz corresponding to a signal magnitude suppression of -20 dB. The -20 dB filter suppression was chosen as the acceptable WF_{eff} suppression by examining our pilot data (Fig. 3.2, A-1.1). It was observed that the Doppler signal showed dramatically high variance ($\sim 100\%$ or higher) when Doppler shift was below 10 Hz. Hence, 10 Hz was chosen as the WF_{eff} . Note that the WF_{eff} is dependent on the choice of the filter parameters. Fig. 3.1(b) represents the phase of the filter's frequency response. The equiripple minimum phase response FIR filter is chosen

for the study over, for example, an infinite impulse response filter, because it is easier to achieve a linear phase response using FIR filter, which is desirable in this study.

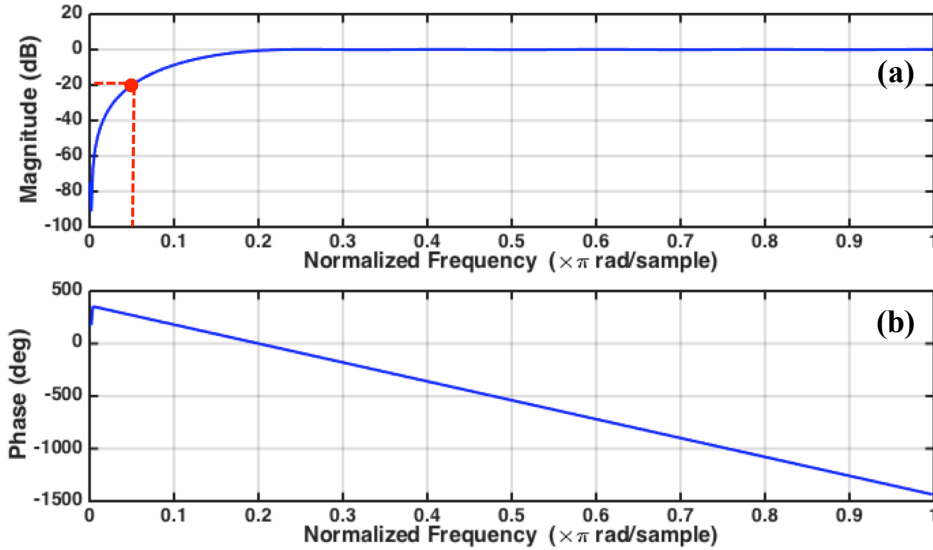


Figure 3.1: Frequency response of the equiripple minimum-phase FIR filter of order 21 and 60-dB suppression. The effective wall filter cut-off is indicated by the vertical dashed line corresponding to a normalized frequency of 0.05.

Justification of the choice of WF_{eff} is presented in Fig. 3.2. It is a plot of the theoretical and experimentally obtained mean Doppler shifts from each of three receiver beams of a 3R configuration, sampling a velocity magnitude of 2 cm/s located at ~ 2 mm depth below the top vessel wall and with each experimental value averaged over 160 independent measurements. The receiver beams were oriented at various azimuthal angles with the transmit beam maintaining an elevation angle of 90° . The gray band represents the 10-Hz WF_{eff} cutoff region. Theoretically calculated Doppler shifts for the third beam (beam3) generally lie close to or within the 10-Hz cutoff, thus the experimental mean Doppler shifts for this beam have higher standard deviations for nearly all orientations, ranging from 10 Hz to 18 Hz (i.e., $\geq 96\%$), reflecting the effect of

the 10-Hz WF_{eff} . For Doppler shifts > 10 Hz the standard deviation is usually < 7 Hz (i.e. $< 40\%$). Similar results were observed for other inter-beam angles ($\beta = 15^\circ$ and 25°) and are shown in appendix (Fig. A-1). For context, although velocities of magnitude ≤ 5 cm/s used in our study encompass the whole vessel with diameter of 2.46 cm (i.e. farther away from the wall), this range of velocities would lie within 0.7 mm ($< 5\lambda$) from the wall of an 8-mm diameter carotid artery with average diastolic flow rate of ~ 4 ml/s [(Holdsworth et al. 1999), Fig. 11] and centerline diastolic velocity of ~ 16 cm/s.

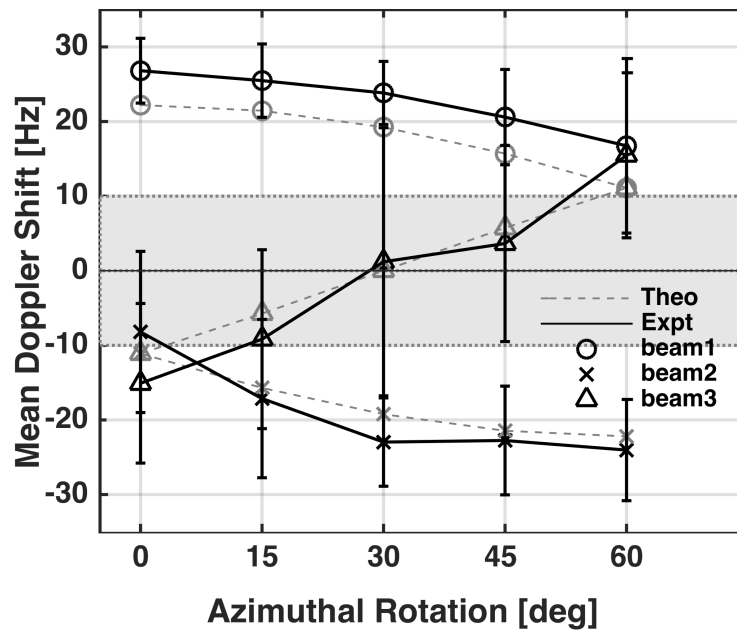


Figure 3.2: Experimental mean Doppler shifts (solid) averaged over 160 independent measurements of a velocity of 2 cm/s with a 3R configuration with an inter-beam angle of 20° . The corresponding theoretical Doppler shifts are shown with gray markers. The gray band represents the effective wall-filter cut-off range ($\pm WF_{\text{eff}}$). Error bars represent standard deviations over 160 independent measurements.

3.2 Theoretical Geometric Analysis

Fig. 3.3 presents results from a geometric analysis of the number of valid velocity-component estimates expected for a velocity magnitude of 2 cm/s using 3R to 8R configurations.

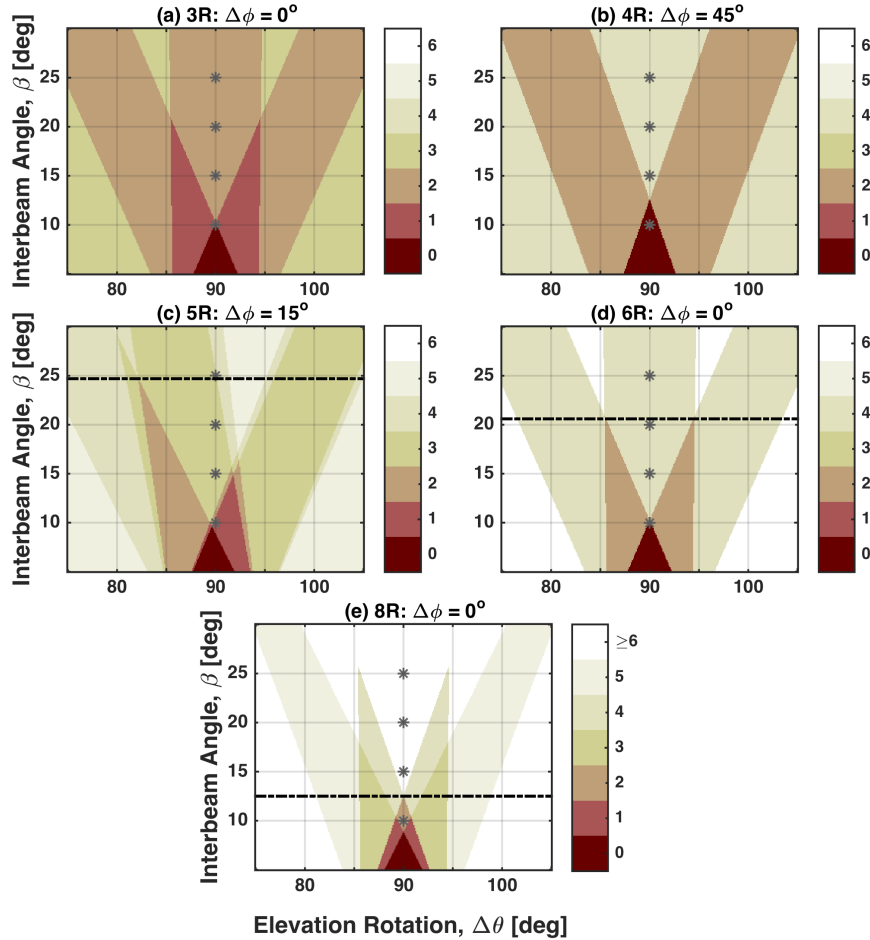


Figure 3.3: Color-encoded plots demonstrating theoretical determination of the number of receivers with Doppler shifts exceeding a WF_{eff} of 10 Hz for each of the 3R to 8R configurations (as labeled) for inter-beam angles varying from $\beta = 5^\circ$ to 30° . Each is shown for a 2 cm/s velocity vector rotated through elevation angles $\Delta\theta$ between 75° to 105° relative to the x axis and for the worst-case of azimuthal angles, $\Delta\phi$. The data points labeled with an asterisk correspond to parameters applied in the experiments and the worst-case $\Delta\phi$ (one column per configuration) included in Fig. 3.4. The black dashed-line represents the minimum inter-beam angle for which ≥ 3 receivers' Doppler shifts are above the WF_{eff} .

Each of these is shown for a range of inter-beam angles ($5^\circ \leq \beta \leq 25^\circ$), a critical range of elevation angles ($75^\circ \leq \theta \leq 105^\circ$), and the worst-case of azimuthal angle $\Delta\phi$ (0° for 3R, 6R, and 8R, 15° for 5R, and 45° for 4R configurations). The critical range of elevation angles refers to the range for which the number of receivers with Doppler shifts exceeding WF_{eff} is impacted by the inter-beam angle and azimuthal orientation. The worst-case of $\Delta\phi$ is the azimuthal orientation for which the region with ≥ 3 -receivers' Doppler shifts exceeding WF_{eff} is minimum compared to other $\Delta\phi$ s for each configuration. The results show that with $\geq 5R$, a minimum inter-beam angle exists above which Doppler shifts always exceed the WF_{eff} for at least 3 receivers across the entire range of elevation angles. For 5R and 6R, this minimum inter-beam angle is $\sim 25^\circ$ and $\sim 21^\circ$ respectively, and $\sim 13^\circ$ for the 8R configuration [(Fig. 3.3(c), (d), and (e))]. No such minimum inter-beam angle exists for 3R and 4R [Fig. 3.3(a) and (b)].

This is further demonstrated in Fig. 3.4 specifically for an elevation angle $\theta = 90^\circ$, as indicated by asterisks in Fig. 3.3; each is shown for four inter-beam angles ($\beta = 10^\circ, 15^\circ, 20^\circ, 25^\circ$) and five velocity vector azimuthal angles in the range $90^\circ \leq \phi'_n \leq 150^\circ$ corresponding to azimuthal rotations of $0^\circ \leq \Delta\phi \leq 60^\circ$ of each configuration relative to the flow-direction vector. Beyond this range of azimuthal rotations the relative azimuthal orientations are repeated; e.g. for the 6R configuration, the velocity vector orientation relative to six equally spaced receivers is the same at $\Delta\phi = 0^\circ$ as for $\Delta\phi = 60^\circ$. The numbers of receivers whose Doppler shifts exceed the WF_{eff} for each configuration are color-encoded. The azimuthal rotations presented span the entire range of unique azimuthal orientations for all configurations; beyond this the relative azimuthal

orientations are repeated, e.g. for the 6R configuration, the velocity vector orientation relative to six equally spaced receivers is the same at $\Delta\phi = 0^\circ$ as for $\Delta\phi = 60^\circ$.

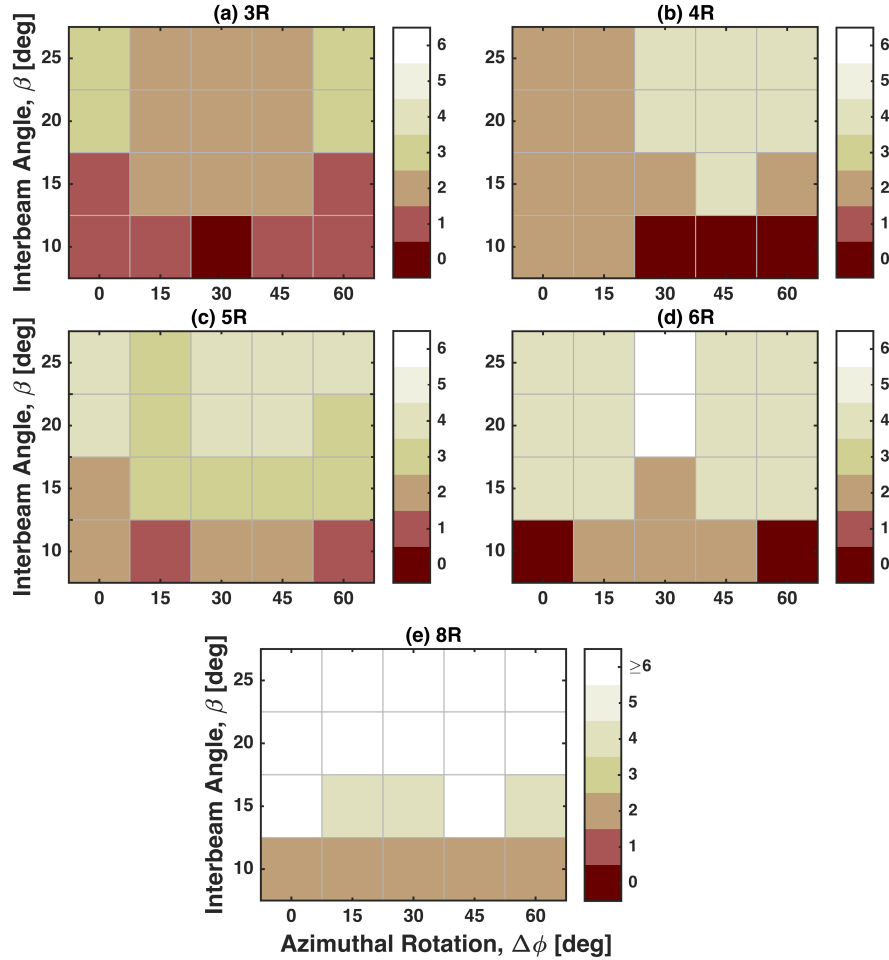


Figure 3.4: Color-encoded plots demonstrating theoretical determination of the number of receivers with Doppler shifts exceeding the effective wall filter cutoff of 10 Hz for 3R - 8R configurations (as labeled) each shown for $\beta = 10^\circ, 15^\circ, 20^\circ,$ and 25° for a 2 cm/s velocity vector rotated through azimuthal angles of $\Delta\phi = 0^\circ, 15^\circ, 30^\circ, 45^\circ,$ and 60° relative to y axis with an elevation angle $\theta = 90^\circ$.

Ideally, an accurate assessment of a 3D velocity vector requires accurate estimations of the Doppler shifts from at least three beams oriented in 3D space. The performance of each configuration was assessed in terms of a possible minimum inter-beam angle ($10^\circ \leq \beta \leq 25^\circ$) for which at least three or more beams exceed the WF_{eff} for all relative velocity

orientations. No such inter-beam angle $\leq 25^\circ$ exists for 3R and 4R configurations [Fig. 3.4(a) and (b)], whereas this was achievable with $\beta \geq 20^\circ$ for 5R [Fig. 3.4(c)] and 6R [Fig. 3.4(d)] configurations, and $\beta \geq 15^\circ$ for the 8R [Fig. 3.4(e)] configuration, each shown by a black dashed line.

3.3 Experimental Results

3.3.1 Doppler Power and Velocity Components

Figure 3.5 and Fig. 3.6 show the averaged Doppler powers and estimated velocity components, respectively, with their corresponding standard deviations calculated from 160 independent measurements for receiver-beams oriented at various azimuthal angles, which would contribute in calculating the resultant velocity vector oriented along the +y axis i.e. $\Delta\phi = 0^\circ$, $\theta = 90^\circ$ to achieve 3R-8R configurations for the selected inter-beam angle of $\beta = 20^\circ$. For example, a 5R configuration oriented at $\Delta\phi = 0^\circ$ would require velocity-components from receiver-beams oriented at 0° , 72° , 144° , 216° , and 288° . As expected the Doppler power is lower for larger Doppler angles reducing the SNR [Fig. 3.5(d)], the effect of which is observed in the reliability of velocity estimations [Fig. 3.6(d)] showing higher standard deviations. One or more of these low-SNR velocity-components contributing in the estimation of the resultant velocity will reduce the accuracy and precision of the resultant velocity estimates. The PT beam-selection method mentioned in Chapter 2, applies a Doppler power threshold, which is indicated by the dotted lines in Fig. 3.5, to each beam's Doppler signal in order to eliminate the low SNR beams' signal before calculating the resultant velocity. The resultant mean velocity magnitude and direction are calculated from the respective velocity-components shown in Fig. 3.6, to obtain the estimations from 3R–8R configurations using the PT method.

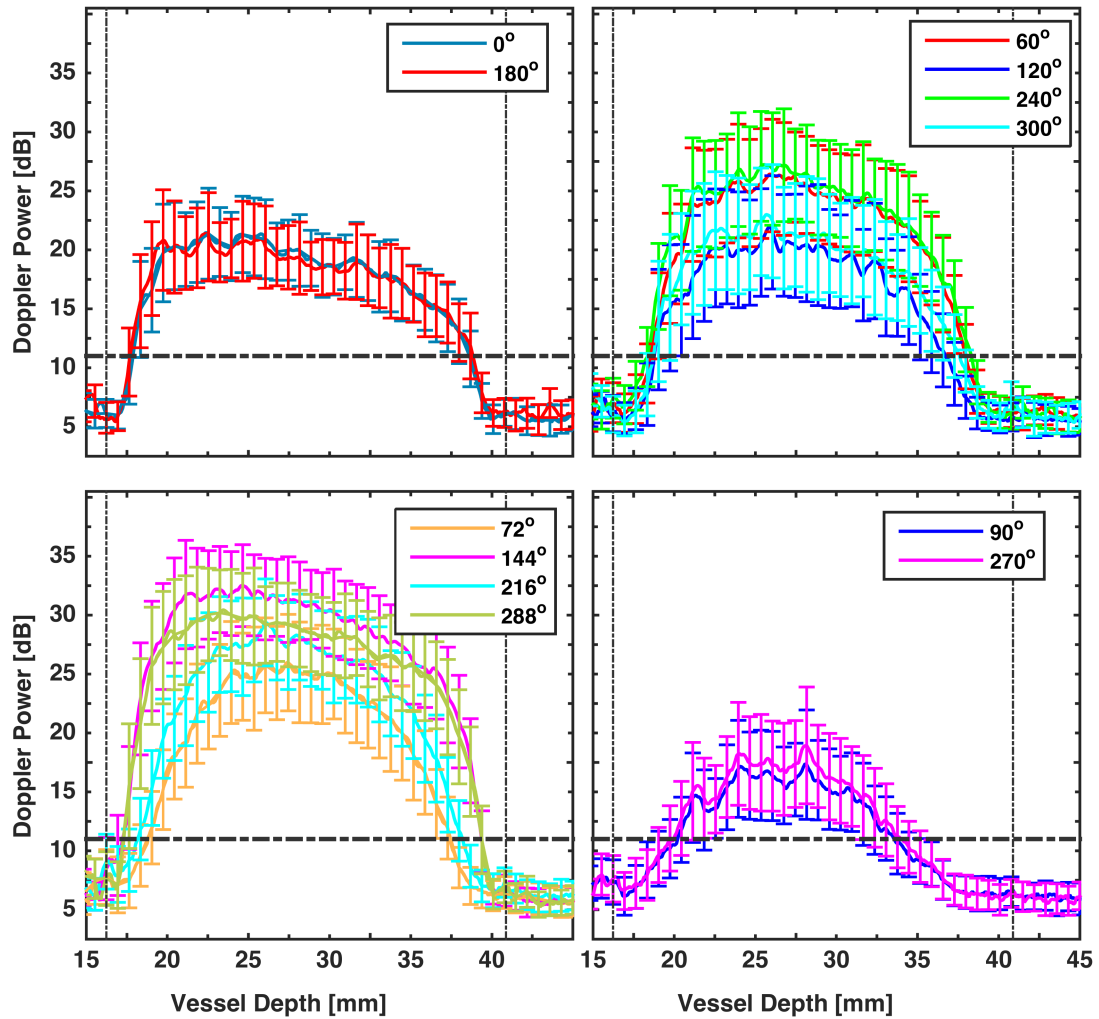


Figure 3.5: Mean Doppler power from each receiver beam oriented at various azimuthal rotation angles (legend labels), averaged over 160 independent measurements, to achieve 3R to 8R configurations, with $\beta = 20^\circ$, for velocity vectors oriented at an azimuthal angle of 90° (i.e. azimuthal rotation, $\Delta\phi = 0^\circ$ relative to y axis) and elevation angle $\theta = 90^\circ$, for a parabolic flow data. The beam-selection method used is the PT method, indicating the Doppler power chosen as shown by the black dashed lines in each sub-plot. The legend labels represent the azimuthal rotations of the receiver beams with respect to the velocity vector. The error bars represent SDs. Vertical dashed-lines separate the lumen and TMM regions.

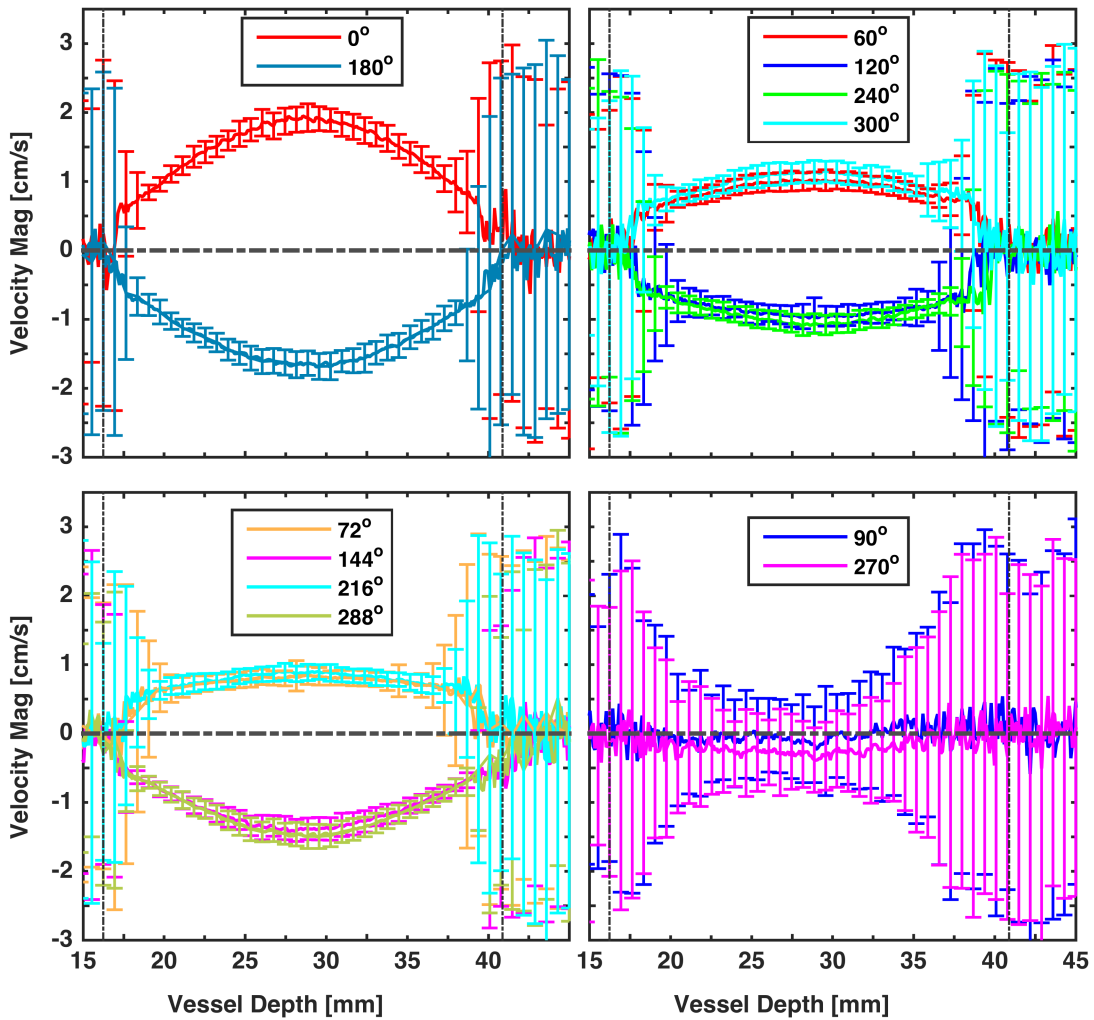


Figure 3.6: Mean Doppler velocities from each receiver beam oriented at various azimuthal rotation angles each with an elevation angle of 20° , averaged over 160 independent measurements, to achieve 3R to 8R configurations, with $\beta = 20^\circ$, for velocity vectors oriented at an azimuthal angle of 90° (i.e. azimuthal rotation, $\Delta\phi = 0^\circ$ relative to y axis) and elevation angle $\theta = 90^\circ$, for parabolic flow. The legend labels represent the azimuthal rotations of the receiver beams relative to the velocity vector (i.e. vessel axis). For example, a 3R configuration would be reconstructed from beams at 0° , 120° , and 240° ; this could be extended to 6R by including beams at 60° , 180° , and 300° . The error bars represent SD. Vertical dashed lines separate the lumen and TMM regions.

These estimates are presented in Fig. 3.7(a)–(c). The estimated resultant-velocities (Fig. 3.7) were aligned with the theoretical profile by locating the position of the shallower vessel-wall, which was done by matching the measured depth with that obtained from the

Doppler power plot. For all configurations, the estimated velocity magnitudes agree with the theoretical parabolic profile of Poiseuille's Law to within 15% for velocities as low as 3 cm/s, which also held true for all azimuthal rotations $\Delta\phi = 0^\circ$ to 60° with remaining estimated resultant-velocities for $\Delta\phi \geq 15^\circ$ shown in Fig. A-2.

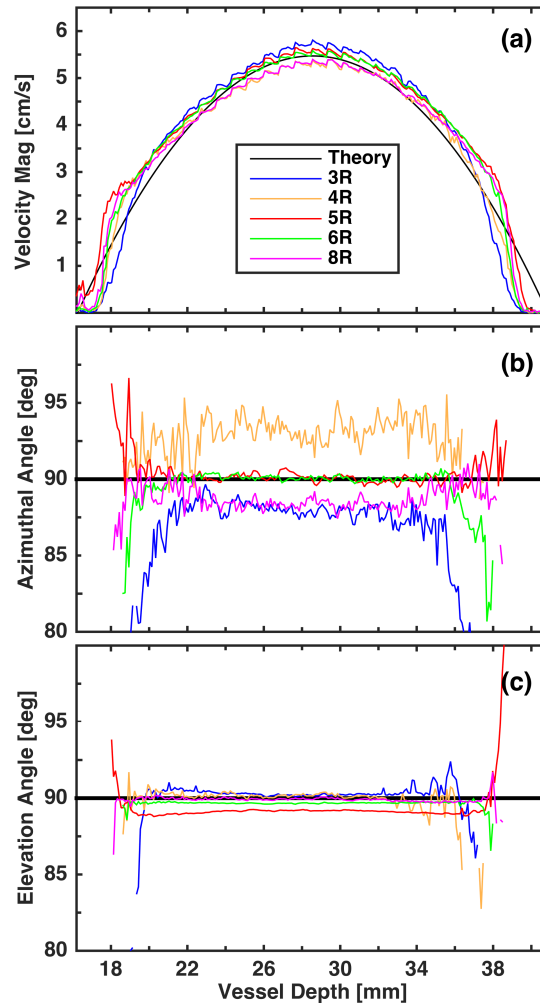


Figure 3.7: Sample parabolic flow data representing mean Doppler velocity vector estimations for (a) magnitude, (b) azimuthal direction, and (c) elevation direction, averaged over 160 independent measurements for each of 3R to 8R configurations, with $\beta = 20^\circ$, for velocity vectors oriented at an azimuthal angle of 90° (i.e. azimuthal rotation, $\Delta\phi = 0^\circ$ relative to y axis) and elevation angle $\theta = 90^\circ$, after applying the PT method. Theoretical velocity magnitude profile and direction are shown in solid black line. Note that velocity estimations from only the upper half of the profile were used for the analysis.

For velocities ≥ 3 cm/s, the velocity azimuthal angle error was within 5° for $\geq 5R$ configurations for all rotations, but varied up to $\pm 10^\circ$ for 3R and $\pm 15^\circ$ (at $\Delta\phi = 15^\circ$) for 4R. The error in the elevation angle of the estimated velocity was within $\pm 2^\circ$ for all configurations for velocities ≥ 2 cm/s. This is also true for all three beam-selection methods therefore the results for the elevation angle are not shown in the subsequent figures. Note, for the PT method, a small fraction ($\leq 5\%$) of the angle estimations were undefined at lower velocities, i.e. signal power from every receiver in the configuration was below the selected power threshold, and thus all were considered invalid. These values were not included when calculating the average error presented here, or in the remaining results that follow.

3.3.2 Relative Performance of Multi-Receiver Configurations for Velocity Estimations

Fig. 3.8 presents a comparison of beam-selection methods (PT, MDSD, WLS) and the reference NT method for selecting the best receiver beams in terms of their SNR to estimate a velocity vector with a magnitude of 2 cm/s. The velocity magnitude and the direction bias are plotted for five different configurations, each for an elevation angle of 90° and inter-beam angles of 15° , 20° , and 25° . Each data point represents the bias in velocity, averaged over 160 independent repeated measurements for each of the five azimuthal rotations ($\Delta\phi$), giving a total of 800 measurements. Note that the velocity bias for each rotation may be either positive or negative. As mentioned in the methods, Chapter 2, we applied an azimuthal rotation, $\Delta\phi$, to the entire configuration to emulate various relative vector orientations in a 2D (xy) plane perpendicular to the transmit (z) axis (i.e. vertical axis in Fig. 2.1). For any given elevation angle (i.e. along a given

vertical line in Fig. 3.3) within the critical range, the number of receivers with a Doppler shift exceeding WF_{eff} changes with the azimuthal orientation of the velocity vector relative to the configuration, as demonstrated in Fig. 3.4. It is observed from Fig. 3.3 that there is no one case of elevation angle for which the number of receivers with Doppler shifts exceeding the WF_{eff} is the same for all azimuthal rotations for each configuration. Hence, choosing one elevation angle is a representative example of the system's performance compared to any other elevation angle within the critical range. An elevation angle of $\theta = 90^\circ$ was chosen here due to ease of the set-up.

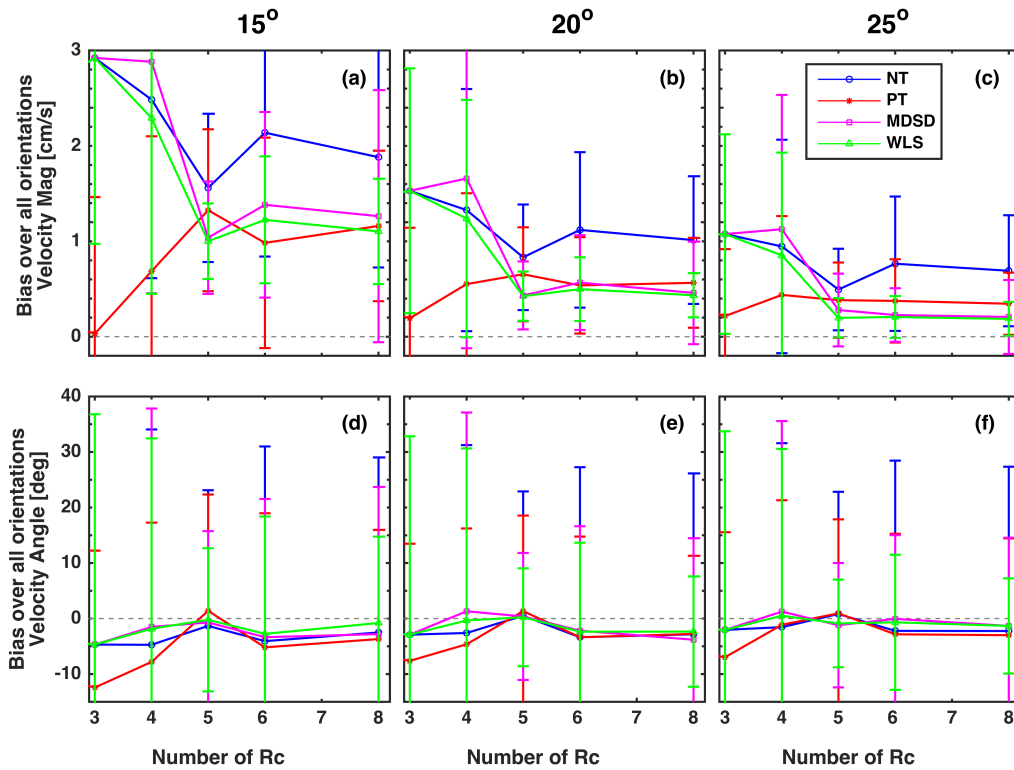


Figure 3.8: Bias in velocity magnitude (a – c) and direction bias (d – f) averaged over all orientations comparing beam-selection methods for 3R - 8R configurations and $\beta = 15^\circ$ (a, d), 20° (b, e) and 25° (c, f) when measured a theoretical velocity vector of 2 cm/s. Biases represent the averaged differences between the experimental and theoretical values over all five azimuthal orientations ($\Delta\phi = 0^\circ, 15^\circ, 30^\circ, 45^\circ, 60^\circ$ relative to y axis). Error bars represent SDs over 800 measurements.

3.3.2.1 Velocity Estimations Improve with Increasing Inter-beam Angle

As expected, an overall improvement, both in terms of reduced bias and standard deviation, is seen in the velocity vector magnitude and direction estimation with increasing the inter-beam angle for all configurations and for all methods. This improvement is greater when the inter-beam angle is increased from $\beta = 15^\circ$ to 20° . In the case of the PT method, increasing β from 15° to 20° for 5R [Fig. 3.8(a), (b)], substantially reduced the error and uncertainty in the velocity magnitude from $66\% \pm 43\%$ to $33\% \pm 26\%$ with a further drop to $19\% \pm 20\%$ when β increased to 25° . Average direction bias stayed within 15° overall, but it was within 5° with $\geq 5R$ and $\beta \geq 20^\circ$, with small improvement of $\leq 4^\circ$ in the standard deviation when β increased from 15° to 20° . Similarly, results from the theoretical geometric analysis suggested that $\geq 5R$ and a minimum of $\beta = 20^\circ$ would be needed in order to obtain at least three beams with Doppler shifts exceeding WF_{eff} for all azimuthal directions, as necessary to obtain accurate 3D velocity vector estimations. Hence, experimental results here agree with the findings of the geometric analysis.

3.3.2.2 Beam-Selection Methods Perform Equally Well for $\geq 5R$ at Low Velocities

For all β , both the velocity magnitude and direction biases [Fig. 3.8(a)–(f)] decreased as the number of receiver beams increased. When using a 5R configuration to measure a velocity vector of 2 cm/s, overall the velocity magnitude bias was lowest for both the MDSD and WLS methods (0.43 cm/s; $\sim 22\%$), with WLS showing the least standard deviation (0.26 cm/s or 13%), shown in Fig. 3.8(b). For $\geq 5R$ and $\beta \geq 20^\circ$ [Fig. 6(b), (c), (e), and (f)], all three selection methods, excluding the NT method, led to a bias of 0.65

cm/s ($\sim 33\%$) and 5° at worst. Note that the NT method is used as a reference therefore, results for this method are not included in the quantitative comparison unless stated otherwise. For 3R, the WLS and MDSD methods used all three beams and were therefore identical to the NT method. Differential weighting was not applicable on a fully determined system (3R) and only played a role in an over-determined system ($\geq 4R$). The PT method consistently improved estimates compared to the NT method for most of the configurations. The WLS method showed reduced variability compared to all other selection methods for all configurations, especially when $\geq 5R$. However, for 4R, the WLS and the MDSD methods gave large velocity magnitude bias, while the PT method showed lower magnitude bias but with higher direction bias, especially for $\beta = 15^\circ$. With the PT method, the selection of valid Doppler shifts from amongst low SNR beams reduces the bias in magnitude but increases it for the direction estimation when the number of included receiver signals is reduced to less than three. As mentioned previously, the PT method can have reduced precision in some cases because it eliminates Doppler shifts from all of the receivers for a subset of the data, e.g. $\sim 1\%$ of all the estimates at a velocity of 2 cm/s for 4R in this case. Overall, with $\geq 5R$, performance became relatively insensitive to the selection method.

3.3.2.3 Velocity Orientation Sensitivity Reduced for $\geq 5R$

Fig. 3.9 provides insight into the results from Fig. 3.8 (where bias was averaged over all orientations) by showing the velocity vector biases as a function of the individual azimuthal rotations representing the different relative velocity vector orientations. Results are shown for configurations with $\geq 4R$ and $\beta = 20^\circ$. For 4R [Fig. 3.9(a) and (d)], a greater velocity magnitude bias with higher variability is observed, especially at $\Delta\phi = 0^\circ$

and 15° with the MDSD method, which explicitly includes a third beam's Doppler shift regardless of SNR, thus reducing the reliability and accuracy. Bias and variance for the WLS method was similar to the NT method for these two $\Delta\phi$ s for 4R with no effect of weighting observed. This was attributed to large velocity overestimations contributed from the two very noisy signals from beams transverse to the flow.

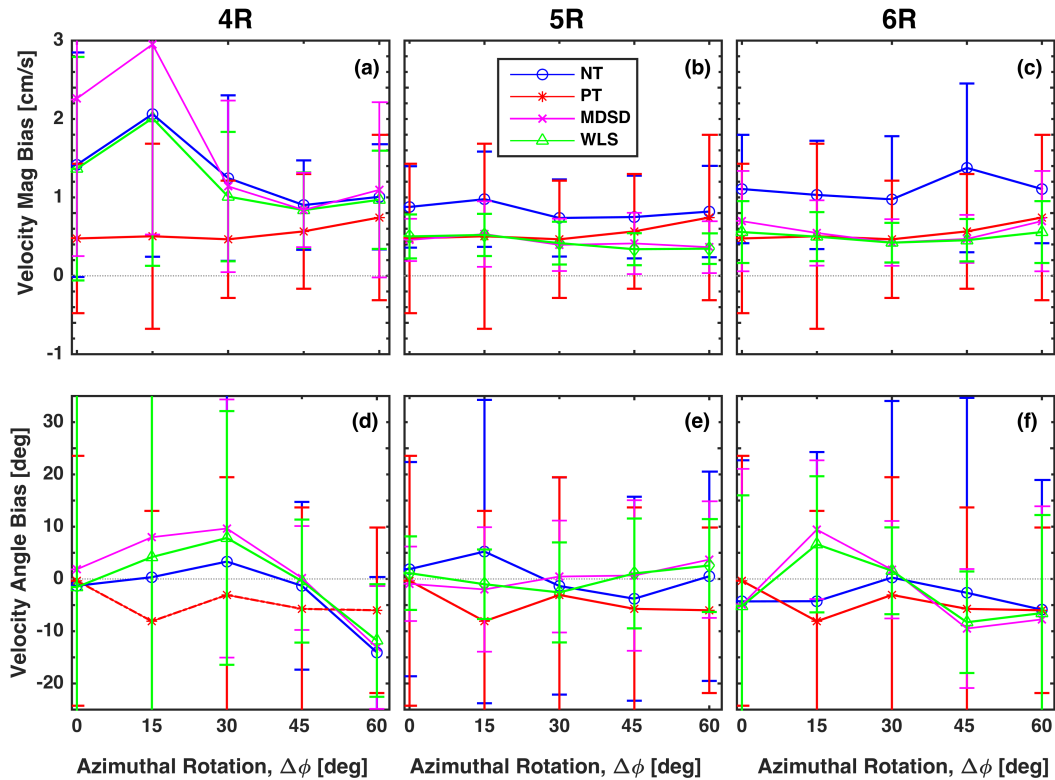


Figure 3.9: Velocity magnitude bias (a – c) and direction bias (d – f) comparing beam-selection methods for 4R to 6R configurations (as labeled) versus azimuthal rotation for $\beta = 20^\circ$ when measured a theoretical velocity of 2 cm/s. Biases are averaged differences with respect to the theoretical value over 160 independent measurements for each orientation. Error bars represent the standard deviations (SD) over 160 measurements. Note the error bars in (d) extend beyond the plotted region ($40^\circ \leq SD \leq 51^\circ$).

Comparison with Fig. 3.4(b) explicitly shows that for these $\Delta\phi$ s, only two beams should be expected to have Doppler shifts exceeding WF_{eff} . The PT method, on the other hand,

eliminated the noisy transverse beams leading to improved velocity magnitude estimates, but with < 3 beams, the velocity direction estimation is then compromised, as illustrated in Fig. 3.9(d), where angle bias increased from $< 1^\circ$ at $\Delta\phi = 0^\circ$ to $\sim 8^\circ$ at $\Delta\phi \geq 15^\circ$. With the PT method, the angle bias (3.9) stayed within 10° when averaged over these orientations, but often with higher standard deviations, especially for 4R ($>40^\circ$). The PT method at $\beta = 20^\circ$ [Fig. 3.9(b) and (e)] shows an average bias of $\sim 30\%$ in the velocity magnitude but with relative standard deviation decreasing from 50% for 4R to 25% for 5R, and the direction bias decreased from 5° to $< 2^\circ$ with slightly reduced standard deviation when using 5R. In general, with $\geq 5R$, all three beam-selection methods performed well over all azimuthal rotations, with WLS showing the least variance in both magnitude and direction for all orientations.

3.3.2.4 Beam-Selection Methods Perform Equally Well for $\geq 4R$ at Higher Velocities

Fig. 3.10 extends the analysis to higher-magnitude velocity vectors, comparing the relative error in velocity magnitude and direction, averaged over all azimuthal orientations, for the different selection methods for 4R to 6R configurations, again at $\beta = 20^\circ$. Results confirm an overall improvement in terms of reduced bias and variance in the velocity magnitude and direction estimation for all selection methods for increasing velocity magnitudes. At high velocities (≥ 5 cm/s), all configurations with $\geq 4R$ perform equally well with relative error $\leq 3\%$ in magnitude and a bias of $\leq 4^\circ$ in direction. Notably, for 5R, the bias in the angle estimation is within 2° for all velocities ≥ 2 cm/s. At velocities ≥ 3 cm/s, the equivalence of the WLS, PT and NT methods in the velocity bias suggests that all receivers detect a Doppler shift greater than the wall filter cut-off, and the PT method includes a signal from all beams for the estimation. The WLS method,

however, shows improved precision in the estimations. The MDSD method, which specifically picks out only three beams, typically showed greater error compared to the other methods.

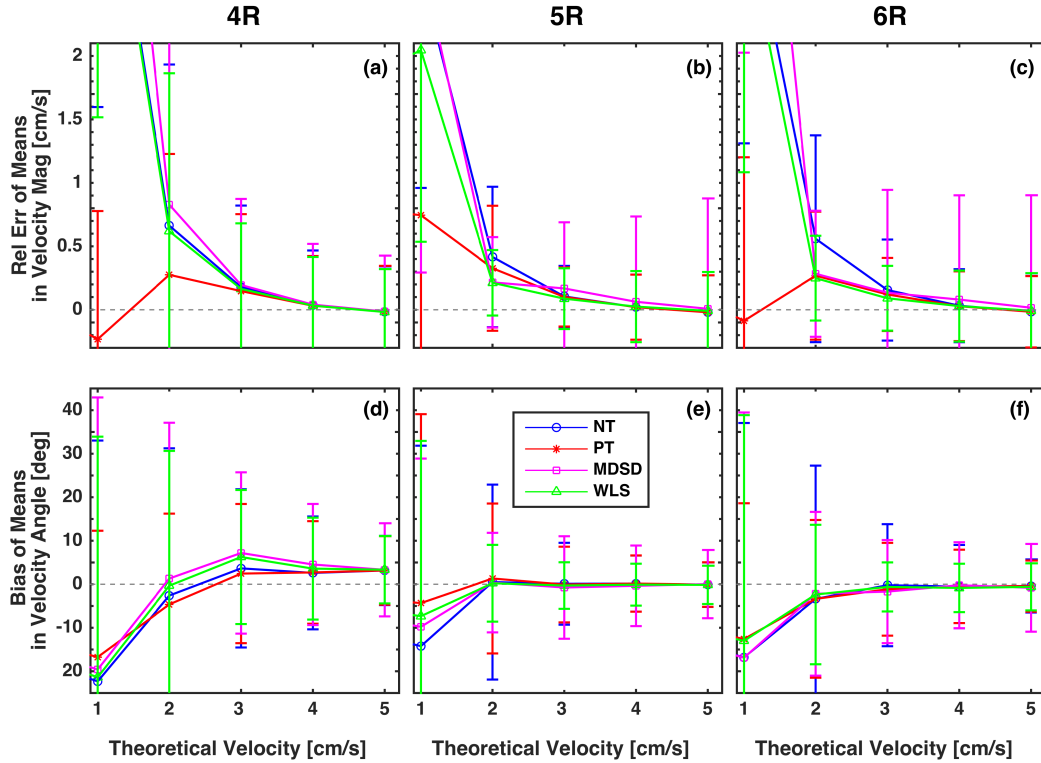


Figure 3.10: Relative error of the means in velocity magnitude (a-c) and direction bias (d-f) comparing beam-selection methods for a theoretical velocity range of 1 to 5 cm/s for 4R to 6R configurations (as labeled) at $\beta = 20^\circ$. Biases are averaged differences over all velocity vector orientations ($\Delta\phi = 0^\circ, 15^\circ, 30^\circ, 45^\circ, 60^\circ$ relative to y axis). Error bars represent the standard deviations over 800 measurements.

For a velocity of 1 cm/s, very high bias and standard deviations were observed for the WLS and the MDSD methods. At this velocity, most of the contributing Doppler shifts were below the WF_{eff} , therefore the filtered signals had very poor SNR. The PT method eliminated contributions from some or all beams leaving at most two Doppler shifts for the resultant 3D velocity estimation. This resulted in reduced magnitude bias

but very large variances and large angle biases (up to 24°). The percentage of data points for which all Doppler shifts were eliminated (i.e. no velocity estimation possible) was 62%, 5%, and 48%, for 4R, 5R, and 6R configurations, respectively; in comparison, for a velocity magnitude of 2 cm/s, this was only 5% for 3R and $\leq 1\%$ for $\geq 4R$.

3.4 Discussion

A quantitative analysis was done to assess the relative benefit of increasing the number of receiver beams to more accurately estimate low 3D velocities spanning the wall-filter cut-off while also considering the effects of varying inter-beam angle and beam-selection methods. Analysis was performed on flow with a range of velocity magnitudes and orientations. The results provided insight for suitable choices of the number of receivers and the inter-beam angle for a design of a future 2D array for applications where accurate estimates of 3D blood velocities with Doppler shifts close to the wall filter cut-off are desired for accurate velocity mapping and shear stress measurements. Examples of such applications include vector Doppler imaging in regions near the arterial wall, in recirculation, and distal to a destabilizing jet in a carotid artery.

The theoretical geometric results (Fig. 3.3 and 3.4) suggested that an inter-beam angle $\geq 20^\circ$ should be chosen for configurations with $\geq 5R$ so that ≥ 3 receiver beams provide Doppler shifts exceeding the wall filter cut-off for almost all orientations, whereas no such inter-beam angle existed for configurations with 3R and 4R.

For low velocities (≤ 2 cm/s), the experimental results were consistent with the geometric calculations. Experimentally, with $\leq 4R$, the accuracy of the velocity estimation is sensitive to both the relative velocity vector orientation and the selection

method. When the number of beams was increased to $\geq 5R$, the configurations became insensitive to the selection methods, especially with $\beta \geq 20^\circ$ (Fig. 3.8), which enabled more beams to exceed the wall filter cut-off.

For higher velocities (Fig. 3.10), above 2 cm/s, all configurations with $\geq 4R$ performed equally well for all selection methods, as expected. For example, for 4R at a velocity of 5 cm/s, error in estimation of velocity magnitude and direction was reduced to $\sim 2\%$ ($\pm 7\%$) and 3° ($\pm 8^\circ$) respectively. The results indicate that when estimating low velocities, e.g. near the wall of a carotid artery for estimations of wall shear stress, at least a 5R configuration with $\beta \geq 20^\circ$ should be used, whereas for higher velocities such as in the jet, any of the proposed configurations with $\geq 4R$ should work satisfactorily provided the PRF is sufficiently high to avoid aliasing.

Overall, the direction bias was lowest and had the least standard deviation, $< 1^\circ$ and 9° respectively, when applying the WLS method for a 5R configuration with $\beta \geq 20^\circ$ on a velocity vector of 2 cm/s (i.e. velocity components near the -20 dB frequency of wall filter). Furthermore, with a magnitude bias of approximately 0.4 cm/s ($\sim 22\%$) with standard deviation < 0.3 cm/s (13%), the 5R configuration demonstrated the best accuracy, precision, and reliability. With an odd number of receivers, the 5R inherently lacks symmetry about the flow axis whenever $\Delta\phi \neq 0^\circ$, and thus has only one beam close to 90° for any velocity vector orientation, making it less sensitive to orientation. The even-numbered configurations have opposing paired beams that duplicate the information, including noisy beams when present. This is also demonstrated in Fig. 3.8 for the NT method, where 5R shows the lowest biases and standard deviations observed

in both magnitude and direction for all $\beta \geq 15^\circ$, compared to the rest of the configurations. Asymmetric configurations with more than five receivers presumably would also be effective, but these were not tested because of the long experimental time required to construct an asymmetric configuration by rotating the apertures about the transmit axis.

The performance of multi-receiver configurations may be helpful for real-time assessment of rapidly changing flow where higher than normal frame rate is needed thus requiring lower ensemble size. Velocity estimates from each beam will become noisier with smaller ensembles; therefore, a 5R configuration, for example, may still out-perform other multi-receiver configurations, but only at some velocity > 2 cm/s. Alternatively, a greater number of receivers may be required for equivalent performance at an increased frame rate. We still suggest that asymmetry is important as it reduces redundancy. Therefore, an asymmetrically arranged 6R or a 7R configuration may provide similar results at a higher frame rate compared to those obtained here at a lower frame rate (14 fps) from a 5R.

In general, the estimates of velocities in the transition region of the clutter filter are prone to overestimation with the autocorrelation method. Another approach would be to use speckle tracking with PWI compounding (multiple-angle plane waves compounded), which does not require a wall filter (Fadnes et al. 2015), therefore the ability to detect the low blood velocities depends on spatial resolution and frame-rate. It is a 2D-vector technique. However, a 3D speckle tracking requires a large number of calculations and therefore is very computationally demanding. Although performance of VDUS systems for velocities in the transition region can be improved by using a clutter

filter with a steeper transition, such as using a polynomial regression filter (Bjaerum et al. 2002; Fadnes et al. 2015), our study suggests that adding more receivers, i.e. more viewing angles to compensate for any loss, can further improve the estimates of these low velocities. A filter with a steeper transition band could provide a cut-off velocity < 2 cm/s. In such a case, our recommendation regarding the number of receivers and the inter-beam angle would be valid down to a lower cut-off velocity. Conversely, if the wall-filter cut off is higher than the 10 Hz cut-off shown in Fig. 3.3, then our recommendations are valid only above a higher cut-off velocity. To illustrate how these recommendations apply at a different wall filter cut-off, Fig. 3.11 shows results similar to Fig. 3.3, but for a 50 Hz wall-filter cut-off at a velocity cut-off of 5 cm/s. Similar plots with only 3R, 4R, and 6R configurations were presented in [(Hussain et al. 2012), Fig. 2]. Fig. 3.11 adds the results for 5R (c) and 8R (e) for completeness. For a fair comparison with results shown in this study (Fig. 3.3), the theoretical plots are done for 10 cm/s at 50 Hz WF_{eff} (Fig. A-3). Results demonstrated the same recommendations for the number of receivers and the inter-beam angle as made from the results from Fig. 3.3.

Note that although the phantom used in our study is wall-less, the acquired Doppler signal still has clutter originating from side-lobe reverberations within the overlying tissue-mimicking material cast around the flow channel; in this case, the clutter has a zero Doppler frequency because there is no tissue motion. Therefore, our conclusions would be equally applicable to walled and wall-less phantoms without influencing the blood velocity measurements, assuming any wall clutter signal can be sufficiently removed.

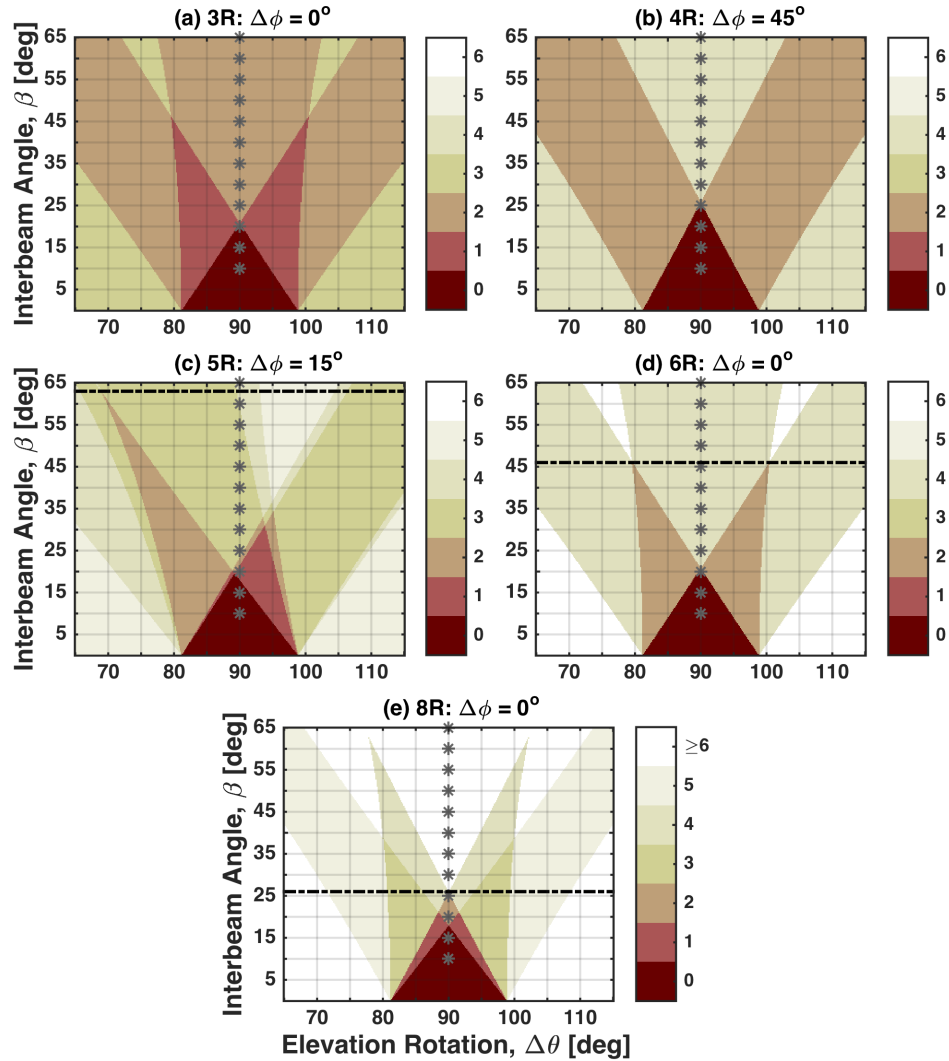


Figure 3.11: Color-encoded plots demonstrating theoretical determination of the number of receivers with Doppler shifts exceeding an WF_{eff} of 50 Hz for 3R to 8R configurations (as labeled) with varying inter-beam angle from $\beta = 5^\circ$ to 65° . Each is shown for a 5 cm/s velocity vector rotated through elevation angles $\Delta\theta$ from 65° to 115° relative to the x-axis and for the worst-case of azimuthal angles, $\Delta\phi$. The data points labeled with an asterisk (i.e. one column per configuration) correspond to parameters applied in the experiments and the worst-case $\Delta\phi$. The black dashed-line represents the minimum inter-beam angle for which Doppler shifts from ≥ 3 receivers exceed the WF_{eff} for all velocity orientations.

Overall, the consistently good performance of the PT method suggests it is the best option out of all three selection methods, but its performance is contingent upon the choice of a user-defined threshold value. The WLS and MDSD methods, on the other hand, do not require a user-defined threshold value. However, the MDSD method lacked reliability in picking the best beams' Doppler shifts as it does not discriminate sufficiently between flow and tissue power for the low-power beams' Doppler shifts, as observed for the 4R configuration [Fig. 3.9(a) and (d)]. The WLS method showed accuracy comparable to the PT method when the number of receivers was $\geq 5R$, but, because it provides the best precision (least variance) of all methods, WLS is preferable. Conversely, for cases where the number of receivers is $\leq 4R$, or the inter-beam angle is $\leq 15^\circ$, or the velocities are very low (< 2 cm/s), the PT method performed better than WLS. In these cases, for beams that carry only noise or have low SNR, the PT method can exclude the resulting unreliable velocity estimates altogether instead of including them with lower assigned weighting as is done with the WLS method. A more robust option for overall improved accuracy and precision of the velocity estimates could be to combine the WLS and PT methods. First, the PT method can be applied to eliminate the obviously low SNR Doppler shifts and then the WLS method is applied to the remaining beams. With the combined approach, the PT method should satisfactorily remove any obviously noisy estimates even if the user-defined threshold value is sub-optimal. However, this idea needs further investigation.

Our results suggest that five receivers with a minimum inter-beam angle of 20° should be used for more accurate and precise estimation of these low velocities. For a 2D array, the diameter would need to be at least 2.5 cm to reach a depth of 2 cm (typical

depth of superficial arteries, such as the carotid artery) for an inter-beam angle of 20° (i.e., Doppler angle $\sim 80^\circ$) and receiver aperture of ~ 1 cm. The size of the probe increases linearly with depth; therefore, the imaging depth may be limited or a larger probe would be required for deeper arteries. The trade-off is then to reduce the inter-beam angle, which may work for higher velocities. For example, for a velocity of 5 cm/s with the PT method, reducing the inter-beam angle from 20° to 15° for 5R (Fig. A-4), the error in velocity magnitude increases from $\sim 2\%$ to $\sim 12\%$ with almost no change in the accuracy of the direction estimates; the precision for both magnitude and direction is not affected greatly by lowering the angle to 15° . Note that the size of a 2D array depends on the inter-beam angle for a specific depth, but not on the number of beams. A limitation in the design of a multi-receiver 2D array is the need for a large number of addressable elements. As an example, for the design of a 5R configuration (i.e., 1Tx and 5Rc) with similar aperture areas as used in this study (32 elements in a linear array, each of size $1\lambda \times 10\lambda$) would require 320 elements for each receiver and transmitter in a 2D-array with an element pitch of 0.3 mm (1λ) along each dimension. A commonly used 2D array uses a 64×64 element grid. Schematic of a 5R configuration on such a 2D matrix is shown in Fig. 3.12 with circular transmit and receive apertures. Note that the apertures are shown as perfect circles, but in practice when the circular boundary passes through an element, the element is then either included or excluded depending on the criterion used to accept or reject the element for apodization (Smith et al. 1991). The size of the array is 1.92 cm x 1.92 cm with a total of 4096 elements when a similar pitch (0.3 mm) to that of the 1D array is used. The total number of elements that would need to be wired to reach a fixed maximum possible depth of 1.8 cm would be 1920 (6×320). If one needs to slide the

aperture for multi-gating to a shallower depth of up to ~ 0.8 cm, then it would increase the number of wired elements to approximately 2320. A circular aperture of 320 elements will have a diameter of 0.6 cm, which is smaller than the aperture length (0.95 cm for a linear array) used in this study. Although increasing the number of beams does require added hardware and more computing power, processing multiple receive beams is an inherently parallel process that is well suited to modern multi-core processors.

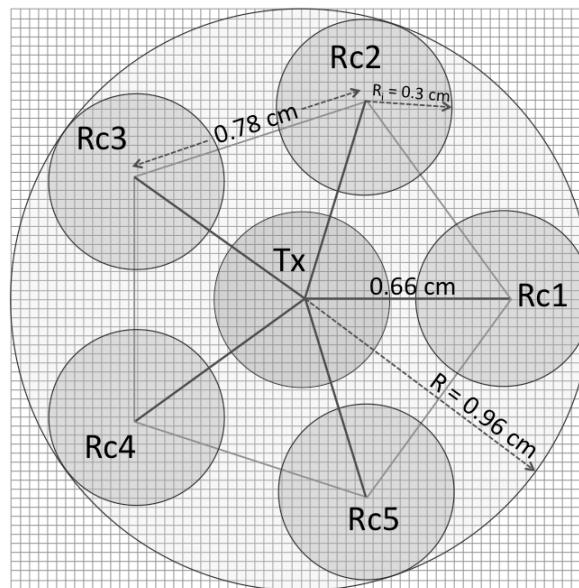


Figure 3.12: An example of possible 2D probe design for a 5R configuration using a 64 x 64 element grid with each element pitch of 0.3 mm along both directions. Note that the outline of these circular apertures will be pixelated either including or excluding the elements that lie on the aperture boundary.

In the future, a parametric simulation study for the design of a 2D probe would be useful to investigate these trade-offs. Also, the effect of considerations that could be difficult to study experimentally, such as sample volume misregistration and differences in attenuation along different receive beams, could also be simulated.

Chapter 4

4 Vector Doppler Ultrasound Aperture-Translation

This chapter presents the results and discussion of the potential of an aperture-translation method for improved estimation of low velocities that lie close to and within WF_{eff} . The method improves the Doppler power by increasing the phase-shift of the received signal thus improving the accuracy of the low velocity estimates. Section 4.1 presents the results demonstrating the proof of concept using a mechanical aperture-translation method, which is considered to be an idealized version of the electronic aperture-translation method because it allows independent and precise variation of the flow-imaging parameters. The feasibility of the electronic version, which is more suitable for clinical implementation, is compared to the mechanical version and is presented in sections 4.2 and 4.3. The discussion for these results is given in section 4.4. Analysis is performed only on the magnitude of the 2D vector velocities, using parabolic flow in a straight vessel (small-ID flow phantom), as the data were taken at only one orientation with azimuthal and elevation angles of 0° and 90° , respectively.

The terminology introduced for various sweep speeds is abbreviated for the type of translational sweep method used – ‘M’ for mechanical and ‘E’ for electronic – followed by the number representing the sweep speed in cm/s. As an example, M2 represents mechanical translation with sweep speed of 2 cm/s. Note that the conventional method in this study is the 2D VDUS method with stationary apertures and is referred to as Case-0. The terms ‘conventional’ and ‘Case-0’ are used interchangeably in this chapter.

4.1 Mechanical-Sweep Method

Figure 4.1 shows the mean Doppler frequency profiles, processed from the left and right receiver beams' data, obtained using the M-sweep method for varying sweep speeds and ensemble sizes (a–d). Each profile shown is an average over 70 independent measurements taken over seven different locations with 10 repeated measurements at each location in the vessel. For visual clarity, error bars showing SD are not included in the plots. Standard deviations in the tissue and the center of the lumen (excluding aliased velocities) ranged between 5 to 10 Hz for sweep speeds ≥ 2 cm/s. For the conventional method and M1, the SD in the TMM and low velocity regions (close to the wall) were up to 20 Hz with larger ensembles and up to 30 Hz with lower ensembles, and it converged for all cases (i.e. to < 10 Hz) at flow velocities ≥ 2 cm/s. The Doppler data were further processed to obtain 2D velocity profiles for the different sweep speeds and compared with that of the conventional 2D-VDUS method and the theoretical profile (Fig. 4.2).

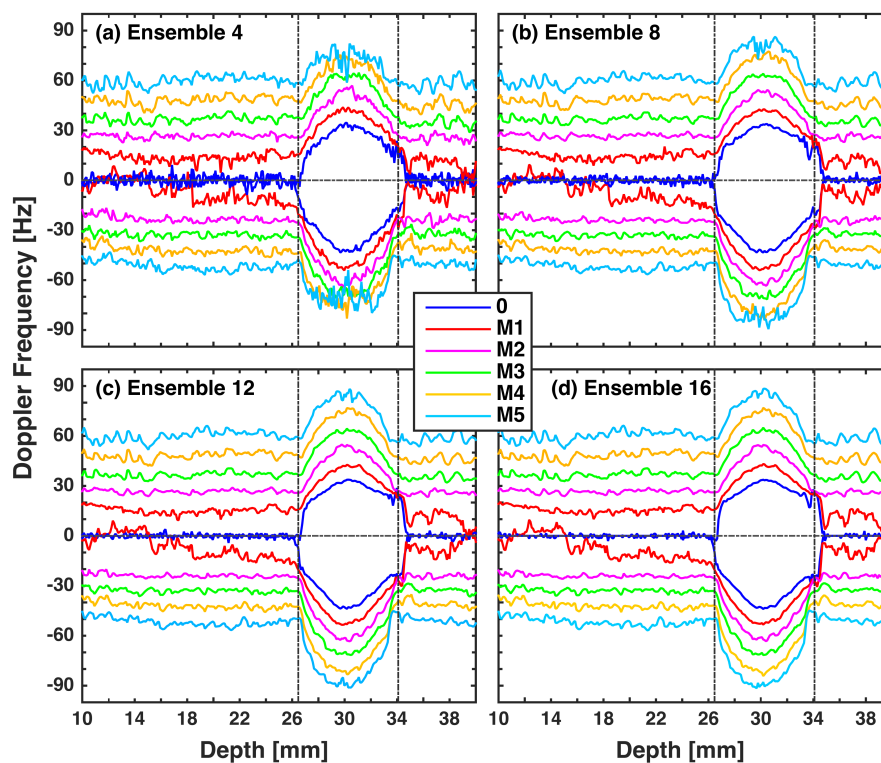


Figure 4.1: Mean Doppler frequency profile for varying mechanical-sweep speeds (0 – 50 mm/s) for ensemble sizes (a – d), in the stationary TMM and for parabolic flow in the CCA-vessel of the carotid flow phantom with a peak velocity of 3.4 cm/s. The positive and negative Doppler shifts are from the left and right receiver beams, respectively, at an inter-beam angle of 20° and a PRF of 223 Hz. Doppler shifted frequencies are averaged over 70 independent measurements. The vertical dashed-lines separate the lumen and the TMM regions.

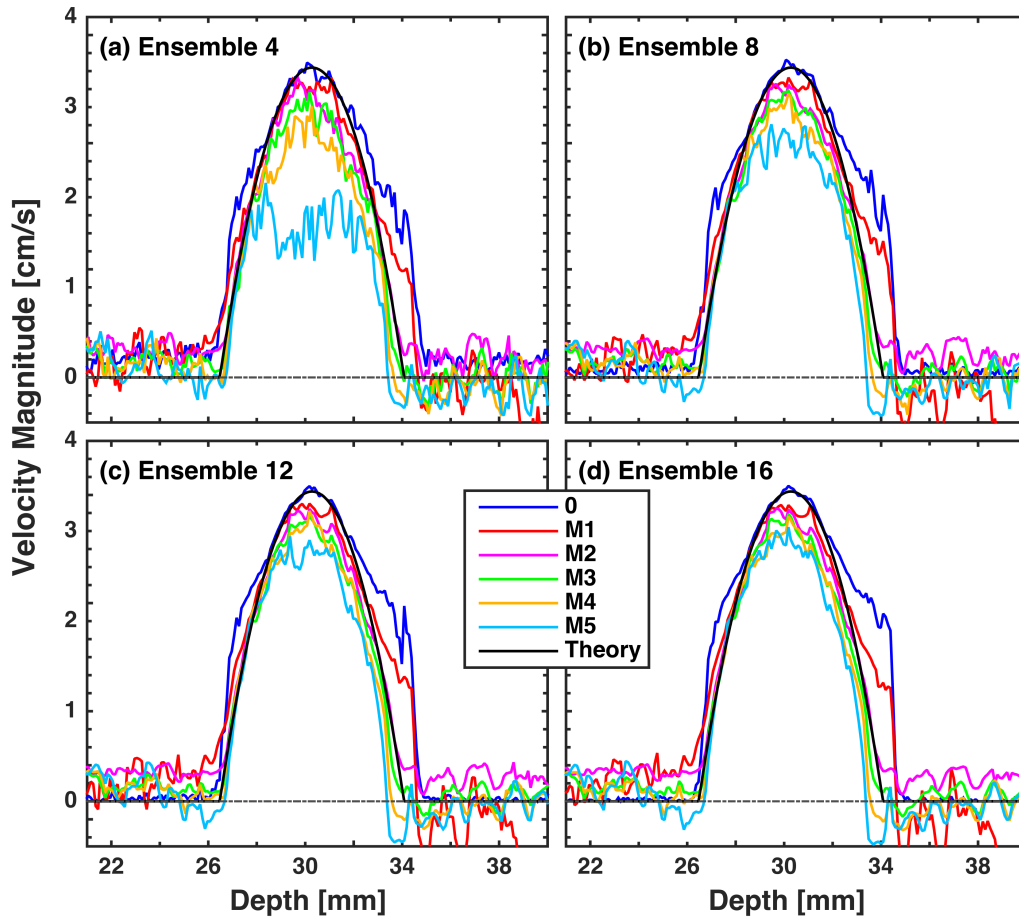


Figure 4.2: Mean resultant velocity magnitude profiles reconstructed from the left and right receivers' Doppler shifts for varying sweep speeds (0 – 50 mm/s) for four ensembles (a – d), in the TMM and in the CCA of the carotid flow phantom with a peak velocity of 3.4 cm/s at $\beta = 20^\circ$ and a PRF of 223 Hz. The velocities are averaged over 70 independent measurements.

As expected, the velocity magnitude estimates (Fig. 4.2) have smoother profiles (lower noise) for larger ensemble sizes. Note that the low flow velocities ≤ 2 cm/s are the focus of this chapter because the Doppler frequencies related to these velocities lie close to and within the WF_{eff} applied in this study. The estimation of velocities on the deeper side of the vessel is observed to be less reliable as shown by the shoulder [Fig. 4.2(a)-(d)]. This is presumed to be a consequence of lower SNR due to frequency dependent

attenuation. All subsequent analysis was completed using data from the shallower half of the vessel.

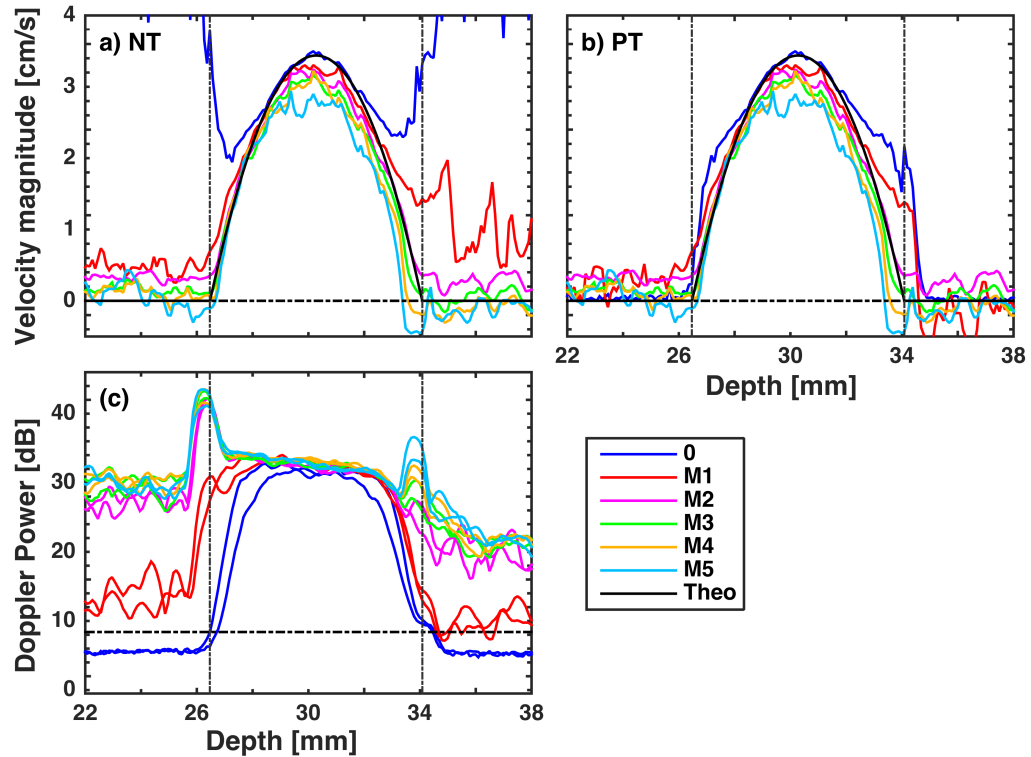


Figure 4.3: (a) Example of resultant mean velocity magnitude profiles reconstructed from the left and right receivers' Doppler shifts with no power threshold applied to the data (b) resultant mean velocity profiles after applying power threshold, and (c) mean Doppler powers showing constant power threshold applied (gray horizontal line) to all data, for varying sweep velocities (0 – 50 mm/s) for an ensemble size of 12 at $\beta = 20^\circ$ and a PRF of 223 Hz, in the TMM and in the CCA of the carotid flow phantom with a peak velocity of 3.4 cm/s. Resultant velocity magnitude and Doppler powers are averaged over 70 independent measurements. The vertical dashed-lines separate the lumen and the TMM regions.

The underestimation of the resultant averaged flow velocities at higher sweep speeds, i.e. M4 and M5, specifically at lower ensemble sizes, is due to aliasing. This is more obvious from the single-acquisition velocity profiles (not shown in this section)

rather than the averaged velocity profiles. This will be explained in more detail in the next section.

Fig. 4.3 (a-b) demonstrates the effect of power threshold (PT) on the estimation of the resultant velocity magnitude obtained from the M-sweep aperture-translation method. In Fig. 4.3(b), a constant power threshold of ~ 8.4 dB was applied to all the data irrespective of the sweep speed before reconstructing the resultant 2D velocity. This constant user-defined value was set at 40% above the average tissue Doppler power (~ 6 dB with respect to a power level of 0 dB). The tissue Doppler power was obtained from the conventional method. The applied power threshold greatly improved the tissue and the low-velocity estimates for the conventional method, as well as for M1 at the lower half of the flow profile. This can be seen in Fig. 4.3(a) with no threshold for the conventional and M1 case (blue and red curve, respectively), showing high overestimations for the tissue and the low velocities. These overestimated velocity regions have very low Doppler power (Fig. 4.3c) and applying the stated threshold removes this artifact (Fig. 4.3b). However, for M2 and higher sweep speed cases, Doppler power is well above the threshold for all flow velocities and even for the tissue signal (Fig. 4.3c), thus no threshold criterion was required. To be consistent, the power threshold was applied to all cases irrespective of the sweep speeds. Note that all the subsequent analysis in this study, from Fig. 4.4 onwards, is performed on the data from the upper-half of the vessel, as well as from the TMM above the vessel. This is because of higher attenuation (lower SNR) of the signal at a greater depth causing overestimation of the signal for lower velocities. This is more noticeable for the conventional method and for M1 for the deeper half of the flow profiles (Fig. 4.3).

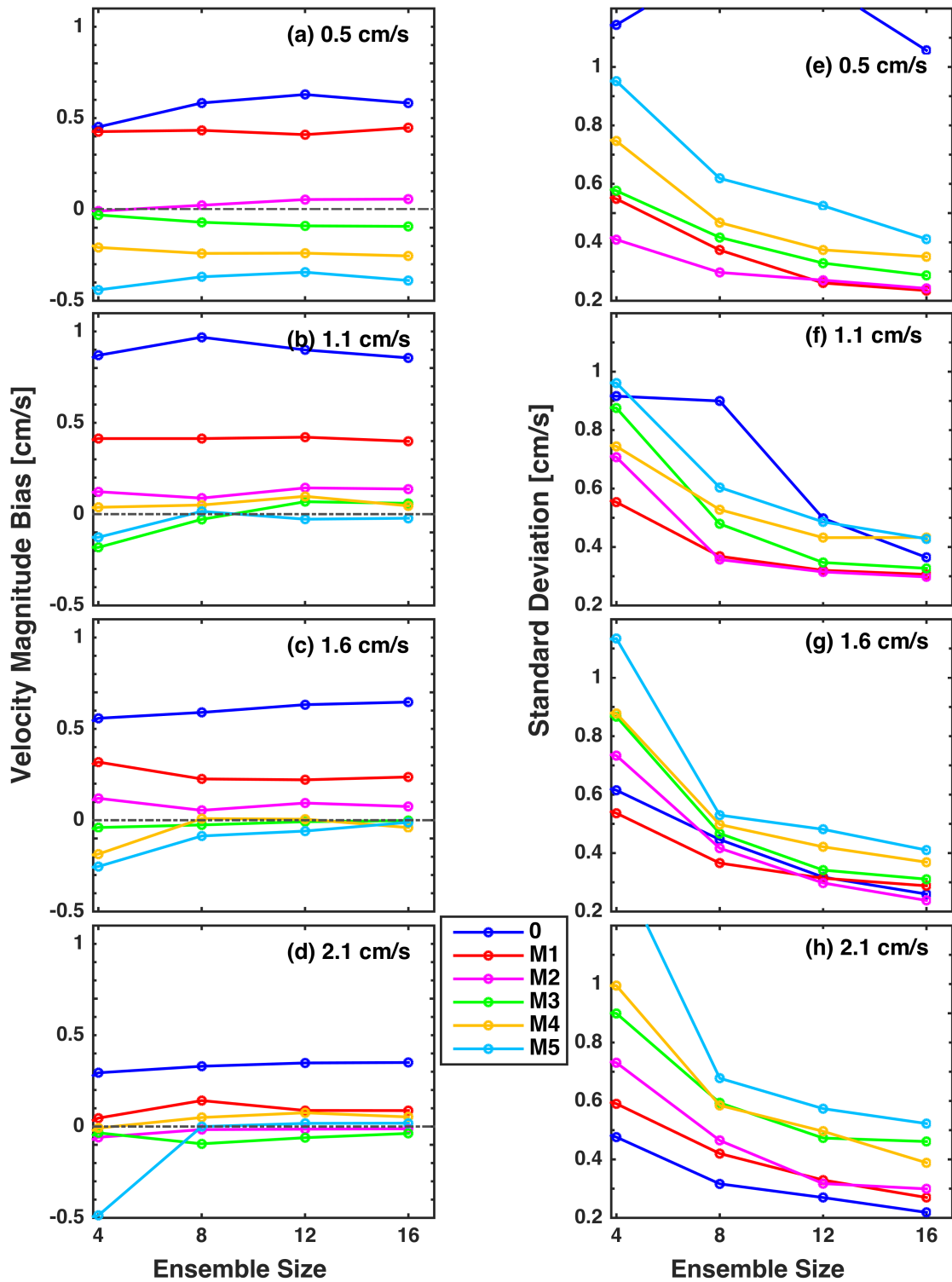


Figure 4.4: Velocity magnitude bias (a-d) and standard deviations (e-h) for four specified flow velocities (as labeled) measured at $\beta = 20^\circ$, comparing five sweep speeds for ensemble sizes ranging from 4 to 16. Biases are differences averaged over 70 independent measurements.

Fig. 4.4 assesses the impact of various sweep speeds and ensemble sizes in terms of their accuracy and reliability relative to the conventional method, where velocity biases (a – d) and SDs (e – h) for each sweep speed are plotted as a function of ensemble size for flow velocities ranging from 0.5 – 2.1 cm/s. Overall, the velocity bias is independent of the ensemble size for all cases. The bias is lowest for M2 and M3 and stays within 0.2 cm/s for all ensembles and flow velocities shown. The accuracy for higher sweep speeds is compromised at lower flow velocities (0.5 cm/s), showing a bias of ~ -0.5 cm/s and ~ -0.3 cm/s for M4 and M5 respectively, which is comparable to that of the conventional method (~ 0.6 cm/s). This is because the low velocities are very close to the wall (e.g. 0.5 cm/s lies within ~ 0.03 cm) and thus with a sample volume length of 0.15 cm (5λ), the acquired Doppler signal would include both flow and wall signal with an increased frequency shift due to the aperture translation. Therefore, for higher sweep speeds the wall signal also shifts into the passband of the filter, where it is not attenuated. This introduces a negative bias in the velocity estimations, as observed for M4 and M5.

Overall, the standard deviations [Fig. 4.4(e)–(h)] decrease with increasing ensemble size for all aperture-translation methods. However, a consistently higher SD is observed for the conventional method at the lowest flow velocity, 0.5 cm/s [Fig. 4.4(e)] for all ensemble sizes (not fully visible in the plot as it extends off the scale). This is attributed to the low velocity signal being greatly attenuated by the wall filter thus reducing its SNR to such a low value that an increase in ensemble size does not increase its reliability. In general, the reliability increases with decreasing sweep speed for all flow velocities for a given ensemble size. For M1 and M2, the SD stays within 0.3 cm/s when the ensemble size is ≥ 12 , which corresponds to a timeframe of ~ 54 ms, with no

substantial improvement when increased to a higher ensemble of 16. Therefore, an ensemble of 12 has been used for the rest of the results, which would provide higher frame-rate (54 ms/scanline) than when an ensemble of 16 is used (72 ms/scanline). Overall, M2 shows minimum bias and SD for all flow velocities, suggesting that a sweep speed of 2 cm/s could be sufficient to overcome the adverse effects of a low SNR signal, while sufficiently low enough to avoid aliasing.

Relative error and relative standard deviation in the estimation of velocity magnitude are shown in Fig. 4.5, extending the comparison to higher flow velocities of up to 3 cm/s, which are above the WF_{eff} but still in the transition region of the wall filter. All ensemble sizes are shown here for completeness. These results are consistent with the previous results in Fig. 4.4, suggesting that there is no advantage of using an ensemble of 16 over 12, and lower ensemble sizes (4 and 8) are not sufficient (higher SD). As expected, relative error is reduced with increasing flow velocity below the aliasing limit for all sweep speeds. Focusing on the results for an ensemble of 12, M2 and M3 performed consistently better for all flow velocities, with an accuracy of $\leq 13\%$ and $\leq 18\%$ respectively. The relative SD [Fig. 4.5(c)] for both sweep speeds is $\leq 30\%$ for flow velocities ≥ 1.1 cm/s, while it is $> 50\%$ for a velocity of 0.5 cm/s. For higher flow velocities (> 2 cm/s), all cases performed equally well with relative error and relative SD within 12% and 22%, respectively

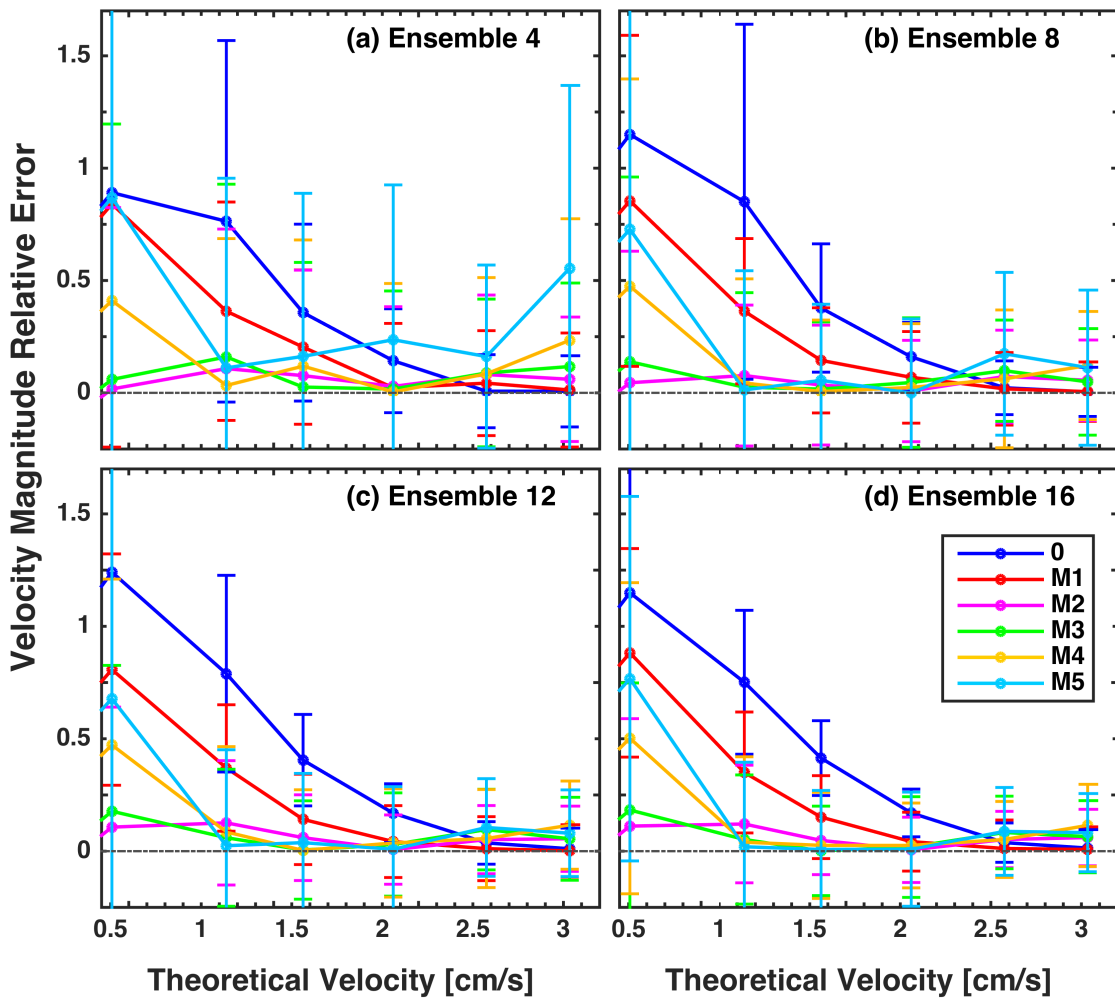


Figure 4.5: Relative error in velocity magnitude comparing varying sweep speeds for a theoretical velocity range of 0.5 to 3 cm/s for ensembles of 4 to 16 (as labeled) at $\beta = 20^\circ$. Relative errors are calculated from the estimated velocities averaged over 70 measurements. Error bars represent relative standard deviations.

Fig. 4.6 compares the accuracy and precision of the velocity magnitude estimates for inter-beam angles of 15° and 20° for a range of theoretical velocities measured with an ensemble of 12. It demonstrates the benefit of using aperture-translation to enable a reduction of the inter-beam angle, which is usually desired in order to reduce the probe size and/or to measure flow in deeper vessels. Comparing the results for the two inter-beam angles [Fig. 4.6(a), (b)], it is seen that similar or better accuracy can be achieved

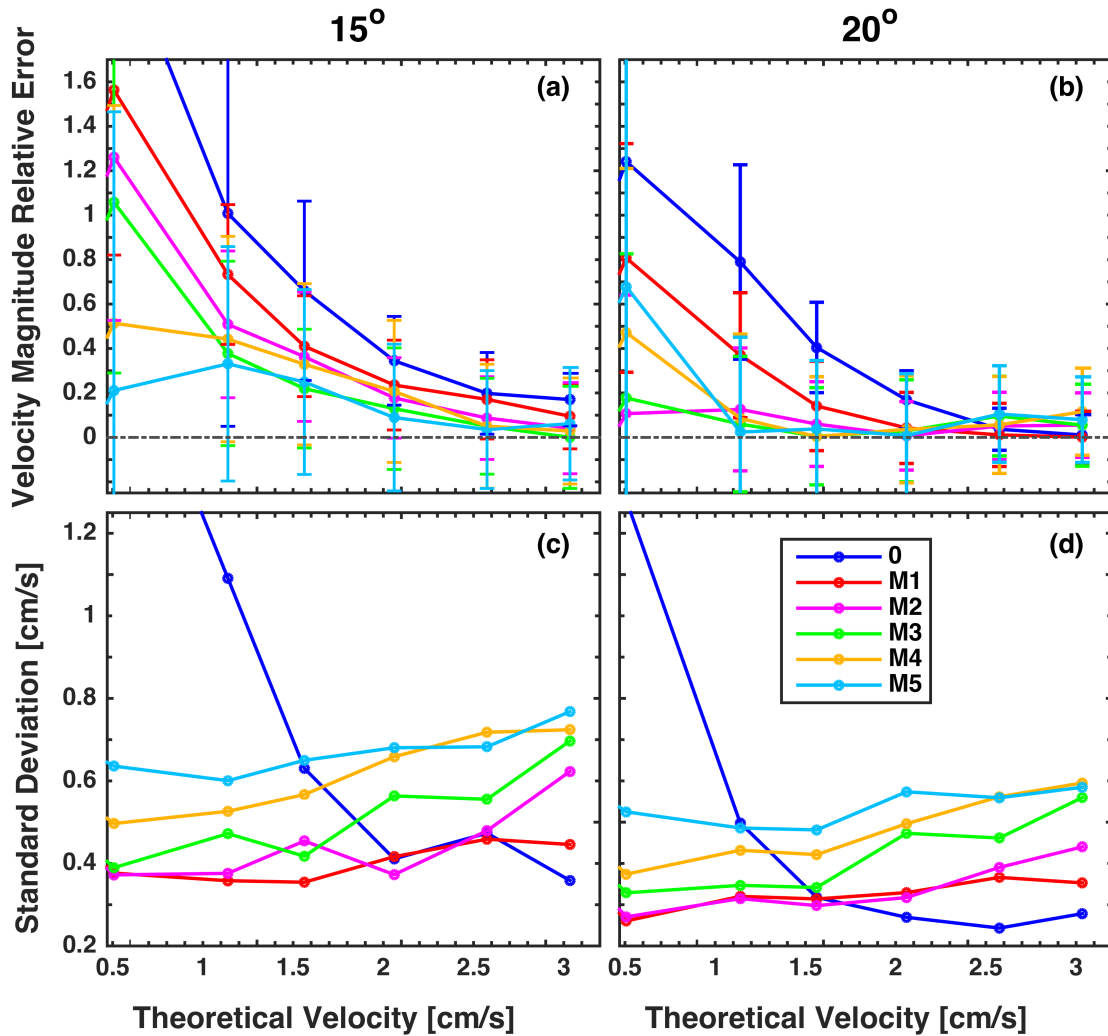


Figure 4.6: Relative error (a,b) and SD (c,d) in velocity magnitude comparing inter-beam angles of 15° and 20° at various sweep speeds for flow velocities ranging from 0.5 to 3 cm/s for an ensemble size of 12. Relative errors are calculated from the estimated velocities averaged over 70 measurements. Error bars (in a, b) represent the relative standard deviations over 70 measurements.

using the aperture-translation method at a smaller inter-beam angle ($\beta = 15^\circ$) than what can be obtained at a higher angle ($\beta = 20^\circ$) with the conventional method. As an example, for M2 at $\beta = 15^\circ$ and for a flow velocity of 1.1 cm/s, the error was reduced by 28 percentage points with the standard deviation reduced by 11 percentage points, compared

to Case-0 at $\beta = 20^\circ$. At higher velocities > 1.1 cm/s, the accuracy of M2 at $\beta = 15^\circ$ is comparable to the accuracy of Case-0 at $\beta = 20^\circ$ at a small cost in the reliability of the estimates.

4.2 Electronic-Sweep Method

To assess the practicability of the E-sweep method (sec. 2.1.4), the velocity magnitude profiles were generated and compared with the theoretical profiles (Fig. 4.7). These velocity data were compared later with that from the M-sweep method.

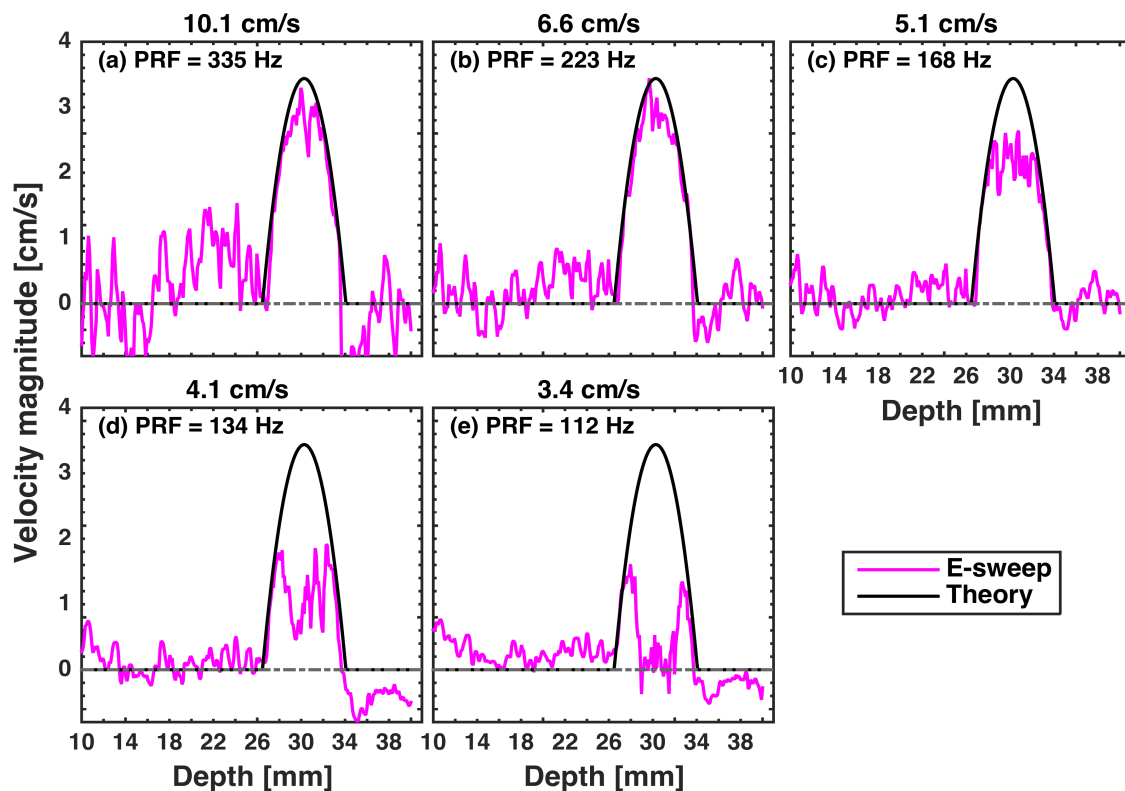


Figure 4.7: Mean resultant velocity magnitude profiles reconstructed from the left and right receivers' Doppler shifts for varying electronic-sweep speeds for an ensemble of 12, in the TMM and in the straight-vessel flow phantom with a peak velocity of 3.4 cm/s at a β of 15° . The flow velocities are averaged over 60 independent measurements.

As previously mentioned in Chapter 2 (section 2.3.2.2), the sweep speeds obtained with the E-sweep method are dependent on the PRF (inverse of the pulse repetition interval or the time-step), indicating that a reduction in the sweep speed by a factor of two reduces the required or effective PRF by half (Fig 2.4). Therefore, the velocity profiles shown for each sweep speed have a different effective PRF. Note that aliasing starts to occur at a flow velocity of ~ 2 cm/s for E3.5 and E4 and at ~ 2.5 cm/s for E5, which are lower than the expected aliasing velocities calculated for each PRF. For example, aliasing should occur at a velocity of ~ 3 cm/s for E3.5 at a PRF of 112 Hz and $\beta = 15^\circ$.

Aliasing is demonstrated in Fig 4.8, which shows representative single scanlines from the data presented in Fig. 4.1 and 4.7, at various sweep speeds for M-sweep and E-sweep methods, as well as the conventional method. Aliasing can be seen for both M-sweep and E-sweep at lower Doppler frequencies than the expected Nyquist frequency (PRF/2) for one or both beams. This is due to higher fluctuations in the Doppler signal as is obvious from the scanlines, especially in the tissue. The standard deviation of the Doppler frequencies was calculated in the tissue region of 21 – 26 mm (50 data points, with each data point representing 40 independent measurements for a total of 2000) for each PRF for both the M-sweep and E-sweep. The SD of the Doppler frequency estimate increased with the sweep speed, i.e. ~ 3.5 Hz to ~ 6 Hz for sweep speeds of 3.5 cm/s and 5 cm/s, respectively, for both methods. However, the SD when normalized with the corresponding PRF showed consistently comparable values of ~ 0.03 , which varied only within ~ 0.005 . The conventional method also showed comparable normalized SD of within 0.036, when obtained at a central velocity of 3.4 cm/s (matched with M3.5 and E3.5) at a PRF of 112 Hz. These results suggest an increase in the variability of the

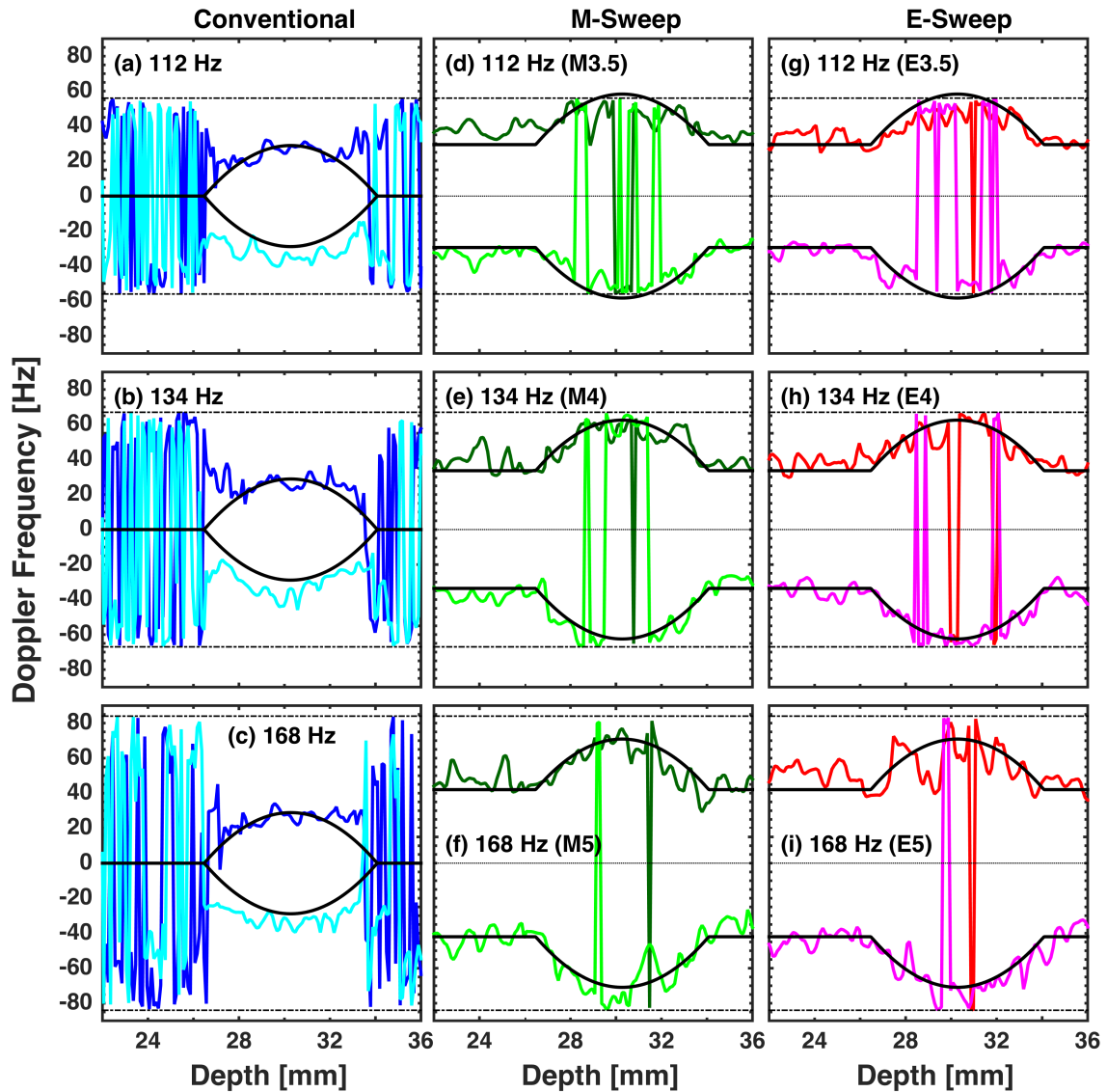


Figure 4.8: Left and right single-line Doppler frequencies for conventional (a-c), M-sweep (d-f), and E-sweep (g-i) methods using varying PRFs (112, 134, and 168 Hz), which correspond to sweep speeds of 3.5, 4, and 5 cm/s, respectively.

estimates with the PRF. Moreover, the right beam (with negative Doppler frequency profile) appeared to alias earlier than the left, which could be due to a slight asymmetry present between the two beams. Similar plots could also be generated at a PRF of 223 Hz to show that underestimation of the averaged Doppler frequencies at higher sweep speeds

(Fig. 4.1) is due to the aliasing of some of the scanlines that are used in the averaged signal, as presented in the previous section.

4.3 Electronic-Sweep Versus Mechanical-Sweep

To test the feasibility of implementing the method electronically, the velocity profiles obtained from both E-sweep and M-sweep are first compared qualitatively, as shown in Fig. 4.9 for the three matching sweep speeds of 3.5, 4, and 5 cm/s with their corresponding PRFs of 112, 134, and 168 Hz, respectively, at an inter-beam angle of 15° . The inter-beam angle chosen here is 15° instead of 20° in order to avoid aliasing for as large a range of flow velocities as possible. The velocity data for M-sweep were re-processed to match the PRF for the E-sweep data, where the E-sweep speeds were 3.4, 4.1, and 5.1 cm/s. Only these three sweep speeds were compared as shown in Fig. 4.9(a)–(c). For M-sweep, the sweep speed was limited to a maximum 5 cm/s, which is a limitation of the translational stage used in the study, whereas the E-sweep method only allowed a minimum speed of ~ 3.4 cm/s due to a hardware limitation as discussed in Chapter 2 (Section 2.3.2.2).

The velocity profiles [Fig. 4.9(a)–(c)] for both the E-sweep and M-sweep method are very similar demonstrating the equivalence of the principle of the two methods. For flow velocities below the aliasing limit, the velocity profiles from both versions of the aperture-translation method match more closely to the theoretical velocity profile than does the conventional method.

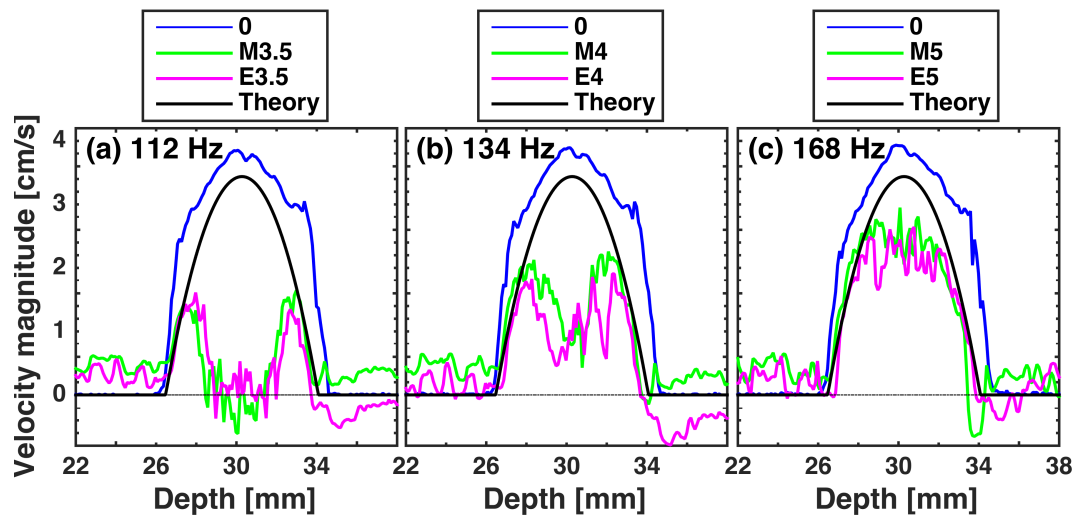


Figure 4.9: Mean resultant velocity magnitude profiles reconstructed from the left and right receivers' Doppler frequencies comparing M-sweep and E-sweep methods with case-0 and theoretical velocity profiles for three matching sweep speeds (3.5, 4, and 5 cm/s) with corresponding PRFs (as labeled) for an ensemble of 12 at $\beta = 15^\circ$. The velocities are averaged over 60 independent measurements.

Fig. 4.10 quantitatively compares the E-sweep and M-sweep methods with the 2D-VDUS conventional method and the theory, highlighting the velocities of 0.5 to 3 cm/s from Fig. 4.9. There are two key inferences obtained from the data. First, the two methods, E-sweep and M-sweep outperform the conventional method for low flow velocities within the aliasing limit. This is demonstrated in Fig. 4.10 (a)–(c). For all three sweep speeds, the E-sweep and M-sweep methods show better accuracy, with a relative error of $< 33\%$ for flow velocities ≥ 1.1 cm/s, compared to highly erroneous estimates (error reaching 100%) for the conventional method. The gaps between the SE bars for the aperture-translation methods and the conventional method are larger than the mean size of the error bars for velocities ≤ 2 cm/s. These large gaps suggest a statistically significant difference ($p \geq 0.05$) (Cumming et al. 2007) between the aperture-translation and the conventional method.

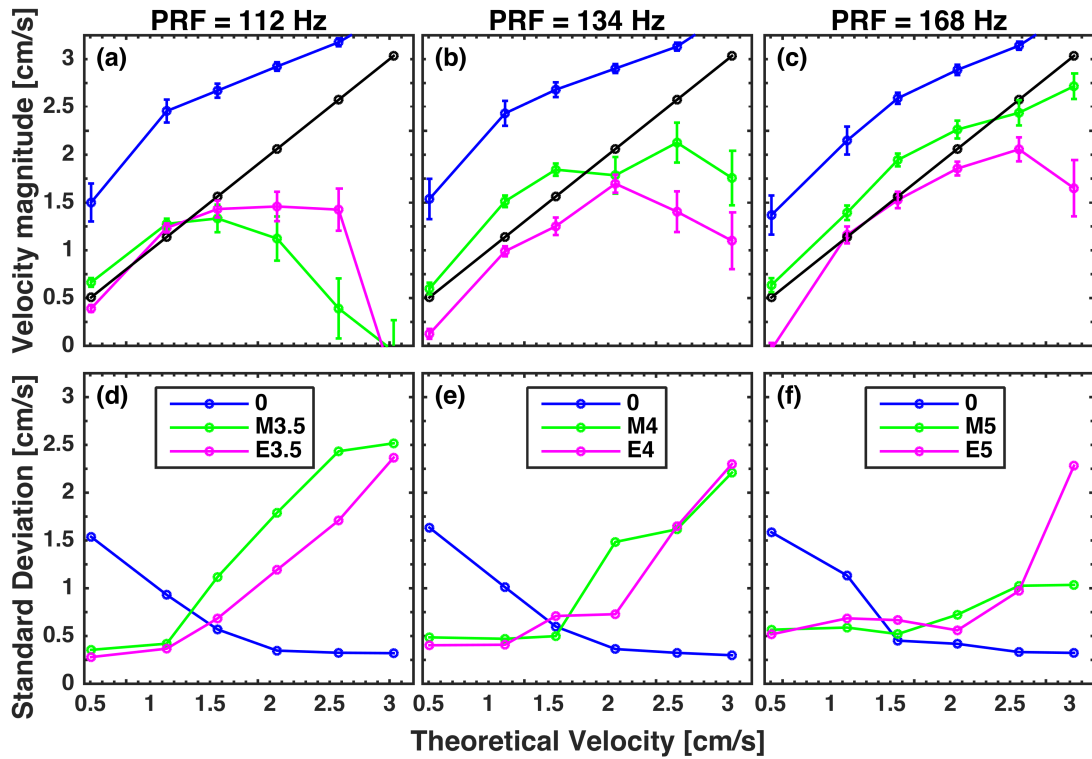


Figure 4.10: Velocity magnitude (a-c) comparing mechanical and electronic-sweep methods with conventional method for theoretical velocities ranging from 0.5 to 3 cm/s (in gray) for three matching sweep speeds (3.5, 4, and 5 cm/s) with corresponding PRFs (as labeled) for an ensemble of 12 at $\beta = 15^\circ$. Error bars represent the standard error over 60 measurements. Standard deviations (d-e) for the three methods are compared for the same flow velocities.

Second, the E-sweep method performs similarly or better than M-sweep. For all sweep speeds, below the aliasing limit, the error for the E-sweep method is within 20%, and the SD (≤ 0.71 cm/s) comparable to the M-sweep method for flow velocities ≥ 1.1 cm/s. For these velocities, the relative error for the M-sweep is typically higher and reaches as high as 33% [Fig. 4.10(b)], suggesting E-sweep to be the better choice for implementation.

4.4 Discussion

The proof of concept and feasibility for clinical implementation of aperture translation techniques using two receiver beams has been demonstrated. The method used the principle of increasing the phase difference to improve the SNR of the low velocity signals, which would otherwise lie below the wall filter cut-off. A quantitative analysis was performed on the M-sweep method with varying sweep speeds, ensemble sizes, and inter-beam angles to assess the overall potential of the aperture-translation method compared to the conventional method for estimation of low velocities, such as would be present in recirculation regions or near the wall, for improved shear stress measurements. Comparative analysis of the E-sweep and M-sweep results demonstrated the equivalence of the principle of the two implementations. Both E-sweep and M-sweep aperture-translation methods out-performed the conventional method for the low near-wall velocities ≤ 2 cm/s. E-sweep, which is the desired method for clinical implementation, showed improved performance relative to M-sweep, therefore suggesting potential for future development.

In general, a smaller ensemble size, i.e. higher temporal resolution, is desirable whenever possible to achieve a high frame-rate such as to capture rapidly changing flow. The compromise that accompanies high temporal resolution is the reduced SNR with smaller ensemble sizes, i.e. reduced reliability. For the aperture-translation method, the accuracy in the flow estimation was found to be independent of the ensemble size for all sweep speeds (M1-M5), which would allow the choice of ensemble size to be smaller but at a small cost of reduced precision (Fig. 4.4).

Fig. 4.5 compares the performance of varying sweep speeds, i.e. M1-M5, demonstrating that M2 performed consistently better overall, with improved accuracy (relative error within 13%) and reliability ($SD \leq 0.4$ cm/s) for all flow velocities (0 to 3 cm/s) and ensemble sizes ≥ 12 . These results suggest that M2 is a suitable choice for the filter parameters used in this study.

The aperture-translation method showed its benefit in enabling a reduction of the inter-beam angle, giving comparable accuracy to the conventional method at a large angle at a minimal cost of precision (Fig. 4.6). A smaller inter-beam angle is usually desired when imaging at a greater depth and/or for reducing the probe size.

It is understood that the choice of an appropriate PRF is essential for the aperture-translation method not just to avoid aliasing but also to avoid de-correlation of the signal between pulses. Reducing the PRF increases the inter-pulse interval and therefore increases the lateral distance travelled between pulses by the transmit beam. It has been pointed out by (Wagner et al. 1983) that speckle signal, during an ultrasound B-scan, de-correlates if the distance moved between two consecutive pulses is greater than 0.87 times the lateral resolution of the transmit beam. For the case of the aperture-translation technique, the lateral resolution of the transmit beam used was ~ 0.94 mm, which would require the distance moved between pulses to be ≤ 0.82 mm. For the lowest PRF of 112 Hz and the maximum sweep speed of 5 cm/s used in this study, the distance moved would only be ~ 0.45 mm. Therefore, the signal should stay correlated for consecutive pulses at all the sweep speeds and blood velocities used in this study.

For more physiological pulsatile flow, the WF_{eff} may need to be set higher, e.g. at ~ 25 Hz, to accommodate the typical Doppler frequency obtained from the systolic motion of the wall of the CCA. This would take into account that a $\sim 10\%$ systolic dilation (Morganti et al. 2005) occurs over a timespan of about 100 ms (Holdsworth et al. 1999). Velocity estimates would thus be improved for some correspondingly higher velocities, say ~ 5 cm/s, which is the velocity close to WF_{eff} of 25 Hz.

For proof of concept, the study was performed on steady parabolic flow where there was no wall motion. However, the flow in arteries is pulsatile and causes wall motion, where radial wall motion is typically axial to the transmit beam. Each receiver beam, oriented at an angle relative to the transmit-beam axial direction, sees a component of the wall-motion velocity. A typical artery experiences a maximum radial wall velocity during the transition from end diastole to peak systole and can be estimated to be ~ 0.8 cm/s, when considering the above mentioned dilation and timespan. Theoretical calculations of the flow and wall-motion Doppler frequencies estimated using the left and right beams after directional Doppler processing at different sweep speeds are shown in Fig. 4.11. With no aperture motion, both receiver beams see the same positive Doppler signal (shown in blue) from the wall motion. It is obvious in Fig. 4.11(a) that a sufficiently low wall filter applied to retain the blood signal would also retain the wall signal, and therefore the filtering would not suffice. By translating the aperture, the Doppler frequency estimates can be shifted as shown in Fig. 4.11 (b)–(f). Due to this translation, the wall-motion Doppler frequency decreases for one beam and increases for the other (shown in magenta), introducing an asymmetry. For example, in Fig. 4.11(c), the wall-motion Doppler frequencies from the two beams translating with a sweep speed

of 2 cm/s parallel and anti-parallel to the flow, respectively, are 46 Hz and ~3 Hz. This asymmetry could allow the high-pass wall filter to eliminate the wall-motion component of the Doppler spectrum while retaining the blood-flow component of one of the beams (the left beam in this example). However, this would change the method from 2D vector estimation to only 1D as only one out of the two receiver beams provides a reliable Doppler frequency estimate in the presence of wall motion.

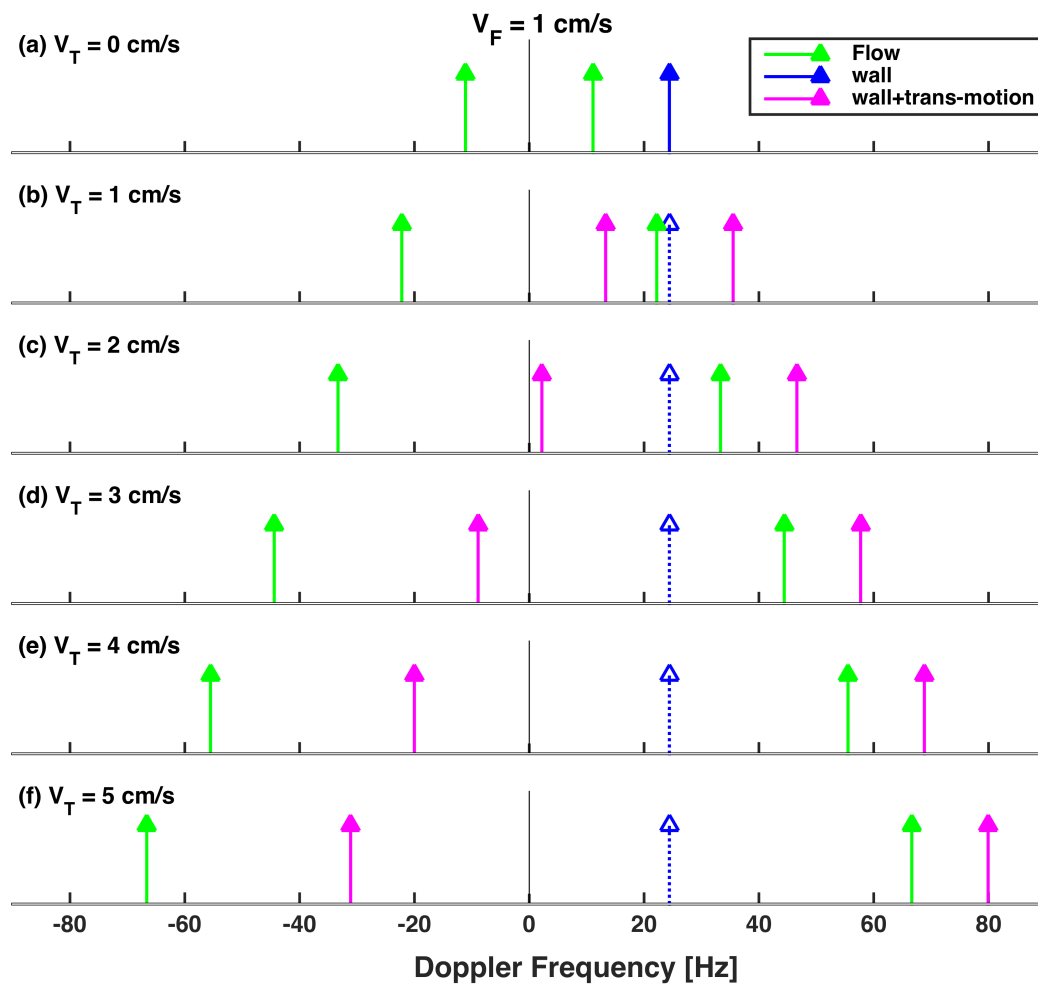


Figure 4.11: Theoretical Doppler frequencies, seen by two symmetrically oriented receiver beams at an interbeam angle of 20° for various sweep velocities (a – f), due to axial wall of 0.8 cm/s with no sweep velocity, wall velocity (perpendicular to the flow velocity) with sweep speed, and lateral flow velocity of 1 cm/s.

The results in this study were presented for a linear array parallel to the vessel-wall, but arteries generally are not straight making it difficult to align the array parallel to the vessel wall, resulting in a tilt of the array relative to the vessel and wall. The effect of this tilt on the effective wall-motion Doppler frequency was determined by calculating the change in the wall-motion Doppler frequency with respect to the tilt angle for various sweep speeds (not shown). A change of ~ 1 Hz in the Doppler frequency was obtained when the linear array was tilted through 5° . With the aperture being translated parallel to the array, any tilt would need to be compensated by acquiring the Doppler signal from progressively changing depths. This could be achieved by changing the sampling time (gate-depth) as the aperture translates such that the signal is acquired at the same depth (vessel radial position) relative to the vessel wall. Real-time variation of echo sampling times have previously been used to reduce the sampling rate required for B-mode beamforming (Foster et al. 1989; Brown and Lockwood 2005) and therefore might be readily implemented for the application presented here.

For conventional VDUS systems, three or more receiver beams should be used to make the measurements independent of the orientation of the 3D velocity vector. The technique presented here was shown to work with two receivers on a linear array, which may be reduced to only one when there is wall motion. The array must be aligned with the velocity vector, or with the wall assuming flow very close to the wall of the vessel is parallel, and would rely on the abilities of a sonographer for accurate alignment. Multiple orientations of the linear array, rotated about the transmit axis (azimuthal orientations), could be used to allow for a selection of receivers that best aligned with the velocity vector.

As demonstrated in the results section, the aperture-translation method is useful for more accurately measuring low blood velocities. Two examples of clinically relevant applications with interest in very low velocities, such as for accurate measurement of wall shear stress, are in the carotid artery and in arteriovenous fistulae (AVF). Studies have shown the significance of diastolic wall shear stress in the carotid artery for cerebral disease assessment (Palm-Meinders et al. 2009; Mutsaerts et al. 2011) and for stroke risk (Jeong et al. 2014). During the diastolic phase of the cardiac cycle, the wall velocity is very low, which eliminates the need of a higher cutoff frequency for the wall filter. A high-pass filter with a lower cutoff frequency (used in this study) would be sufficient to reduce the clutter originating from the side-lobe reverberations from surrounding tissue making the results from this study applicable when measuring shear stress during the diastolic phase.

The second application could be the accurate mapping of blood velocities and shear stress measurements in an AVF. An arteriovenous fistula is an abnormality where an artery and a vein join together, which can be congenital, pathological, or created surgically such as for dialysis intervention. Studies have demonstrated that an AVF is prone to atherosclerosis and thrombosis (Huijbregts et al. 2008; Basile et al. 2016), requiring periodic evaluation of the vascular access (fistula) through testing, such as flow measurements to detect any dysfunction (Hayashi et al. 2006; Valliant and McComb 2015). The surgical fistula for hemodialysis is created in the forearm and could easily be imaged with a probe using either M-sweep or E-sweep methods, thus providing potentially useful information on velocity and shear stress to diagnose dysfunction in the AVF.

4.4.1 Practical Limitations of VDUS Aperture Translation

The M-sweep version of the aperture-translation method is limited by the physical space available to move the transducer parallel to the vessel(s) of interest and could be difficult to align with the vessel wall. On the other hand, it would allow more flexibility in terms of choosing a broader range of sweep speeds while keeping a constant PRF, as demonstrated in the results.

Conversely, E-sweep does not require physical motion and therefore would be easier to align the direction of the aperture motion with the vessel wall by using a B-mode image. However, the E-sweep method is limited due to the dependence of the sweep speed on the PRF, as already explained. Unfortunately, hardware limitations of the scanner used in this study only allowed for a maximum of ~600 pulses to be saved at a time. With this limitation, a maximum of 6 pulses per aperture location were possible per 100 aperture-steps, yielding a minimum velocity of 3.5 cm/s at a PRF of 112 Hz. Reducing the PRF in order to lower the sweep speed then caused aliasing at even a very low flow velocity of 2 cm/s, as seen in the cases for E3.5 and E4 (Fig. 4.10).

To change the E-sweep speed for a given constant PRF would then require a change in the element-pitch of the array, which corresponds to the distance moved by the aperture between two consecutive pulses for this method. The transducer used in this study had an element-pitch of 0.3 mm, which produced a sweep speed of ~10 cm/s at a PRF of 223 Hz. For a sweep speed of 5 cm/s, i.e. reducing the sweep speed by half, the PRF had to be lowered by a factor of two. Furthermore, if a transducer with a smaller element-pitch is used, e.g. an element-pitch of 0.15 mm, the sweep speed could then be reduced to half its original at the same PRF. This means that various transducers, each

with a different element-pitch would be required for different sweep speeds. However, the M-sweep results (Fig. 4.5) suggest that at a PRF of 223 Hz a sweep speed of 2 cm/s performs best. A 2 cm/s E-sweep at the same PRF would require a transducer with an element-pitch of ~ 0.09 mm. A compromise could be made by changing the PRF to 200 Hz, resulting in a transducer with an element-pitch of 0.1 mm, which is approximately the element-pitch of current 15 MHz arrays. Arrays used with frequencies ≥ 15 MHz already exist and implement finer element-pitch arrays. The drawback of such a finer pitch array would be a reduced lateral field of view (FOV). If there is a need to increase the FOV, extra elements would need to be added.

In summary, both the mechanical (M-sweep) and the electronic (E-sweep) versions of the aperture-translation VDUS method out-performed the conventional method. Overall, M2 showed the best accuracy and reliability, suggesting the importance of making a reasonable choice of sweep speed with an optimal PRF. The electronic version of the technique, which would be more relevant clinically, performed better than M-sweep, which is an approximation of an ideal implementation of aperture translation. Therefore, the E-sweep version shows promise for further development and could be implemented with no extra hardware or modification as it uses the same type of image sequencing used for B-mode linear array scanning on almost all ultrasound scanners available in the market.

Chapter 5

5 Summary, Conclusion, and Future Directions

This chapter summarizes the work presented in this thesis and some suggestions for future work. The first section 5.1 presents the summary of the studies and the conclusions drawn from them. Section 5.2 suggests possible future directions of the work.

5.1 Summary and Conclusion

5.1.1 Crossbeam Multi-Receiver Configurations

This study provided a comparison of the accuracy of the low velocity estimates (magnitude and direction) derived using a varying number of receiver beams and assessing sensitivity to velocity orientation. The aim was to explicitly assess the benefit of increasing the number of beams while using a reasonable inter-beam angle and choice of beam selection method in order to achieve more accurate and reliable estimation of 3D velocities. Accurate estimation of these low velocities is important for accurate mapping of velocities to achieve improved estimations of wall shear stress and turbulence, which are known risk factors for atherosclerosis and stroke. In this work, as an initial assessment of the potential of multi-receiver configurations for 3D velocity estimations; a theoretical geometric analysis was performed using 3R – 8R configurations at various inter-beam angles for a range of velocity-vector orientations with a magnitude such that its Doppler shift lies near the wall filter cut-off. The experimental analysis used a steady parabolic flow data, which generated flow velocity magnitudes spanning up to 5 cm/s, such as might typically occur within a few millimeters of the wall of a common carotid artery or other large vessels. Flow was imaged using a linear array, and vector Doppler

signal processing. The linear array was rotated about the central transmit-beam axis to generate various crossed receiver-beam configurations and to emulate different velocity-vector orientations. Some beam-selection criteria were examined to assess their affect on the accuracy of the resultant velocity vector estimation.

Overall, this study provided guidance in choosing the best configuration and geometric parameters for VDUS applications where low velocities were needed to be measured, e.g. for wall shear stress estimates, and also for designing a 2D array for such applications. The results demonstrated both theoretically and experimentally that accurate and reliable estimations of low 3D vector velocities require greater than four receiver-beams with a minimum inter-beam angle of 20° for each of the beam selection methods tested in this study. The asymmetry in the arrangement of receivers, as seen with a 5R configuration, was observed to be an important factor in improving the velocity vector estimations. Hence, a minimum of five receivers was suggested when designing a 2D array or probe for velocities near the wall filter cut-off.

5.1.2 Vector Doppler Ultrasound Aperture-Translation

The aim of this study was to also accurately estimate blood velocities as close as possible to the wall with the same motivation as mentioned above i.e. to improve the estimation of wall shear stress in large arteries. A novel technique – aperture-translation – was introduced for this purpose. The low near-wall velocities, when measured with the conventional VDUS system would give highly unreliable estimates, which are due to the reduced SNR of the Doppler signal. The aperture-translation method improved the SNR for these velocities by increasing the phase difference via two versions of the technique, translating the transmit- and receive-apertures mechanically and electronically. These two

versions, M-sweep and E-sweep, were assessed for velocity accuracy compared to the conventional method, imaging the velocities in a wall-less straight-vessel phantom under steady flow conditions. Performance of the M-sweep method was also assessed at various sweep speeds and ensemble sizes at two inter-beam angles and for a range of flow velocities (0 to 3 cm/s). The M-sweep and E-sweep methods were compared to assess if the two versions were equivalent.

The results from this work demonstrated that the aperture-translation VDUS method, both its mechanical and electronic version, improved the accuracy and precision of low near-wall velocities that lied within the WF_{eff} compared to the conventional method. However, a reasonable choice of sweep speed and an optimal PRF would be important. The equivalence in the performance of the two versions with E-sweep performing similarly or better than M-sweep suggested the E-sweep method, which would be more suitable for clinical implementation, showed promise for further study.

5.2 Future Directions

5.2.1 2D Array Design of a 5R configuration

The results from Chapter 3 suggested a 2D array design with 5R configuration, for best accuracy and precision of low 3D vector velocities that lie near the wall filter cut-off, without introducing redundancy in terms of number of receivers. As discussed in Chapter 3, for a 2D array with 5R configuration design, a large number of elements would need to be wired (1920, with each aperture using 320 elements, as described in Section 3.4). This is a well-known limitation that makes the implementation of 2D arrays a very challenging task, i.e. requiring a large amount of hardware and computing power. To overcome this

challenge, techniques such as Mills cross arrays, vernier arrays, and random 2D arrays have been implemented (Davidsen et al. 1994; Brunke and Lockwood 1997; Yen and Smith 2004). These methods deteriorate the imaging capability and the Doppler signal strength. Various optimization algorithms like simulated annealing and genetic algorithms (Trucco 1999; Weber et al. 1999; Chen et al. 2010) have been introduced that try to improve the beam-quality by minimizing the side-lobes and the grating-lobes while maintaining a constant width of the main-lobe.

In future work, a simulation study using Field-II, an open-ware MATLAB-based ultrasound simulation program (Jensen and Svendsen 1992; Jensen 1996b) (<http://field-ii.dk>), could be performed for the design of a 2D array to implement a 5R configuration. The study might include simulation of an optimization algorithm, for example using a genetic or simulated annealing algorithm. A recent work (Diarra et al. 2012) demonstrated that a reduction in the number of elements by ~82% resulted in a good quality image using the simulated annealing sparse array technique. A similar algorithm could be adopted to assess each receiver-beam's Doppler SNR with the limited number of elements. Besides optimization of number of elements of the array, it would also be useful to study the effect of aperture size and considerations that would be difficult to study experimentally, such as sample volume misregistration and differences in attenuation along different receive beams.

5.2.2 Optimized Beam-Selection Method

The work in chapter 3 also showed a preliminary study on assessing the potential of a few beam-selection methods on the accuracy of 3D velocity estimations. The results of the study suggested overall good performance of PT method but requires a user-defined

threshold. A comprehensive simulation study on the beam-selection methods would be useful for finding a more robust beam-selection criterion with an objective of making it user-independent. This could include a combination of WLS and PT method to improve the accuracy and reliability of velocity estimation using a 3D VDUS system, potentially a 5R configuration. A possible way would be to apply the PT method first, to eliminate the obviously low SNR Doppler shifts and then apply the WLS method to the remaining beams. With the combined approach, the PT method would satisfactorily remove any obviously noisy estimates even if the user-defined threshold value was sub-optimal. A combination of other methods, such as MDSD and maximum power (selecting three beams with maximum Doppler power), along with the PT method could also be studied for optimization. This would potentially contribute in improving the overall accuracy of the low SNR Doppler signals that lie near and within the WF_{eff} .

5.2.3 Implementation of Optimized 2D array for *In-vitro* and *In-vivo* Assessment

The next step might be to implement the optimized 2D array. Fully wired 2D arrays are available in the market. These could be custom sampled to match the 5R design, controlled by software to form a sparse array. The velocities in regions such as in recirculation in the sinus bulb of the ICA and near the wall could be estimated to obtain velocity maps using the existing PVA carotid flow phantom (stenosis severity of 50% eccentrically oriented) initially using constant flow conditions. A steady state condition would be useful for line-by-line acquisition to obtain velocity maps in the vessel. The particle image velocimetry (PIV) technique could be used to compare and validate the accuracy of the estimated velocities in the proposed 2D array design. Particle image

velocimetry is considered the gold standard laboratory technique for fluid flow characterization and is already set up in our laboratory. Shear stress measurements could then be made and compared with the PIV shear stress measurements. The validation could then extend to a physiologically realistic flow condition, i.e. pulsatile flow, which could be achieved by applying a carotid flow-rate waveform to the carotid flow phantom using a programmable flow pump (Holdsworth et al. 1991). A trigger signal could be set up on the waveform to acquire data at the same phase of the cardiac cycle in order to generate an ensemble data set from multiple cardiac cycles.

An *in-vivo* study could be performed to estimate near wall velocities in the CCA, where the flow is mostly parabolic, as well as in the ICA bulb, where the flow is recirculating. The ethical approval for such a system should not be any different, as the increased number of receivers would not increase the amount of energy delivered to the body. The probe would use only one transmit-beam, which would be similar to any other clinically used probes. Velocity estimations close to the vessel wall, both during the peak systole and the diastolic phase of the cardiac cycle, could be made and the wall shear stress could also be calculated from these velocity estimations. The results could then be compared with that of PIV or computational fluid dynamics using patient-specific geometric models. The images for these geometries could be obtained from MRI. The trade-offs are that PIV validation would require phantom fabrication with optically transparent TMM, such as polydimethylsiloxane, for each individual geometry, which could be costly. On the other hand, computational fluid dynamics assumes rigid wall conditions, which would not be a physiologically realistic assumption. Hence, trade-offs would need to be assessed before making the choice.

The *in-vivo* study would be useful in more accurately determining the wall shear stress because the 5R configuration design of the probe would allow accurate velocity estimations closer to the wall than it would be possible with only 3R configuration. As already mentioned in the introduction chapter, wall shear stress is an important hemodynamic parameter for vascular disease diagnosis.

5.2.4 Optimization of VDUS Aperture-Translation Technique

The potential and proof of concept of a novel technique, for accurate estimation of low blood velocities within the wall filter cut-off, was introduced in Chapter 4. The results showed improvement of low velocities ≤ 2 cm/s for this method compared to the conventional VDUS method with the electronic aperture-translation method showing improved precision with similar accuracy when compared with its mechanical version. Due to the hardware limitation and dependence of PRF on the sweep speed, for a given pitch of the linear array, only a limited range of velocities were possible, which limited the analysis to only few sweep speeds.

In the future, this analysis could be advanced by a simulation study, which would easily allow for changing the element-pitch of the array to keep the PRF constant when changing the sweep speed, instead of switching linear arrays to change the element-pitch. The effect of the range of varying beam-orientations, PRFs, and ensemble sizes for varying sweep speeds could be studied to optimize these parameters imaging a range of low velocities

As discussed in Chapter 4, the aperture-translation method requires accurate alignment of the linear array along the wall of the vessel in the elevation direction,

however, the sensitivity of the technique on the velocity vector orientation should be studied by simulating the bends and twists as seen in the human vasculature. The next step could be to experimentally demonstrate the potential of the method suggested for obtaining information from varying depths (Discussion: section 4.4) when the aperture translation is not parallel to the vessel axis (i.e. presumed flow direction). The experiment could be performed in a straight-vessel phantom using constant flow but tilting the transducer to move the aperture at an angle relative to the vessel. The method of varying the sampling rate to obtain signal from varying depths was previously introduced by Foster *et al.* (Foster et al. 1989) for B-mode beamforming and it would be useful to study its effect on the aperture-translation technique.

5.2.5 Reducing Effect of Wall Motion on VDUS Aperture-Translation

As discussed in Chapter 4 the wall motion affect the aperture-translation method both favorably and adversely, as shown in Fig. 4.11, reducing the 2D system to 1D. As suggested, multiple orientations of the linear array, rotated about the transmit axis (azimuthal orientations), would allow for a selection of receivers that best align with the velocity vector. An experimental study could be performed in the existing straight-vessel phantom adding vessel-wall motion. The motion could be a sinusoidal flow motion, axial to the transmit beam, generated using a programmable flow pump. The potential of the method of selecting multiple receivers for the accuracy and reliability of 2D velocity estimates could be assessed for various wall velocities, corresponding to different phases of the cardiac cycle, and varying sweep speeds.

The final verification of the technique would be an *in-vivo* study performed on normal healthy common carotid arteries during systolic and diastolic phases to measure

the wall velocities and the wall shear stresses. The application of the method would not be limited to only carotid flow but would also be useful for diagnosing abnormal flow and for improved estimations of wall shear stress, such as, in the arteriovenous fistula.

Overall, the future work suggested here would be very useful in overcoming the major limitations of DUS, the angle-dependence, and the adverse effect of the high-pass filter. This would provide more accurate estimation of low and 3D blood velocities, improved measurements of wall shear stress, and accurate mapping of abnormal hemodynamics in a diseased vasculature. Implementation of the optimized 2D-array design and the aperture-translation techniques would provide a useful tool for improved diagnosis and management of vascular disease.

Bibliography

Asakura T, Karino T. Flow patterns and spatial-distribution of atherosclerotic lesions in human coronary-arteries. *Circ Res* 1990; 66:1045-66.

Ashrafzadeh AC, J.Y, Dormer, K.J. Analysis of velocity estimation error for a multidimensional Doppler ultrasound system. *IEEE Transactions on Ultrasonics Ferroelectrics and Frequency Control* 1988; 35:536-44.

Back MR, Wilson JS, Rushing G, Stordahl N, Linden C, Johnson BL, Bandyk DF. Magnetic resonance angiography is an accurate imaging adjunct to duplex ultrasound scan in patient selection for carotid endarterectomy. *J Vasc Surg* 2000; 32:429-38.

Bakker P. Bifurcations in flow patterns: Some applications of the qualitative theory of differential equations in fluid dynamics. New York: Springer, 1991.

Basile C, Vernaglione L, Casucci F, Libutti P, Lisi P, Rossi L, et al. The impact of haemodialysis arteriovenous fistula on haemodynamic parameters of the cardiovascular system. *Clinical Kidney Journal* 2016; 9:729-34.

Bastos CAC, Fish PJ, Vaz F. Spectrum of Doppler ultrasound signals from nonstationary blood flow. *IEEE Transactions on Ultrasonics Ferroelectrics and Frequency Control* 1999; 46:1201-17.

Bercoff J, Montaldo G, Loupas T, Savery D, Meziere F, Fink M, Tanter M. Ultrafast compound Doppler imaging: Providing full blood flow characterization. *IEEE Transactions on Ultrasonics Ferroelectrics and Frequency Control* 2011; 58:134-47.

Bjaerum S, Torp H, Kirstoffersen K. Clutter filter design for ultrasound color flow imaging. *IEEE Transactions on Ultrasonics Ferroelectrics and Frequency Control* 2002; 49:204-16.

Bohs LN, Gebhart SC, Anderson ME, Geiman BJ, Trahey GE. 2-d motion estimation using two parallel receive beams. *IEEE Transactions on Ultrasonics Ferroelectrics and Frequency Control* 2001; 48:392-408.

Bohs LN, Geiman BJ, Anderson ME, Breit SM, Trahey GE. Ensemble tracking for 2D vector velocity measurement: Experimental and initial clinical results. *IEEE Transactions on Ultrasonics Ferroelectrics and Frequency Control* 1998; 45:912-24.

Bohs LN, Trahey GE. A novel method for angle independent ultrasonic-imaging of blood-flow and tissue motion. *IEEE Trans Biomed Eng* 1991; 38:280-6.

- Brinjikji W, Huston J, Rabinstein AA, Kim GM, Lerman A, Lanzino G. Contemporary carotid imaging: From degree of stenosis to plaque vulnerability. *J Neurosurg* 2016; 124:27-42.
- Brott TG, Halperin JL, Abbara S, Bacharach JM, Barr JD, Bush RL, Cates CU, et al. Amer Acad N, Soc Cardiovasc Comput Tomogr 2011 ASA/ACCF/AHA/AANN/AANS/ACR/ASNR/CNS/SAIP/SCAI/SIR/SNIS/SVM/SVS guideline on the management of patients with extracranial carotid and vertebral artery disease: Executive summary. *Catheter Cardiovasc Interv* 2013; 81:E75-E123.
- Brown JA, Lockwood GR. A digital beamformer for high-frequency annular arrays. *IEEE Transactions on Ultrasonics Ferroelectrics and Frequency Control* 2005; 52:1262-9.
- Brunke SS, Lockwood GR. Broad-bandwidth radiation patterns of sparse two-dimensional vernier arrays. *IEEE Transactions on Ultrasonics Ferroelectrics and Frequency Control* 1997; 44:1101-9.
- Bryant DJ, Payne JA, Firmin DN, Longmore DB. Measurement of flow with NMR imaging using a gradient pulse and phase difference technique. *J Comput Assist Tomogr* 1984; 8:588-93.
- Calzolari M, Capineri L, Fort A, Masotti L, Rocchi S, Scabia M. A 3-D PW ultrasonic Doppler flowmeter: Theory and experimental characterization. *IEEE Transactions on Ultrasonics Ferroelectrics and Frequency Control* 1999; 46:108-13.
- Cardoso JCS, Ruano MG, Fish PJ. Nonstationarity broadening reduction in pulsed Doppler spectrum measurements using time-frequency estimators. *IEEE Trans Biomed Eng* 1996; 43:1176-86.
- Censor D, Newhouse VL, Vontz T, Ortega HV. Theory of ultrasound Doppler-spectra velocimetry for arbitrary beam and flow configurations. *IEEE Trans Biomed Eng* 1988; 35:740-51.
- Chalela JA. Evaluating the carotid plaque: Going beyond stenosis. *Cerebrovasc Dis* 2009; 27:19-24.
- Chen P, Shen BJ, Zhou LS, Chen YW. Optimized simulated annealing algorithm for thinning and weighting large planar arrays. *Journal of Zhejiang University-Science C-Computers & Electronics* 2010; 11:261-9.
- Chen ZM, Sandercock P, Pan HC, Counsell C, Collins R, Liu LS, Xie JX, Warlow C, Peto R, Cast, ISTC Groups. Indications for early aspirin use in acute ischemic stroke - A combined analysis of 40,000 randomized patients from the chinese acute stroke trial and the international stroke trial. *Stroke* 2000; 31:1240-9.
- Cheung CCP, Yu ACH, Salimi N, Yiu BYS, Tsang IKH, Kerby B, et al. Multi-channel pre-beamformed data acquisition system for research on advanced ultrasound imaging

methods. IEEE Transactions on Ultrasonics Ferroelectrics and Frequency Control 2012; 59:243-53.

Cicha I, Worner A, Urschel K, Beronov K, Goppelt-Struebe M, Verhoeven E, et al. Carotid plaque vulnerability a positive feedback between hemodynamic and biochemical mechanisms. Stroke 2011; 42:3502-U268.

Cloutier G, Qin Z, Durand LG, Teh BG. Power Doppler ultrasound evaluation of the shear rate and shear stress dependences of red blood cell aggregation. IEEE Trans Biomed Eng 1996; 43:441-50.

Cumming G, Fidler F, Vaux DL. Error bars in experimental biology. J Cell Biol 2007; 177:7-11.

Davidson RE, Jensen JA, Smith SW. 2-dimensional random arrays for real-time volumetric imaging. Ultrason Imaging 1994; 16:143-63.

Davies JE, Whinnett ZI, Francis DP, Willson K, Foale RA, Malik IS, et al. Use of simultaneous pressure and velocity measurements to estimate arterial wave speed at a single site in humans. Am J Physiol-Heart Circul Physiol 2006; 290:H878-H85.

Dawson DL, Roseberry CA, Fujitani RM. Preoperative testing before carotid endarterectomy: A survey of vascular surgeons' attitudes. Ann Vasc Surg 1997 ;11:264-72.

Diarra B, Liebgott H, Robini M, Tortoli P, Cachard C. Optimized 2D array design for ultrasound imaging. Proceedings of the 20th European Signal Processing Conference, Bucharest, Romania 2012. pp. 2718-22.

Dirksen MT, Van der Wal AC, Van den Berg FM, Van der Loos CM, Becker AE. Distribution of inflammatory cells in atherosclerotic plaques relates to the direction of flow. Circulation 1998; 98:2000-3.

Dunmire B, Beach KW, Labs KH, Plett M, Strandness DE. Cross-beam vector Doppler ultrasound for angle-independent velocity measurements. Ultrasound Med Biol 2000; 26:1213-35.

Dunmire B, Pagel G, Beach KW, Labs KH. Post stenotic flow disturbances in a steady flow model. Proceedings of SPIE Medical Imaging 2001: Ultrasonic Imaging and Signal Processing, SanDiego, CA 2001. pp. 502-13.

Dyverfeldt P, Kvitting JPE, Sigfridsson A, Engvall J, Bolger AF, Ebbers T. Assessment of fluctuating velocities in disturbed cardiovascular blood flow: In vivo feasibility of generalized phase-contrast MRI. J Magn Reson Imaging 2008; 28:655-63.

Dyverfeldt P, Sigfridsson A, Kvitting JPE, Ebbers T. Quantification of intra-voxel velocity standard deviation and turbulence intensity by generalizing phase-contrast MRI. Magn Reson Med 2006; 56:850-8.

ECST. MRC European Carotid Surgery Trial: Interim results for symptomatic patients with severe (70–99%) or with mild (0–29%) carotid stenosis. *Lancet* 1991; 337:1235-43.

Ekroll IK, Swillens A, Segers P, Dahl T, Torp H, Lovstakken L. Simultaneous quantification of flow and tissue velocities based on multi-angle plane wave imaging. *IEEE Transactions on Ultrasonics Ferroelectrics and Frequency Control* 2013; 60:727-38.

Evans DH, Jensen JA, Nielsen MB. Ultrasonic colour Doppler imaging. *Interface Focus* 2011; 1:490-502.

Evans DHM, W. N. Doppler ultrasound: Physics, Instrumentation and Signal Processing. West Sussex, UK: John Wiley & Sons, Ltd, 2000.

Fadnes S, Ekroll IK, Nyrnes SA, Torp H, Lovstakken L. Robust angle-independent blood velocity estimation based on dual-angle plane wave imaging. *IEEE Transactions on Ultrasonics Ferroelectrics and Frequency Control* 2015; 62:1757-67.

Fahrbach K. Ein beitrage zur blutgeschwindigkeitsmessung unter anwendung des Dopplereffektes. *Electromedizin* 1970; 15:26-31.

Fayed AM, White CJ, Ramee SR, Jenkins JS, Collins TJ. Carotid and cerebral angiography performed by cardiologists: Cerebrovascular complications. *Catheter Cardiovasc Interv* 2002; 55:277-80.

Feigin VL, Forouzanfar MH, Krishnamurthi R. Global and regional burden of stroke during 1990-2010: Findings from the global burden of disease study 2010 (vol 383, pg 245, 2014). *Lancet* 2014; 383:218.

Fish PJ. Nonstationarity broadening in pulsed Doppler spectrum measurements. *Ultrasound Med Biol* 1991; 17:147-55.

Flynn J, Daigle R, Pflugrath L, Linkhart K, Kaczowski P. Estimation and display for vector Doppler imaging using planewave transmissions. 2011 IEEE International Ultrasonics Symposium (IUS) 2012; pp. 413-8.

Ford MD, Xie YYJ, Wasserman BA, Steinman DA. Is flow in the common carotid artery fully developed? *Physiol Meas* 2008; 29:1335-49.

Forsberg F, Stein AD, Merton DA, Lipcan KJ, Herzog D, Parker L, Needleman L. Carotid stenosis assessed with a 4-dimensional semiautomated Doppler system. *J Ultrasound Med* 2008; 27:1337-44.

Foster FS, Larson JD, Pittaro RJ, Corl PD, Greenstein AP, Lum PK. A digital annular array prototype scanner for realtime ultrasound imaging. *Ultrasound Med Biol* 1989; 15:661-72.

Fox AJ. How to measure carotid stenosis. *Radiology* 1993; 186:316-8.

Fox MD. Multiple crossed-beam ultrasound Doppler velocimetry. *IEEE Transactions on Sonics and Ultrasonics* 1978; 25:281-6.

Fox MD, Gardiner WM. 3-dimensional Doppler velocimetry of flow jets. *IEEE Trans Biomed Eng* 1988; 35:834-41.

Frydrychowicz A, Harloff A, Jung B, Zaitsev M, Weigang E, Bley TA, et al. Time-resolved, 3-dimensional magnetic resonance flow analysis at 3T: Visualization of normal and pathological aortic vascular hemodynamics. *J Comput Assist Tomogr* 2007; 31:9-15.

Fung Y. *Biomechanics: Circulation*. New York: Springer, 1997.

Ganger R. *Fluid mechanics*. New York: Dover, 1995.

Glagov S, Zarins C, Giddens DP, Ku DN. Hemodynamics and atherosclerosis - insights and perspectives gained from studies of human arteries. *Arch Pathol Lab Med* 1988; 112:1018-31.

Gokaldas R, Singh M, Lal S, Benenstein RJ, Sahni R. W carotid stenosis: From diagnosis to management, where do we stand? *Curr Atheroscler Rep* 2015; 17:1

Gorelick PB. Stroke prevention - An opportunity for efficient utilization of health-care resources during the coming decade. *Stroke* 1994; 25:220-4.

Guidi G, Licciardello C, Falteri S. Intrinsic spectral broadening (ISB) in ultrasound Doppler as a combination of transit time and local geometrical broadening. *Ultrasound Med Biol* 2000; 26:853-62.

Gupta A, Marshall RS. Moving beyond luminal stenosis: Imaging strategies for stroke prevention in asymptomatic carotid stenosis. *Cerebrovasc Dis* 2015; 39:253-61.

Ha H, Kim GB, Kweon J, Lee SJ, Kim YH, Lee DH, Yang DH, Kim N. Hemodynamic measurement using four-dimensional phase-contrast MRI: Quantification of hemodynamic parameters and clinical applications. *Korean J Radiol* 2016; 17:445-62.

Hansen HHG, Saris A, Vaka NR, Nillesen MM, de Korte CL. Ultrafast vascular strain compounding using plane wave transmission. *J Biomech* 2014a; 47:815-23.

Hansen KL, Udesen J, Gran F, Jensen JA, Nielsen MB, IEEE. Fast blood vector velocity imaging using ultrasound: In-vivo examples of complex blood flow in the vascular system. *Proceedings of IEEE International Ultrasonics Symposium*, vols 1-4 and appendix, Beijing, China 2008. pp. 1068-71.

Hansen KL, Udesen J, Oddershede N, Henze L, Thomsen C, Jensen JA, Nielsen MB. In vivo comparison of three ultrasound vector velocity techniques to MR phase contrast angiography. *Ultrasonics* 2009a; 49:659-67.

Hansen KL, Udesen J, Thomsen C, Jensen JA, Nielsen MB. In vivo validation of a blood vector velocity estimator with MR angiography. *IEEE Transactions on Ultrasonics Ferroelectrics and Frequency Control* 2009b; 56:91-100.

Hansen PM, Olesen JB, Pihl MJ, Lange T, Heerwagen S, Pedersen MM, et al. Volume flow in arteriovenous fistulas using vector velocity ultrasound. *Ultrasound Med Biol* 2014b; 40:2707-14.

Hansen PM, Pedersen MM, Hansen KL, Nielsen MB, Jensen JA. Examples of vector velocity imaging. In: Dremstrup K, Rees S, Jensen O. 15th Nordic-Baltic Conference on Biomedical Engineering and Medical Physics, 2011. pp. 77-80.

Hayashi R, Huang E, Nissenson AR. Vascular access for hemodialysis. *Nature Clinical Practice Nephrology* 2006; 2:504-13.

Hoeks APG, Hennerici M, Reneman RS. Spectral composition of Doppler signals. *Ultrasound Med Biol* 1991; 17:751-60.

Holdsworth DW, Norley CJD, Frayne R, Steinman DA, Rutt BK. Characterization of common carotid artery blood-flow waveforms in normal human subjects. *Physiol Meas* 1999; 20:219-40.

Holdsworth DW, Rickey DW, Drangova M, Miller DJM, Fenster A. Computer-controlled positive displacement pump for physiological flow simulation. *Med Biol Eng Comput* 1991; 29:565-70.

Holme PA, Orvim U, Hamers M, Solum NO, Brosstad FR, Barstad RM, Sakariassen KS. Shear-induced platelet activation and platelet microparticle formation at blood flow conditions as in arteries with a severe stenosis. *Arterioscler Thromb Vasc Biol* 1997; 17:646-53.

Hoskins PR, Kenwright DA. Recent developments in vascular ultrasound technology. *Ultrasound* 2015; 23:158-65.

Huibers A, de Borst GJ, Wan S, Kennedy F, Giannopoulos A, Moll FL, Richards T. Non-invasive carotid artery imaging to identify the vulnerable plaque: Current status and future goals. *Eur J Vasc Endovasc Surg* 2015; 50:563-72.

Huijbregts HJT, Bots ML, Wittens CHA, Schrama YC, Moll FL, Blankestijn PJ, CIMINO Study Group. Hemodialysis arteriovenous fistula patency revisited: Results of a prospective, multicenter initiative. *Clin J Am Soc Nephrol* 2008; 3:714-9.

Hussain B, Wong EY, Yiu BYS, Yu ACH, and Poepping TL. Evaluation of cross-beam vector Doppler ultrasound systems for accurate 3-D velocity measurements. *Proceedings of IEEE International Ultrasonics Symposium, Dresden, Germany 2012*, pp. 326-29.

Hutchison KJ. Doppler ultrasound spectral shape downstream of significant arterial-stenosis in-vivo. *Ultrasound Med Biol* 1995; 21:447-58.

Hutchison KJ, Karpinski E. In vivo demonstration of flow recirculation and turbulence downstream of graded stenoses in canine arteries. *J Biomech* 1985;18:285-96.

Jensen JA. Estimation of blood velocities using ultrasound: A signal processing approach. New York, NY, USA: Cambridge University Press, 1996a.

Jensen JA. A new estimator for vector velocity estimation. *IEEE Transactions on Ultrasonics Ferroelectrics and Frequency Control* 2001; 48:886-94.

Jensen JA, Munk P. A new method for estimation of velocity vectors. *IEEE Transactions on Ultrasonics Ferroelectrics and Frequency Control* 1998; 45:837-51.

Jensen JA, Nikolov SI, Udesen J, Munk P, Hansen KL, Pedersen MM, et al. Recent advances in blood flow vector velocity imaging. *Proceedings of IEEE International Ultrasonics Symposium, Orlando, FL 2011*, pp. 262-71.

Jensen JA, Nikolov SI, Yu ACH, Garcia D. Ultrasound vector flow imaging-part I: Sequential systems. *IEEE Transactions on Ultrasonics Ferroelectrics and Frequency Control* 2016a; 63:1704-21.

Jensen JA, Nikolov SI, Yu ACH, Garcia D. Ultrasound vector flow imaging-part II: Parallel systems. *IEEE Transactions on Ultrasonics Ferroelectrics and Frequency Control* 2016b; 63:1722-32.

Jensen JA, Pihl MJ, Olesen JB, Hansen PM, Hansen KL, Nielsen MB. New developments in vector velocity imaging using the transverse oscillation approach. *Proceedings of SPIE 8675 Medical imaging 2013: Ultrasonic imaging, Tomography, and Therapy, Orlando, FL 2013*, 86750F.

Jensen JA, Svendsen NB. Calculation of pressure fields from arbitrarily shaped, apodized, and excited ultrasound transducers. *IEEE Transactions on Ultrasonics Ferroelectrics and Frequency Control* 1992; 39:262-7.

Jeong SK, Lee JY, Rosenson RS. Association between ischemic stroke and vascular shear stress in the carotid artery. *Journal of Clinical Neurology* 2014; 10:133-9.

Karabiyik Y, Ekroll IK, Eik-Nes SH, Avdal J, Lovstakken L. Adaptive spectral estimation methods in color flow imaging. *IEEE Transactions on Ultrasonics Ferroelectrics and Frequency Control* 2016; 63:1839-51.

Kasai C, Namekawa K, Koyano A, Omoto R. Real-time two-dimensional blood-flow imaging using an autocorrelation technique. *IEEE Transactions on Sonics and Ultrasonics* 1985; 32:458-64.

Kefayati S, Holdsworth DW, Poepping TL. Turbulence intensity measurements using particle image velocimetry in diseased carotid artery models: Effect of stenosis severity, plaque eccentricity, and ulceration. *J Biomech* 2014; 47:253-63.

King DM, Moran CM, McNamara JD, Fagan AJ, Browne JE. Development of a vessel-mimicking material for use in anatomically realistic Doppler flow phantoms. *Ultrasound Med Biol* 2011; 37:813-26.

Kokkalis E, Cookson AN, Stonebridge PA, Corner GA, Houston JG, Hoskins PR. Comparison of vortical structures induced by arteriovenous grafts using vector Doppler ultrasound. *Ultrasound Med Biol* 2015; 41:760-74.

Kokkalis E, Hoskins PR, Corner GA, Stonebridge PA, Doull AJ, Houston JG. Secondary flow in peripheral vascular prosthetic grafts using vector Doppler imaging. *Ultrasound Med Biol* 2013; 39:2295-307.

Ku DN, Giddens DP, Phillips DJ, Strandness DE. Hemodynamics of the normal human carotid bifurcation - invitro and invivo studies. *Ultrasound Med Biol* 1985; 11:13-26.

Kwak BR, Back M, Bochaton-Piallat ML, Caligiuri G, Daemens M, Davies PF, et. al. Biomechanical factors in atherosclerosis: Mechanisms and clinical implications. *Eur Heart J* 2014; 35:3013-20.

Leguy CAD, Bosboom EMH, Hoeks APG, van de Vosse FN. Model-based assessment of dynamic arterial blood volume flow from ultrasound measurements. *Med Biol Eng Comput* 2009; 47:641-8.

Lenge M, Ramalli A, Boni E, Liebgott H, Cachard C, Tortoli P. High-frame-rate 2-D vector blood flow imaging in the frequency domain. *IEEE Transactions on Ultrasonics Ferroelectrics and Frequency Control* 2014; 61:1504-14.

Lenge M, Ramalli A, Tortoli P, Cachard C, Liebgott H. Plane-wave transverse oscillation for high-frame-rate 2-D vector flow imaging. *IEEE Transactions on Ultrasonics Ferroelectrics and Frequency Control* 2015; 62:2126-37.

Lesniak B, Kaluzynski K, Liepsch D, Palko T. The discrimination of stenosed carotid bifurcation models with smooth and irregular plaque surface. Part I. Laser and ultrasonic Doppler flow studies. *Med Eng Phys* 2002a; 24:309-18.

Lesniak B, Kaluzynski K, Liepsch D, Palko T. The discrimination of stenosed carotid bifurcation models with smooth and irregular plaque surface. Part II. The multivariate statistical analysis of ultrasonic Doppler velocity data. *Med Eng Phys* 2002b; 24:319-23.

Liu H, Liu DC. Blood flow velocity estimation from ultrasound speckle tracking using chirp signals. *Proceedings of IEEE 3rd International Conference on Bioinformatics and Biomedical Engineering, Beijing, China 2009*, pp. 1-4.

Lovstakken L, Bjaerum S, Martens D, Torp H. Blood flow imaging - a new real-time, 2-D flow imaging technique. *IEEE Transactions on Ultrasonics Ferroelectrics and Frequency Control* 2006; 53:289-99.

Lui EYL, Steinman AH, Cobbold RSC, Johnston KW. Human factors as a source of error in peak Doppler velocity measurement. *J Vasc Surg* 2005; 42:972-9.

Malek AM, Alper SL, Izumo S. Hemodynamic shear stress and its role in atherosclerosis. *Jama-Journal of the American Medical Association* 1999; 282:2035-42.

Malik V, Subramaniam A, Kapoor PM. Strain and strain rate: An emerging technology in the perioperative period. *Annals of Cardiac Anaesthesia* 2016; 19:112-21.

Manbachi A, Hoi Y, Wasserman BA, Lakatta EG, Steinman DA. On the shape of the common carotid artery with implications for blood velocity profiles. *Physiol Meas* 2011; 32:1885-97.

Markl M, Frydrychowicz A, Kozerke S, Hope M, Wieben O. 4D flow MRI. *J Magn Reson Imaging* 2012; 36:1015-36.

McArdle A, Newhouse VL. Doppler bandwidth dependence on beam to flow angle. *J Acoust Soc Am* 1996; 99:1767-78.

McArdle A, Newhouse VL, Beach KW. Demonstration of three-dimensional vector flow estimation using bandwidth and two transducers on a flow phantom. *Ultrasound Med Biol* 1995; 21:679-92.

Mendis S, Abegunde D, Yusuf S, Ebrahim S, Shaper G, Ghannem H, Shengelia B. WHO study on prevention of recurrences of myocardial infarction and stroke (WHO-premise). *Bull World Health Organ* 2005; 83:820-8.

Miller KS, Rochwarg MM. Covariance approach to spectral moment estimation. *IEEE Transactions on Information Theory* 1972; 18:588-96.

Mitchell GF, Parise H, Vita JA, Larson MG, Warner E, Keaney JF, et. al. Local shear stress and brachial artery flow-mediated dilation - the Framingham heart study. *Hypertension* 2004; 44:134-9.

Moran PR. A flow velocity zeugmatographic interlace for NMR imaging in humans. *Magn Reson Imaging* 1982; 1:197-203.

Morbiducci U, Kok AM, Kwak BR, Stone PH, Steinman DA, Wentzel JJ. Atherosclerosis at arterial bifurcations: Evidence for the role of haemodynamics and geometry. *Thromb Haemost* 2016; 115:484-92.

Morganti T, Ricci S, Vittone F, Palombo C, Tortoli P. Clinical validation of common carotid artery wall distension assessment based on multigate Doppler processing. *Ultrasound Med Biol* 2005; 31:937-45.

Morsy AA, von Ramm OT. 3D ultrasound tissue motion tracking using correlation search. *Ultrason Imaging* 1998; 20:151-9.

Mozaffarian D, Benjamin EJ, Go AS, Arnett DK, Blaha MJ, Cushman M, et. al., Amer Heart Assoc Stat Comm, Stroke Stat Subcomm. Heart Disease and Stroke Stat-2015 update: A report from the American Heart Association. *Circulation* 2015; 131:E29-E322.

Mutsaerts H, Palm-Meinders IH, de Craen AJM, Reiber JHC, Blauw GJ, van Buchem MA, et. al. Diastolic carotid artery wall shear stress is associated with cerebral infarcts and periventricular white matter lesions. *Stroke* 2011; 42:3497-501.

Mynard JP, Steinman DA. Effect of velocity profile skewing on blood velocity and volume flow waveforms derived from maximum Doppler spectral velocity. *Ultrasound Med Biol* 2013; 39:870-81.

Mynard JP, Wasserman BA, Steinman DA. Errors in the estimation of wall shear stress by maximum Doppler velocity. *Atherosclerosis* 2013; 227:259-66.

NASCET. Beneficial effect of carotid endarterectomy in symptomatic patients with high-grade carotid stenosis. *N Engl J Med* 1991; 325:445-53.

Nesbitt WS, Westein E, Tovar-Lopez FJ, Tolouei E, Mitchell A, Fu J, et al. A shear gradient-dependent platelet aggregation mechanism drives thrombus formation. *Nat Med* 2009; 15:665-U146.

Newhouse VL, Bendick PJ, Varner LW. Analysis of transit-time effects on Doppler flow measurement. *IEEE Trans Biomed Eng* 1976; 23:381-7.

Newhouse VL, Censor D, Vontz T, Cisneros JA, Goldberg BB. Ultrasound Doppler probing of flows transverse with respect to beam axis. *IEEE Trans Biomed Eng* 1987; 34:779-89.

Newhouse VL, Dickerson KS, Cathignol D, Chapelon JY. 3-dimensional vector flow estimation using two transducers and spectral width. *IEEE Transactions on Ultrasonics Ferroelectrics and Frequency Control* 1994; 41:90-5.

Newhouse VL, Varner LW, Bendick PJ. Geometrical spectrum broadening in ultrasonic Doppler systems. *IEEE Trans Biomed Eng* 1977;24:478-80.

Osmani BF, Montaldo G, Tanter M. Out-of-plane Doppler imaging based on ultrafast plane wave imaging. *IEEE Transactions on Ultrasonics Ferroelectrics and Frequency Control* 2015;62:625-36.

Palm-Meinders IH, Box FMA, de Craen AJM, Blauw GJ, van Buchem MA, van der Grond J, Prosper Study Group. Diastolic wall shear stress in the internal carotid artery is associated with different cardiovascular risk factors than systolic wall shear stress. *Cerebrovasc Dis* 2009;28:185-90.

Pedersen MM, Pihl MJ, Haugaard P, Hansen KL, Lange T, Lonn L, Nielsen MB, Jensen JA. Novel flow quantification of the carotid bulb and the common carotid artery with vector flow ultrasound. *Ultrasound Med Biol* 2014; 40:2700-6.

Peronneau P, Xhaard M, Diebold B, Fiessinger JN, Levy B. Transcutaneous flow measurement by Doppler ultrasonic velocimetry with pulsed emissions. *Nouv Presse Med* 1976; 5:2547.

Peronneau PB, J.P.; Bugnon, A.; Barbet, A.; Xhaard, M. Theoretical and practical aspects of pulsed Doppler flowmetry real-time application to the measure of instantaneous velocity profiles in vitro and in vivo. In: Reneman RS, ed. *Cardiovascular Applications of Ultrasound*. Amsterdam: North Holland Publishing, 1974. pp. 66-84.

Pihl MJ, Jensen JA. A transverse oscillation approach for estimation of three-dimensional velocity vectors, part I: Concept and simulation study. *IEEE Transactions on Ultrasonics Ferroelectrics and Frequency Control* 2014; 61:1599-607.

Pihl MJ, Jensen JA. Measuring 3D velocity vectors using the transverse oscillation method. *Proceedings of IEEE International Ultrasonics Symposium, Dresden, Germany* 2012, pp. 1881-85

Pihl MJ, Stuart MB, Tomov BG, Rasmussen MF, Jensen JA. A transverse oscillation approach for estimation of three-dimensional velocity vectors, part II: Experimental validation. *IEEE Transactions on Ultrasonics Ferroelectrics and Frequency Control* 2014; 61:1608-18.

Plett MI, Beach KW, Dunmire B, Brown KG, Primozych JF, Strandness E. In vivo ultrasonic measurement of tissue vibration at a stenosis: A case study. *Ultrasound Med Biol* 2001; 27:1049-58.

Poepping TL, Rankin RN, Holdsworth DW. Flow patterns in carotid bifurcation models using pulsed Doppler ultrasound: Effect of concentric versus eccentric stenosis on turbulence and recirculation. *Ultrasound Med Biol* 2010; 36:1125-34.

Ramnarine KV, Anderson T, Hoskins PR. Construction and geometric stability of physiological flow rate wall-less stenosis phantoms. *Ultrasound Med Biol* 2001; 27:245-50.

Ramnarine KV, Hoskins PR, Routh HF, Davidson F. Doppler backscatter properties of a blood-mimicking fluid for Doppler performance assessment. *Ultrasound Med Biol* 1999; 25:105-10.

Reininger AJ, Reininger CB, Heinzmann U, Wurzingler LJ. Residence time in niches of stagnant flow determines fibrin clot formation in an arterial branching model - detailed flow-analysis and experimental results. *Thromb Haemost* 1995; 74:916-22.

Ricci S, Bassi L, Tortoli P. Real-time vector velocity assessment through multigate Doppler and plane waves. *IEEE Transactions on Ultrasonics Ferroelectrics and Frequency Control* 2014; 61:314-24.

- Seo Y, Ishizu T, Atsumi A, Kawamura R, Aonuma K. Three-dimensional speckle tracking echocardiography - a promising tool for cardiac functional analysis. *Circ J* 2014; 78:1290-301.
- Shung KK, Cloutier G, Lim CC. The effects of hemtocrit, shear rate, and turbulence on ultrasonic Doppler spectrum from blood. *IEEE Trans Biomed Eng* 1992; 39:462-9.
- Shung KK, Yuan YW, Fei DY, Tarbell JM. Effect of flow disturbance on ultrasonic backscatter from blood. *J Acoust Soc Am* 1984; 75:1265-72.
- Slager CJ, Wentzel JJ, Gijzen FJH, Thury A, van der Wal AC, Schaar JA, Serruys PW. The role of shear stress in the destabilization of vulnerable plaques and related therapeutic implications. *Nature Clinical Practice Cardiovascular Medicine* 2005; 2:456-64.
- Smith RF, Rutt BK, Fox AJ, Rankin RN, Holdsworth DW. Geometric characterization of stenosed human carotid arteries. *Acad Radiol* 1996; 3:898-911.
- Smith RF, Rutt BK, Holdsworth DW. Anthropomorphic carotid bifurcation phantom for mri applications. *JMRI-Journal of Magnetic Resonance Imaging* 1999; 10:533-44.
- Smith SW, Pavy HG, von Ramm OT. High-speed ultrasound volumetric imaging-system .1. Transducer design and beam steering. *IEEE Transactions on Ultrasonics Ferroelectrics and Frequency Control* 1991; 38:100-8.
- Sotelo J, Urbina J, Valverde I, Tejos C, Irrarrazaval P, Andia ME, et al. 3D quantification of wall shear stress and oscillatory shear index using a finite-element method in 3D cine PC-MRI data of the thoracic aorta. *IEEE Trans Med Imaging* 2016; 35:1475-87.
- Steel R, Fish PJ. Velocity bias and fluctuation in the standard dual beam Doppler reconstruction algorithm. *IEEE Transactions on Ultrasonics Ferroelectrics and Frequency Control* 2002; 49:1375-83.
- Steel R, Fish PJ. Sample volume misregistration in linear array-based dual beam Doppler ultrasound systems. *IEEE Transactions on Ultrasonics Ferroelectrics and Frequency Control* 2003; 50:836-47.
- Steel R, Ramnarine KV, Criton A, Davidson F, Allan PL, Humphries N, et al. Angle-dependence and reproducibility of dual-beam vector Doppler ultrasound in the common carotid arteries of normal volunteers. *Ultrasound Med Biol* 2004; 30:271-6.
- Stein PD, Sabbah HN. Measure turbulence and its effect on thromus formation. *Circulation Res* 1974; 35:608 - 14.
- Strong K, Mathers C, Bonita R. Preventing stroke: Saving lives around the world. *Lancet Neurol* 2007; 6:182-7.

Surry KJM, Austin HJB, Fenster A, Peters TM. Poly(vinyl alcohol) cryogel phantoms for use in ultrasound and MR imaging. *Phys Med Biol* 2004; 49:5529-46.

Swanepoel AC, Pretorius E. Prevention and follow-up in thromboembolic ischemic stroke: Do we need to think out of the box? *Thromb Res* 2015; 136:1067-73.

Tambasco M, Steinman DA. Path-dependent hemodynamics of the stenosed carotid bifurcation. *Ann Biomed Eng* 2003; 31:1054-65.

Tang DL, Yang C, Kobayasi S, Zheng J, Vito RP. Effect of stenosis asymmetry on blood flow and artery compression: A three-dimensional fluid-structure interaction model. *Ann Biomed Eng* 2003; 31:1182-93.

Tanter M, Bercoff J, Sandrin L, Fink M. Ultrafast compound imaging for 2-D motion vector estimation: Application to transient elastography. *IEEE Transactions on Ultrasonics Ferroelectrics and Frequency Control* 2002; 49:1363-74.

Tanter M, Fink M. Ultrafast imaging in biomedical ultrasound. *IEEE Transactions on Ultrasonics Ferroelectrics and Frequency Control* 2014; 61:102-19.

Thorne ML, Poepping TL, Rankin RN, Steinman DA, Holdsworth DW. Use of an ultrasound blood-mimicking fluid for Doppler investigations of turbulence in vitro. *Ultrasound Med Biol* 2008; 34:1163-73.

Tortoli P, Bassi L, Boni E, Dallai A, Guidi F, Ricci S. Quantitative dual-beam Doppler ultrasound investigations. *Proceedings of IEEE International Ultrasonics Symposium, Vancouver, BC 2006*. pp. 979-88.

Tortoli P, Guidi G, Mantovani L, Newhouse VL. Velocity magnitude estimation with linear arrays using Doppler bandwidth. *Ultrasonics* 2001; 39:157-61.

Tortoli P, Lenge M, Righi D, Ciuti G, Liebgott H, Ricci S. Comparison of carotid artery blood velocity measurements by vector and standard Doppler approaches. *Ultrasound Med Biol* 2015; 41:1354-62.

Trahey GE, Allison JW, von Ramm OT. Angle independent ultrasonic-detection of blood-flow. *IEEE Trans Biomed Eng* 1987; 34:965-7.

Trucco A. Thinning and weighting of large planar arrays by simulated annealing. *IEEE Transactions on Ultrasonics Ferroelectrics and Frequency Control* 1999; 46:347-55.

U-King-Im JM, Young V, Gillard JH. Carotid-artery imaging in the diagnosis and management of patients at risk of stroke. *Lancet Neurol* 2009; 8:569-80.

Udesen J, Gran F, Hansen KL, Jensen JA, Thomsen C, Nielsen MB. High frame-rate blood vector velocity imaging using plane waves: Simulations and preliminary experiments. *IEEE Transactions on Ultrasonics Ferroelectrics and Frequency Control* 2008; 55:1729-43.

- Udesen J, Jensen JA. Investigation of transverse oscillation method. *IEEE Transactions on Ultrasonics Ferroelectrics and Frequency Control* 2006; 53:959-71.
- Umetsu S. Determination of arterial blood flow by an ultrasonic device. *J Clin Ultrasound* 1981; 9:209 - 16.
- Valliant A, McComb K. Vascular access monitoring and surveillance: An update. *Adv Chronic Kidney Dis* 2015; 22:446-52.
- Vilkomerson D, Chilipka T, Outcault R, Goldman K. An instrument for screening for carotid stenoses. *Proceedings of SPIE Medical Imaging 2005: Ultrasonic Imaging and Signal Processing, SanDiego, CA* 2005; 5750:254-68.
- Wagner RF, Smith SW, Sandrik JM, Lopez H. Statistics of speckle in ultrasound B-scans. *IEEE Transactions on Sonics and Ultrasonics* 1983; 30:156-63.
- Warlow C, Sudlow C, Dennis M, Wardlaw J, Sandercock P. Stroke. *Lancet* 2003; 362:1211-24.
- Weber PK, Austeng A, Holm S, Aakvaak N. 1D-and 2D-sparse-array-optimization. *Instrum Sci Technol* 1999; 27:235-46.
- Wigstrom L, Ebberts T, Fyrenius A, Karlsson M, Engvall J, Wranne B, Bolger AF. Particle trace visualization of intracardiac flow using time-resolved 3D phase contrast MRI. *Magn Reson Med* 1999; 41:793-9.
- Wong EY, Nikolov HN, Rankin RN, Holdsworth DW, Poepping TL. Evaluation of distal turbulence intensity for the detection of both plaque ulceration and stenosis grade in the carotid bifurcation using clinical Doppler ultrasound. *Eur Radiol* 2013; 23:1720-8.
- Yen JT, Smith SW. Real-time rectilinear 3-D ultrasound using receive mode multiplexing. *IEEE Transactions on Ultrasonics Ferroelectrics and Frequency Control* 2004; 51:216-26.
- Yiu BYS, Lai SSM, Yu ACH. Vector projectile imaging: Time-resolved dynamic visualization of complex flow patterns. *Ultrasound Med Biol* 2014; 40:2295-309.
- Zarins CK, Giddens DP, Bharadvaj BK, Sottiurai VS, Mabon RF, Glagov S. Carotid bifurcation atherosclerosis quantitative correlation of plaque localization with flow velocity profiles and wall sheas-stress. *Circ Res* 1983; 53:502-14.
- Zell K, Sperl JI, Vogel MW, Niessner R, Haisch C. Acoustical properties of selected tissue phantom materials for ultrasound imaging. *Phys Med Biol* 2007; 52:N475-N84.
- Zuech PE, Cobbold RSC, Johnston KW, Kassam M. Spectral-analysis of Doppler flow velocity signals - assessment of objectives, methods, and interpretation. *Ann Biomed Eng* 1984; 12:103-16.

Appendices

Appendix A-1 Justification of Effective Wall Filter Value

The Doppler shifts from three receivers of a 3R configuration are shown in Fig. A-1.1 for inter-beam angles of 15° and 25° . These results complement those shown in Fig. 3.2 (Ch. 3), which correspond to an inter-beam angle of 20° , and thus further justify the choice of the WF_{eff} . The experimental mean Doppler shifts for the third beam (beam3) lie close to or within the 10-Hz cutoff, and therefore show higher standard deviations, ranging from 9 Hz to 22 Hz (i.e. twice the Doppler frequency), for nearly all orientations reflecting the effect of the 10-Hz WF_{eff} .

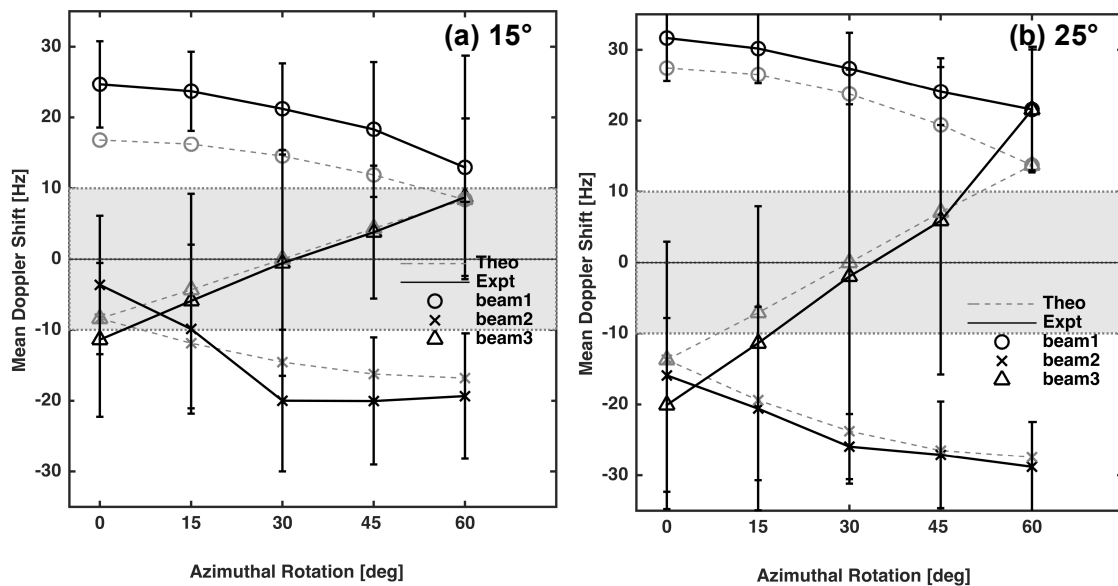


Figure A-1.1: Experimental mean Doppler shifts (solid) averaged over 160 independent measurements of a velocity of 2 cm/s with a 3R configuration with inter-beam angles of (a) 15° and (b) 25° . The corresponding theoretical Doppler shifts are shown with gray markers. The gray band represents the effective wall-filter cut-off range ($\pm WF_{\text{eff}}$). Error bars represent standard deviations over 160 independent measurements.

Appendix A-2 Resultant Velocity Magnitude and Direction

Similar to Fig. 3.7, which was shown for $\Delta\phi = 0^\circ$, Fig. A-2.1 shows the resultant velocity magnitude and directions for the remaining azimuthal rotations, $\Delta\phi = 15^\circ, 30^\circ, 45^\circ$, and 60° (rows 1 to 4) calculated from the respective velocity components shown in Fig. 3.6 to obtain 3R – 8R configurations. The results shown here complement the results from Fig. 3.7, i.e. the estimated velocity magnitudes agree with the theoretical parabolic profile to within 15% for velocities as low as 3 cm/s, for all configurations and rotations ($\Delta\phi = 0^\circ$ to 60°). The angle error for velocities ≥ 3 cm/s is stays within 5° for ≥ 5 R configurations for all rotations, but it varied up to $\pm 10^\circ$ for 3R and $\pm 15^\circ$ (at $\Delta\phi = 15^\circ$) for 4R.

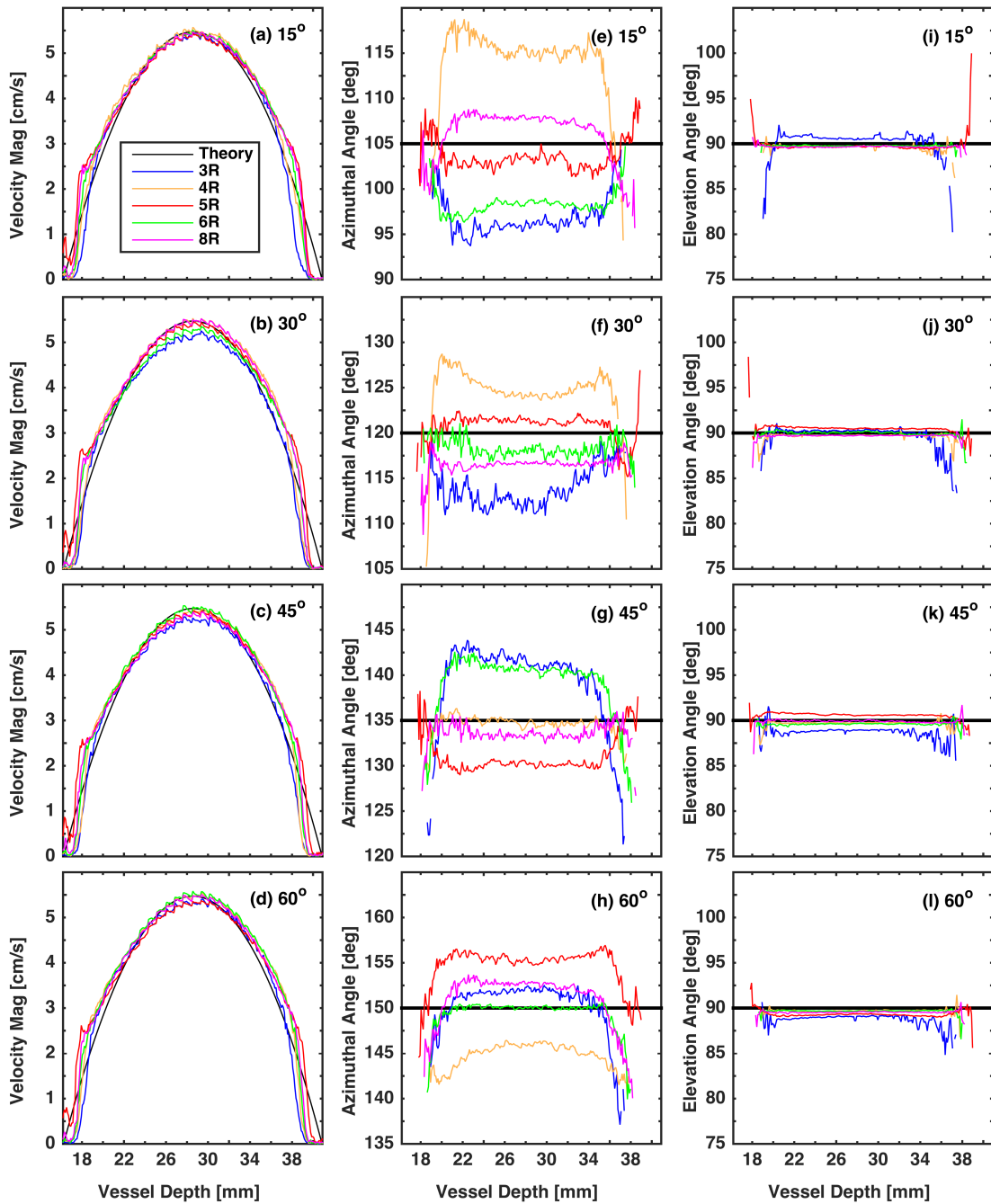


Figure A-2.1: Sample parabolic flow data representing mean Doppler velocity vector estimations for (a) magnitude, (b) azimuthal direction, and (c) elevation direction, averaged over 160 independent measurements for each of 3R - 8R configurations, with $\beta = 20^\circ$, for velocity vectors oriented at an azimuthal angles of 105° , 120° , 135° , and 150° (i.e., azimuthal rotations of $\Delta\phi = 15^\circ$, 30° , 45° , and 60° , respectively, relative to y axis) and elevation angle $\theta = 90^\circ$, after applying the PT method. Theoretical velocity magnitude profile and direction are shown in solid black line.

Appendix A-3 Geometric Analysis at WF_{eff} of 50 Hz for 10 cm/s

Fig. A-3.1 shows the results from the theoretical geometric analysis performed with WF_{eff} of 50 Hz for a flow velocity of 10 cm/s. The results match the findings from Fig. 3.3 (corresponding to 10 Hz, 2 cm/s), suggesting a minimum inter-beam angle of $<15^\circ$, $\sim 21^\circ$, and $\sim 25^\circ$ exists for the 8R, 6R, and 5R configurations, respectively for the worst-case azimuthal orientation, $\Delta\phi$, for each configuration.

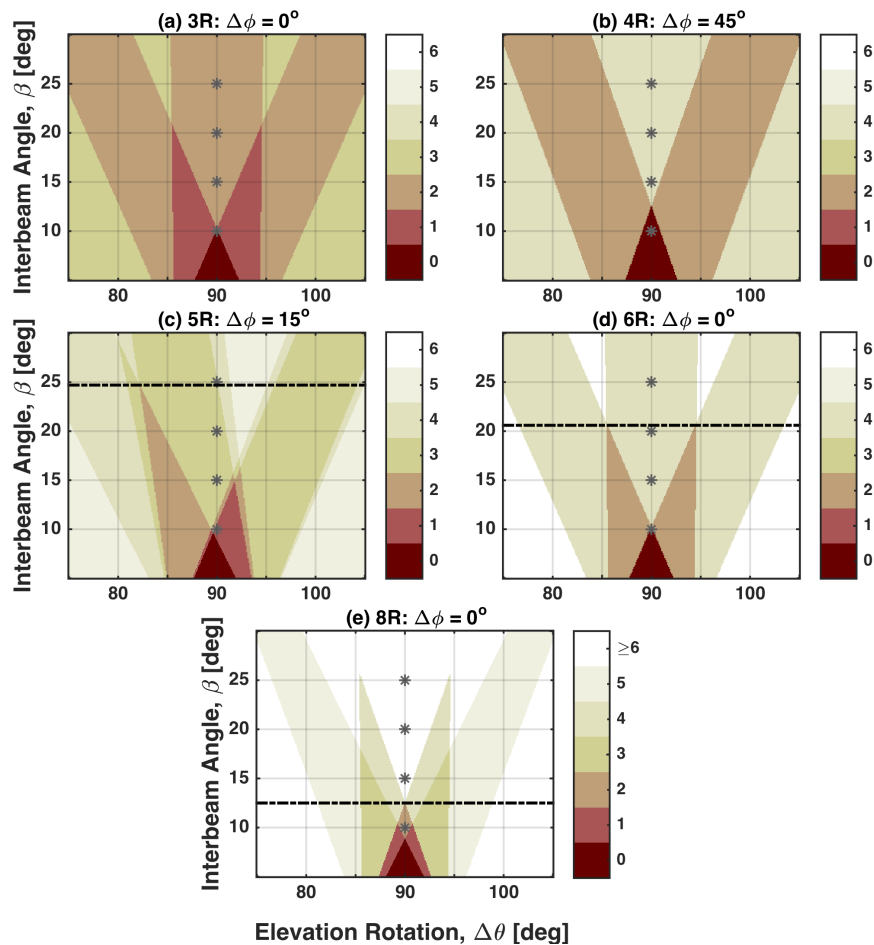


Figure A-3.1: Color-encoded plots similar to Fig. 3.3 shown here for a WF_{eff} of 50 Hz and for a 10 cm/s velocity vector rotated through $\Delta\theta$ from 75° to 105° relative to the x-axis and for the worst-case of, $\Delta\phi$. The black dashed-line represents the minimum inter-beam angle for which ≥ 3 receivers' Doppler shifts are above the WF_{eff} for all velocity orientations.

Appendix A-4 Performance of 5R Configuration at $\beta = 15^\circ$

Fig. A-4.1 is shown to demonstrate the compromises that need to be made when lowering the inter-beam angle to 15° to reduce the probe size of the 2D array. Overall, the WLS method had better accuracy and reliability at $\beta = 20^\circ$ as shown in Fig. 3.10. It is established that reducing the inter-beam angle reduces the accuracy and reliability of the estimates and are poorer for the PT method compared to WLS method. The reduced accuracy, e.g. at a velocity of 2 cm/s, can be illustrated by the increase in the relative error from 21% to 50%, and the reduced reliability is suggested by the increased SD from ~ 0.3 cm/s to 0.4 cm/s [Fig. 3.10(b) and Fig. A-4.1(b) respectively] for the WLS method. For the PT method, the error instead increases to 66%, and the SD increases to ~ 0.9 cm/s. The bias and SD in the angle stay within $2^\circ \pm 4^\circ$ for both methods. These results suggest that reducing the probe size comes at a cost of reduced accuracy and reliability especially in the estimation of velocity magnitude. However, this can be minimized with an optimized choice of a beam-selection method.

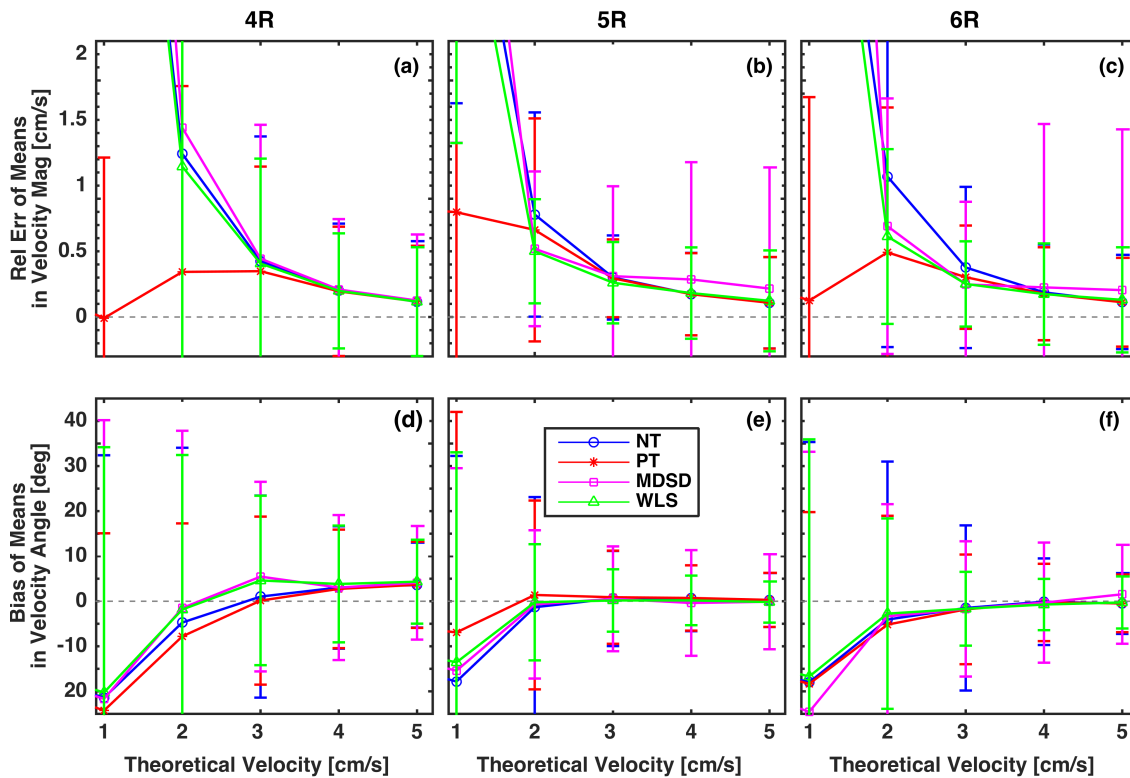


Figure A-4.1: Relative error of the mean velocity magnitude (a-c) and direction bias (d-f) comparing beam-selection methods for a theoretical velocity range of 1 to 5 cm/s for 4R - 6R configurations (as labeled) at $\beta = 15^\circ$. Biases are averaged differences over all velocity vector orientations ($\Delta\phi = 0^\circ, 15^\circ, 30^\circ, 45^\circ, 60^\circ$ relative to y axis). Error bars represent the standard deviations over 800 measurements.

Curriculum Vitae

Name: Bushra Hussain

Place of Birth: Karachi, Pakistan

Post-secondary Education and Degrees:

2007 – 2017 Ph.D. Medical Physics
The University of Western Ontario
London, Ontario, Canada

2002 – 2005 M.S. Physics
Eastern Michigan University
Ypsilanti, Michigan, U.S.A

1989 – 1990 M.Sc. Physics
University of Karachi
Karachi, Pakistan

1985 - 1989 B.Sc. (Hons.) Physics
University of Karachi
Karachi, Pakistan

Honours and Awards:

2010 Shortlisted for best poster at Canadian Association of Physicists
Conference, Toronto, Canada.

2007 – 2009 CIHR Strategic Training Program in Vascular Research

2005 Graduate Assistant of the Year Award,
Eastern Michigan University, MI, USA

2003 Best Quantum Mechanics Student Award, Eastern Michigan
University, USA

1989 – 1990 Fauji Foundation Scholarship, University of Karachi, Pakistan

1979 Best Mathematics Student of the Year Award, Cranford
Community School, UK

Related Work Experience

2007 – 2011 Graduate Teaching Assistant
Department of Physics and Astronomy
University of Western Ontario, London, ON, Canada

- 2006 – 2007 Physics Instructor
Bloomsburg University of Pennsylvania, Department of Physics
and Engineering Technology, PA, USA
- 2005 Adjunct Instructor
Henry Ford Community College
Department of Physics, Dearborn, MI, USA
- 2002 – 2004 Graduate Teaching Assistant
Eastern Michigan University
Department of Physics and Astronomy, Ypsilanti, MI, USA
- 2004 – 2005 Individual Tutor
Eastern Michigan University
Holman Learning Center, Ypsilanti, MI, USA
- 1993 – 2002 Physics Instructor
Federal Government College for Women F-7/2,
Department of Physics, Islamabad, Pakistan

Publications and Proceedings:

B. Hussain, B. Y. S. Yiu, A. C. H. Yu, J. C. Lacefield, T. L. Poepping, “Investigation of Crossbeam Multi-receiver Configurations for Accurate 3-D Vector Doppler Velocity Estimation”, vol. 63, pp. 1786-1798, 2016.

B. Hussain, E. Y. Wong, B. Y. S. Yiu, A. C. H. Yu, and T. L. Poepping, "Evaluation of Cross-beam Vector Doppler Ultrasound Systems for Accurate 3-D Velocity Measurements," in 2012 IEEE International Ultrasonics Symposium, 2012, pp. 326-329.

B. Hussain, E.Y. Wong, and T.L. Poepping. “Numerical design and evaluation of vector Doppler ultrasound systems for accurate 3-D velocity measurements”, Proceedings of IEEE International Ultrasonics Symposium: Vector Flow Imaging Methods, San Diego, California, Sept 2010, paper no. 1023.

Presentations:

B. Hussain, E. Y. Wong, B. Y. S. Yiu, A. C. H. Yu, and T. L. Poepping. “A Novel Vector Doppler Ultrasound Method for Improved Near-Wall 2D-Vector Blood Velocity Estimations: Aperture – Translation”, Imaging Network Ontario, London, Ontario, Mar 2017 (poster).

B. Hussain, E. Y. Wong, B. Y. S. Yiu, A. C. H. Yu, and T. L. Poepping. "A Novel Vector Doppler Ultrasound Method for Improved low 2D-Vector Velocity Estimation: Apertur-Translation", Fallona Family Interdisciplinary Science Showcase, London, Ontario, Jan 2017 (poster).

B. Hussain, E. Y. Wong, B. Y. S. Yiu, A. C. H. Yu, and T. L. Poepping. "Experimental Validation of Vector Doppler Ultrasound for Accurate 3D Measurements of Complex Flow", The Artimino Conference on Medical Ultrasound Technology, Muskoka, Ontario, June 2013 (oral).

B. Hussain, E. Y. Wong, B. Y. S. Yiu, A. C. H. Yu, and T. L. Poepping. "Geometric Optimization of Vector Doppler Ultrasound for Accurate 3D Measurements of Complex Flow", The Artimino Conference on Medical Ultrasound Technology, Artimino, Italy, June 2011 (oral).

B. Hussain, E. Y. Wong, and T. L. Poepping. "Design of a Vector Doppler Ultrasound System for Accurate 3-D Flow Velocity Measurements", Canadian Association of Physicists Conference, Toronto, Ontario, June 2010 (poster).

B. Hussain, E. Y. Wong, and T. L. Poepping. "Design of a Vector Doppler Ultrasound System for Accurate 3-D Flow Velocity Measurements", London Imaging Discovery Conference, London, Ontario, June 2010 (poster).

B. Hussain, E. Y. Wong, and T. L. Poepping. "Design of a Vector Doppler Ultrasound System for Accurate 3-D Flow Velocity Measurements", Taylor Symposium, London, Ontario, Nov 2009 (poster).

B. Hussain, E. Y. Wong, and T. L. Poepping. "Design of a Vector Doppler Ultrasound System for Accurate 3-D Flow Velocity Measurements", London Imaging Discovery Conference, London, Ontario, June 2009 (poster).